TEMPLATED HYBRID HYDROGELS FOR OSTEOCHONDRAL REPAIR

A Dissertation

by

MICHAEL T. FRASSICA

Submitted to the Office of Graduate and Professional Studies of
Texas A&M University
in partial fulfillment of the requirements for the degree of

DOCTOR OF PHILOSOPHY

Chair of Committee,	Melissa A. Grunlan
Committee Members,	Daniel L. Alge
	Akhilesh K. Gaharwar
	W. Brian Saunders
Head of Department,	Michael J. McShane

December 2020

Major Subject: Biomedical Engineering

ABSTRACT

A synthetic materials-guided approach, wherein the scaffold's chemical and physical properties alone instruct cellular behavior for tissue regeneration, has the potential to repair clinically pervasive osteochondral defects (OCDs) without the use of exogenous growth factors. Poly(ethylene glycol) diacrylate (PEG-DA) hydrogels are widely utilized in tissue regeneration, but lacks macroporosity for osteoconduction and are also not strongly bioactive (i.e. inducing mineralization for bone bonding) or osteoinductive (i.e. inducing mesenchymal stem cell [MSC] differentiation toward an osteoblastic-lineage). Previously, work by Grunlan and coworkers established that inclusion of star poly(dimethyl siloxane) methacrylate (PDMS$_{star}$-MA) with PEG-DA produced hydrogels with enhanced bioactivity and osteoinductivity. Furthermore, fabrication with solvent-induced phase separation and a salt template ("SIPS/salt") yielded interconnected, macroporous scaffolds with excellent distribution of the siloxane macromer. Towards achieving osteochondral regeneration, this work sought to prepare macroporous PEG-based hydrogel scaffolds that included siloxane or phosphonated-siloxane macromers, ultimately prepared as monolithic scaffolds with spatial control of chemical and physical properties. In a first study, SIPS/salt scaffolds were prepared with PDMS$_{star}$-MA of two number average molecular weights (M_n's) (2k and 7k) with varying PDMS$_{star}$-MA:PEG-DA ratios and template salt sizes. Interconnected macropore size was tuned by the salt size, and a more uniform distribution was achieved with a lower M_n PDMS$_{star}$-MA. All PDMS$_{star}$-PEG hydrogels were confirmed to be bioactive upon

exposure to 1X simulated body fluid (SBF) and, when cultured with human bone marrow derived MSCs (hBMSCs) for 14 days, displayed a PDMS$_{star}$-MA dose-dependent increase in osteogenesis. In a second study, to further increase bioactivity and osteoinductivity, a siloxane macromer with pendant phosphonate groups, poly(diethyl(2-(propylthio)ethyl) phosphonate methylsiloxane) diacrylate (PPMS-DA), was synthetized. SIPS/salt PPMS:PEG scaffolds showed an enhanced osteogenic potential versus PDMS:PEG scaffolds when cultured with hBMSCs for 14 and 28 days. Finally, to afford spatial control of chemical and physical properties, a method was developed to prepare monolithic scaffolds from such individual scaffolds, termed 'hydrogel scaffolds with spatially tunable chemistries and arrangements' (SSTACs). Demonstrated with several SSTAC designs, the desired spatial distribution of chemistry and pore size was confirmed. Moreover, the interfaces of SSTACs were shown to lack a hard boundary and achieved good mechanical integrity.

DEDICATION

To My Mom

Your persistent love and support gave me the confidence to begin this journey and has

remained for each hurdle along the way. Your perseverance and unwavering support

inspires me every day. Thank you for always being there.

ACKNOWLEDGEMENTS

I would first like to thank my committee chair, Prof. Melissa Grunlan. Even with minimal research experience, Prof. Grunlan showed confidence that I would learn, adapt and succeed. I will forever be grateful for Prof. Grunlan's patient support and guidance during my individual and academic development. I would also like to thank my committee members, Prof. Daniel Alge, Prof. Akhilesh Gaharwar, and Prof. Brian Saunders for the time and support they have provided during my doctoral studies.

Thank you to the Department of Biomedical Engineering, including friends, colleagues, faculty and staff. The department's collaborative and inclusive environment greatly improved my doctoral studies. Within the Grunlan lab, I could not have achieved this without the friendship and support of Dr. Lindsay Woodard, Dr. Kristen Means, Dr. Jakkrit Suriboot, Dr. Bryan Ngo, Michaela Pfau, Ping Dong, Felipe Beltran, Alec Marmo and Connor Demott. I owe a special thanks to the undergraduates who contributed greatly to this work including Mallory Taylor, Sarah Jones, Esteban Ramirez, and Caleb Chesney.

I also must thank my family and friends. Mom, it would have been impossible to complete this without your constant encouragement. Dad, your perseverance and work ethic inspires me to always strive for more and is the reason I began this journey. Brianna, your support and visits are always appreciated much more than you know. To my friends, your persistent friendship through distance and time has helped more than you could know. Finally, Mallory, your love and encouragement has given me constant strength. I am forever grateful for your sacrifices and unwavering support.

CONTRIBUTORS AND FUNDING SOURCES

Contributors

Funding Sources

TABLE OF CONTENTS

LIST OF FIGURES

Page

CHAPTER I

INTRODUCTION: PERSPECTIVES ON SYNTHETIC MATERIALS TO GUIDE

TISSUE REGENERATION FOR OSTEOCHONDRAL REPAIR[*]

1.1. Overview

Regenerative engineering holds the potential to treat clinically pervasive osteochondral defects (OCDs). In a synthetic materials-guided approach, the scaffold's chemical and physical properties alone instruct cellular behavior in order to effect regeneration, referred to herein as "instructive" properties. While this alleviates the costs and off-target risks associated with exogenous growth factors, the scaffold must be potently instructive to achieve tissue growth. Moreover, toward achieving functionality, such a scaffold should also recapitulate the spatial complexity of the osteochondral tissues. Thus, in addition to the regeneration of the articular cartilage and underlying cancellous bone, the complex osteochondral interface, composed of calcified cartilage and subchondral bone, should also be restored. In this Perspective, we highlight recent synthetic-based, instructive osteochondral scaffolds that have leveraged new material chemistries as well as innovative fabrication strategies. In particular, scaffolds with spatially complex chemical and morphological features have been prepared with electrospinning, solvent-casting–particulate-leaching, freeze-drying, and additive

manufacturing. While few synthetic scaffolds have advanced to clinical studies to treat OCDs, these recent efforts point to the promising use of the chemical and physical properties of synthetic materials for regeneration of osteochondral tissues.

1.2. Introduction

Osteochondral defects (OCDs) are injuries to the cartilage of the knee or ankle that extend from the articular cartilage into the underlying subchondral bone (**Figure 1-1**).[1] These defects, occurring from traumatic lesions or osteochondritis dissecans, cause severe pain and diminished mobility.[2-4] Due to the limited healing capacity of this interface,[5] defects can progress to osteoarthritis (OA) and necessitate total joint replacement.[6, 7] As the depth of the defect often extends beyond that of partial or full chondral defects (**Figure 1-1**), limited success is observed for procedures such as microfracture and autologous chondrocyte implantation (ACI) due to the inability to regenerate subchondral bone and articular cartilage.[8, 9] Thus, grafting is the most common clinical option to treat OCDs, with cylindrical autografts utilized for smaller defects (diameter < 3 cm^2) and allografts for larger defects (diameter > 3 cm^2).[10, 11] However, both strategies suffer from a lack of graft availability and delamination from the surrounding tissue, along with risk of donor site morbidity for autografts and disease transmission/rejection for allografts.[11-13] Thus, regenerative engineering has emerged as a promising option to heal OCDs.[14, 15]
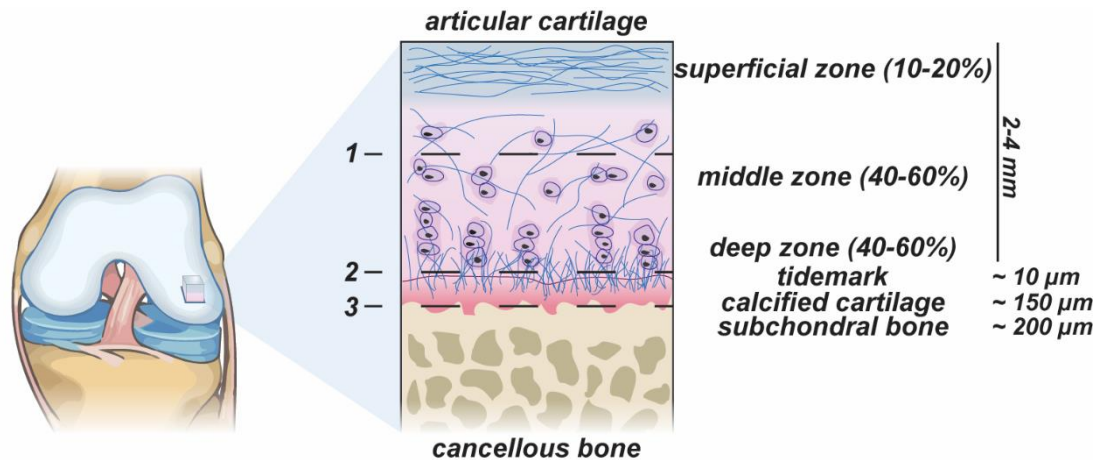
Figure 1-1. Schematic representation of tissue composition along the osteochondral interface. Defect depth is denoted (left) as partial chondral defect (1), full chondral defect (2), and osteochondral defect (3). Cartilage layers are denoted (upper right) with approximate percentage of the cartilage tissue each zone comprises. Cellularity enhances with each layer of cartilage, eventually forming a transition of calcified cartilage connected to the subchondral bone plate. Interface components are labeled (lower right) with approximate sizes.

In general, regenerative engineering aims to provide a temporary three-dimensional (3D) environment or "scaffold", in lieu of the native extracellular matrix (ECM), for recruited or seeded cells to proliferate and regenerate tissue.[16, 17] Mesenchymal stem cells (MSCs), able to differentiate toward multiple cell lineages, are most widely used due to their ease of isolation from numerous adult tissues and their manipulability.[18, 19] Exogenous growth factors, or cellular signaling proteins, are commonly included in scaffolds to stimulate regeneration of tissues, including cartilage (e.g., insulin-like growth factor-1 [IGF-1] or transforming growth factor β-1 [TGFβ-1]) and bone (e.g., bone morphogenetic protein-2 [BMP-2] or vascular endothelial growth factor [VEGF]).[20] Achieving sustained, long-term release of growth factors from scaffolds during their degradation requires high loading levels which is associated with high costs and off-target

tissue responses.[21-23] For osteochondral tissue, the demand for spatiotemporal delivery of various growth factors represents an additional level of complexity.[24] In contrast, a material-based regenerative approach relies exclusively on scaffold chemical and physical material properties to guide tissue regeneration (i.e., without exogenous growth factors).[25-29] As with the ECM of native tissue, numerous scaffold properties have been shown to direct cell behavior, including morphology (e.g., pore size and shape),[30-34] modulus,[35-39] chemical functionality,[40-43] hydrophobicity,[44-46] and hydration.[47-49] Moreover, high porosity and interconnectivity are considered beneficial for nutrient diffusion and neotissue infiltration.[50] Such scaffolds that leverage material properties to guide tissue regeneration in these ways are referred to as "instructive",[27, 51, 52] and will be mentioned as such herein.

A materials-guided approach to treat OCDs represents a particular challenge due to the spatial complexity of tissues spanning this region (**Figure 1-1**). Osteochondral tissue consists of osseous and chondral tissues anchored together by a complex layer of calcified cartilage, beneath the tidemark and abutting the subchondral bone plate,[53, 54] a feature that is key to its ability to disperse normal load.[55] The bone tissue is a highly vascularized, porous scaffolding of organic collagen mineralized with inorganic hydroxyapatite (HAp), with a water content of ~20−30%. The cartilage tissue is a dense ECM of primarily collagen and glycosaminoglycans (GAGs) but with a much higher water content (~75%) and a more sparse distribution of native cells.[5, 56, 57] Furthermore, articular cartilage consists of three layers of different collagen fiber orientation and cellularity (**Figure 1-1**), resulting in remarkable biomechanical stability. In recent years, damage to this interface

has been identified as a major contributor to cartilage defects and OCD propagation due to its key role in supporting the intensive loading of the joint.[8, 55, 58] Leveraging the prior art on materials-guided scaffold properties associated with bone and cartilage regeneration, instructive osteochondral scaffolds have largely adopted designs with multiple phases and are often formed as cylindrical autograft-sized plugs.[59] Biphasic designs have been most extensively used, presenting two distinct environments for differentiation of multipotent cells toward an osteoblastic or chondrocytic lineage. However, the simple merging of two discrete scaffolds (e.g., by mechanical attachment, glue, or freeze-drying) creates a hard interface and so fails to mimic the nativelike complexity of the osteochondral interface.[60-62] Thus, recent designs have adopted triphasic, multiphasic, or gradient designs to recapitulate the transition between the calcified cartilage and subchondral bone plate as well as the zones of cartilage.

A broad range of biomaterials, both biologic and synthetic, have been utilized for OCD repair based on their success in orthopedic and other biomedical applications, as described in Di Luca et al., Longley et al., and Deng et al.[20, 21, 63] Among these materials, the most commonly utilized are approaches based on proteins such as collagen and silk fibroin for their adhesive and regenerative capacities, as recently reviewed in the literature.[20, 21, 63] However, because of the complex nature of cell−protein interactions, we have chosen to focus on the current state of synthetic-based scaffold strategies that do not include a protein component. This highlights the potency of scaffold material properties to independently drive regeneration. Synthetic materials are not without their drawbacks. For instance, bioresorbable polymers, such as poly(α-hydroxy acids), provide potential for

adverse effects to cellular regeneration from acidic degradation products. Attempts to mitigate such effects *in vivo* have included reduction of implant size and inclusion of additives.[64, 65] In the case of cartilage regeneration, synthetic materials are primarily combined with polysaccharides based on their unique mechanical properties as well as chemistries that enhance chondrogenesis; therefore, these systems are included. Thus, within this Perspective, we provide an outlook on the recent utility of the chemical and physical properties of synthetic scaffold systems for OCD repair, with a focus on highlighting common trends and potential areas for future investigation.

1.3. Considerations for Osteochondral-Instructive Scaffolds

Synthetic polymer scaffolds have been widely studied for decades in the field of tissue engineering. The level of control over key chemical and physical properties (e.g., degradation rate, pore morphology, chemical functionality, modulus, etc.) allowed by variations in chemistry and fabrication provides for an expansive scaffold library to apply to various tissue applications. Below, we highlight key criteria and materials for synthetic scaffolds useful for the regeneration of bone, cartilage, and the osteochondral interface.

1.3.1. Materials-Driven Osseous Tissue Regeneration

Bone tissue engineering has been extensively studied, as recently reviewed by Du et al.[66] and Yu et al.[67] For osseous tissue regeneration (i.e., osteogenesis), instructive scaffolds require osteoconductivity, osteoinductivity, and osseointegration[66-69] which may be achieved by their chemical and physical properties. Osteoconductivity is traditionally defined as a material's ability to encourage and support new bone formation on its surface. This has been identified to be facilitated by bioactivity (i.e., formation of a thin carbonated

HAp layer at the material surface) that adsorbs proteins for cellular attachment and proliferation.[70] Scaffold chemical composition (e.g., ion releasing[71] and phosphonate-containing[72]) and pore architecture (interconnected pore size of 200−500 μm[73, 74] or larger[75]) are associated with this trait, providing growth of the mineral layer and space for neotissue infiltration. Osteoinductivity is broadly understood as the ability to induce bone formation via cellular differentiation to a bone-forming lineage. Mechanisms for this action have been widely studied, including active facilitation of nutrient and waste transport via vascularization,[67, 76] adherence of progenitor cells on the material surface (via protein adsorption or direct integrin binding) and subsequent interaction with surface properties,[68, 77-79] osteogenic response to calcium and phosphate ions,[80-82] and concentration of osteogenic proteins by material affinity.[67, 83, 84] Osteoinductivity is often affiliated with a certain chemical composition (e.g., hydrophobic and inorganic materials such as bioglasses, calcium phosphates, siloxanes, and nanosilicates)[68, 85-91] and pore topography (e.g., mesopores,[92, 93] rough surfaces,[94] and aligned fibers[66]). Matrix stiffness is also identified as a key factor in osteogenesis, as adhered cells can respond to the local environment through a variety of mechanisms.[95, 96] Generally, stiffer matrices have been identified as osteogenic; however, other simultaneous cell−material interactions add complexity to a strict correlative relationship. To this point, in comparative studies, osteogenic moduli have been seen with hydrogels of 11−40 kPa[36, 97] or >225 kPa.[98] In other studies, osteogenesis has been observed for non-hydrogel matrices having moduli several magnitudes higher.[74, 99] Finally, osseointegration refers to the ability for the material to integrate with the surrounding bone. In general, this requires scaffold

bioactivity for immediate bone bonding, an interconnected pore architecture for infiltration of neotissue and vascularization, and biodegradability that supports the bone regeneration.[74] Ideally, scaffold degradation should parallel neotissue formation.[100] Calcium phosphates (including HAp), resembling the inorganic phase of native bone tissue, have been the most abundantly utilized material for bone regeneration. Such materials are known to recruit and stimulate MSCs while simultaneously initiating angiogenic and chemotactic responses.[71] For regenerative scaffolds, these have primarily been formed into composites with polymers, typically polyesters, for better control over pore morphology and toughness.[101, 102] More recently, bioglasses and bioceramics have seen use after modifications via element-doping (e.g., F^-, Cl^-, Na^+, and Mg^{2+})[20, 66] to mitigate their brittleness, to slow their resorption rates,[101, 103-105] and to advance osteogenic differentiation or suppress inflammation.[106, 107] Our group has demonstrated that bioactivity and osteoinductivity can also be achieved with nonbrittle materials by the incorporation of a silicon-based, inorganic polymer [star-polydimethylsiloxane methacrylate] into poly(ethylene glycol) diacrylate (PEGDA) hydrogels.[88, 89] The instructive behavior of this silicon-based polymer is attributed to the known role that silicon plays in bone mineralization and gene activation[108, 109] which had originally prompted the use of certain glasses, ceramics, and nanosilicates. As described later, fabrication strategies have been utilized to maximize the potential of these materials by controlling morphological features of the scaffold.

1.3.2. Materials-Driven Chondral Tissue Regeneration

Articular cartilage regeneration presents a significant challenge in tissue engineering, as reviewed by Armiento et al.,[9] with considerably less success compared to bone regeneration. Cartilage is a highly hydrated, avascular tissue that displays remarkably complex biomechanical behavior characterized by high compressive stiffness, strength, and lubricity.[5, 110] Such complexity can be attributed to its layered nature (**Figure 1-1**), wherein horizontally aligned collagen at the surface progresses to vertically aligned deeper in the tissue, resulting in the tissue's anisotropic feature. Furthermore, it has a remarkable ability to expel and regain its water content (up to 80% by weight) during loading and articulation.[111, 112] Toward materials-driven regeneration of cartilage, synthetic materials should recapitulate an environment that drives chondrogenesis through chondroconductivity, chondroinductivity, and chondrointegration. Chondroconductive scaffolds provide a morphology similar to that of the confined chondrocytic environment (smaller interconnected pores (< 300 μm)[113] with low porosity[114]) to facilitate cell−cell interactions for chondrogenesis. Chondroinduction (i.e., induced differentiation toward a chondrocytic lineage) is strongly related to the level of cellular adhesion wherein moderate adherence of MSCs to a material surface is preferred and promotes a spherical cell morphology resembling that of a chondrocyte.[115] Other factors can induce this morphological change as well, including encapsulation and scaffold morphology.[9, 116] Mechanotransduction has also been indicated in chondroinductivity[117, 118] and is part of a complex relationship between cell shape, matrix properties, and mechanical loading. Finally, for chondrointegration, vertical integration of regenerated cartilage with

9

underlying bone has been observed; however, lateral integration with native cartilage tissue is more challenging. This can be attributed to factors such as biomechanical mismatching, cell death at the defect edge, and the antiadhesive nature of the tissue itself.[119] In many cases, bioadhesives are thus employed.[120] Another key factor for chondrointegration is biodegradation, where a degradation rate that matches the rate of tissue growth and can maintain mechanical support is a necessity.

A variety of synthetic polymers (e.g., poly(ε-caprolactone) [PCL], poly(L-lactic acid) [PLLA], poly(lactide-co-glycolide) [PLGA], and poly(ethylene glycol) [PEG]), sometimes in combination with polysaccharides (e.g., cellulose, agarose, and alginate), have been explored for materials-guided cartilage regeneration.[9, 111] Due to their hydration, permeability, and associated lubricity, hydrogels have been most frequently used as materials for cartilage regeneration. PEG-DA hydrogels have been widely studied because of the ease of tuning cross-link density, and in turn the modulus, thereby impacting cellular differentiation toward chondrocytic cell types.[28, 48] However, such PEG scaffolds are limited in their ability to promote sufficient ECM production, which is associated with their lack of chemical and biological mimicry of native cartilage ECM. Thus, synthetic polymers have been combined with natural polymers (e.g., hyaluronic acid [HA], chondroitin sulfate [CS], and chitosan), due to the presence of charged groups like those comprising GAGs found in cartilage ECM, to form instructive scaffolds.[9, 121, 122] HA and CS have further been indicated in the binding of the cell adhesion peptide CD44, assisting in the support of cell−cell interactions and subsequent chondrogenesis.[123, 124] More recently, fibrous materials have been used for articular cartilage regeneration,

particularly those based on biodegradable polyesters such as poly(glycolic acid) [PGA], PLLA, and PCL.[9, 21, 125] These scaffolds' structure mimics the fibrous collagen of native cartilage, providing a morphologically similar environment and a compressive stiffness and strength more similar to that of cartilage. The aligned fibrous morphology of these scaffolds can support a chondrocytic phenotype,[125] as previously mentioned.

1.3.3. Materials-Driven Osteochondral Interface Regeneration

Beyond the "deep zone" of articular cartilage lies the osteochondral interface, consisting of calcified cartilage and the subchondral bone plate, leading subsequently to cancellous bone (**Figure 1-1**). Originally, instructive scaffolds regarded this area as a simple interface between two unique tissues (i.e., bone and cartilage). Thus, biphasic osteochondral scaffolds were formed by merging two independent scaffolds across a hard interface.[60-62] More recently, this interface has been recognized for its role in the pathophysiology of OCDs and eventual OA. Specifically, a healthy subchondral bone adapts to the load of locomotion dispersed by the calcified cartilage layer.[8, 126, 127] In osteochondral tissue formation, subchondral bone acts as a physical barrier that maintains the integrity of neocartilage and prevents bone in-growth, thereby directly relating it to the successful regeneration of articular cartilage.[8, 58] Thus, this interface has been addressed in osteochondral scaffolds by the incorporation of additional layer(s) or "phase(s)" with differing material properties. For triphasic scaffolds, the middle phase is treated as a discrete layer with intermediate properties between bone and cartilage.[128, 129] Often, "middle-ground" levels (between bone and cartilage) of scaffold porosity,[130-132] modulus,[9, 35, 97, 133] and material composition[21, 63] are used to create a transition. Successful *in vitro*

indications often show chondrocytic proliferation in a mineralized environment and expression phenotypical of hypertrophic chondrocytes, similar to that of the calcified cartilage layer.[134, 135] Examples of these strategies include diverse composites (e.g., agarose with HAp, organic sol gel-coated calcium polyphosphate),[136, 137] scaffold component orientations (e.g., arrayed plate-like HAp),[138] additives for osteochondral differentiation (e.g., Mg-doped wollastonite, icariin, or zinc oxide),[139-141] or components that promote a proregenerative environment (e.g., strontium or copper).[142, 143]

1.4. Materials-Guided Tissue Engineering Approaches – Clinical Trials

In the treatment of OCDs, nondegradable partial resurfacing devices and materials-driven regenerative devices have emerged in clinical trials. For partial resurfacing devices, a synthetic material permanently replaces damaged tissues. For example, Cartiva, a cryogenically fabricated poly(vinyl alcohol) (PVA) hydrogel, is an FDA approved therapeutic for the treatment of OCDs in the first metatarsal phalangeal joint.[144] Biopoly, currently in clinical trials, utilizes a titanium bone anchor and an ultra-high-molecular-weight poly(ethylene) (UHMWPE)/HA hybrid surface for treatment of osteochondral defects in the knee.[145] Several layered materials-guided OCD regenerative devices are in clinical trials, including protein-based devices such as BioMatrix CRD (Arthrex, US), Cartilage Repair Device (Kensey Nash Corp.), ChondroMimetic (Collagen Solutions, UK), and MaioRegen (Finceramic, Italy).[146, 147] However, only two OCD devices that use a synthetic materials-guided regenerative strategy without the incorporation of proteins and/or exogenous growth factors have undergone clinical trials. These two devices include the TruFit (Smith & Nephew, Andover, MA) and Agili-C (CartiHeal Ltd., Israel).
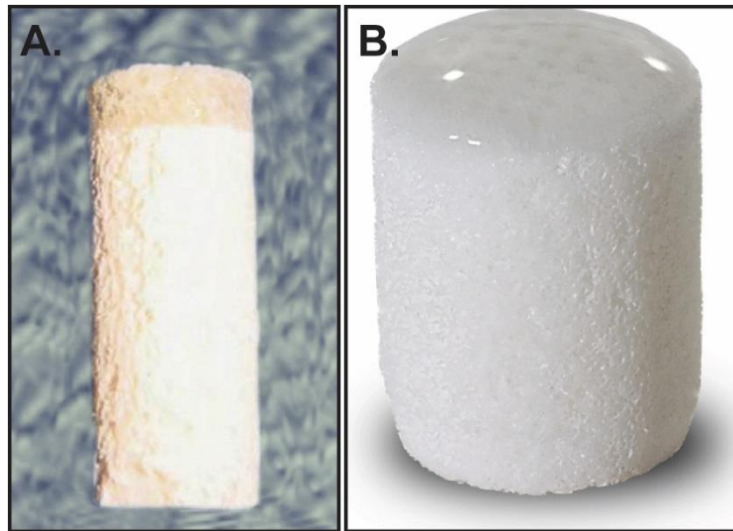
Figure 1-2. Tru-Fit CB **(left, A)** is a biphasic PLGA copolymeric scaffold with calcium sulfate (bone phase) and PGA fibers (chondral phase). The Agili-C **(right, B)** is a marine-derived aragonite (bone phase) scaffold with a hyaluronic acid-containing top (cartilage phase). Reproduced with permission from ref 148. Copyright 2014 Spring Berlin Heidelberg.

The TruFit Plug, an acellular biphasic scaffold, consists of a semiporous 75:25 poly(D,L-lactide-co-glycolide) (PLGA) copolymer with calcium sulfate incorporated in the lower bone phase and Poly(glycolic acid) (PGA) fibers in the upper cartilage phase (**Figure 1-2A**).[148, 149] The two phases are merged together using a small amount of solvent. Bone regeneration relies upon the osteoinductive and resorptive capacity of the calcium sulfate.[150, 151] The limited osteoconductivity (i.e., limited porosity) and brittleness associated with calcium sulfate are mitigated by fabricating as a composite with biodegradable PLGA. At the cartilage phase, PGA fibers are incorporated with the PLGA copolymer scaffold to provide a cartilage-mimetic fibrous environment for recruited

13

progenitor cells from the native tissue. The TruFit Plug advanced to clinical trials for osteochondral repair after initially being utilized for bone voids; however, it has since become unavailable.[152] While preclinical *in vivo* studies showed promise, this TruFit suffered from poor integration with adjacent tissue as well as a lack of sufficient subchondral bone growth in short- and long-term studies.[153-155]

More recently, the Agili-C was developed as an acellular biphasic instructive scaffold composed of coral-derived aragonite at the bone phase and aragonite/hyaluronic acid at the cartilage phase (**Figure 1-2B**).[148] Aragonite is a calcium carbonate with ∼2% sodium, magnesium, potassium, and other ions absorbed from the seawater during its formation.[156] Having interconnected pores ranging from 100 to 300 μm (porosity >50%), this material has recently been shown to support osteogenic differentiation of bone-marrow-derived MSCs.[156, 157] In addition to establishing the devices' biocompatibility and biodegradability, early studies of the device demonstrated its ability to recruit stem cells from the surrounding tissue, attributed to the complex, nanorough geometry of the aragonite and CD44 binding capacity of hyaluronic acid.[125, 158] More recent studies have shown restoration of high-quality cartilage and subchondral bone in a 12 month caprine model.[158] This biphasic device began a 250+ participant premarket approval (PMA) pivotal study in 2017 for treatment of joint surface lesions.[159] Results of this study will be informative regarding the regenerative potential of a biphasic scaffold to treat OCDs

Table 1-1. Select recent synthetic materials-guided strategies for osteochondral tissue engineering. Abbreviations include the following: β-TCP = β-tricalcium phosphate, A6ACA = N-acryloyl 6-aminocaproic acid, CaP = calcium phosphate, CSMA = chondroitin sulfate methacrylate, FDM = fused deposition modeling, HA = hyaluronic acid, HAp = hydroxyapatite, HRP = horseradish peroxidase, PAAm = poly(acrylamide), PCL = poly(ε-caprolactone), PDLLA = poly(D,L-lactide acid), PECDA = poly(ε-caprolactone)- poly(ethylene glycol)-poly(ε-caprolactone) diacrylate, PEG-DA = poly(ethylene glycol) diacrylate, PGA = poly(glycolic acid), PLGA = poly(D,Llactide-co-glycolide), PLLA = poly(L-lactic acid), PNIPAAm = poly(N-isopropylacrylamide), PVA = poly(vinyl alcohol), PVB = poly(vinyl butyrate), SCPL = solvent-casting particulate-leaching, SLA = stereolithography, and SLS = selective laser sintering.

# of phases	Bone	Cartilage	Interface	Fabrication	Year	Ref
7	PCL/30% HAp	PCL	PCL/ (25/20/15/10/5%) HAp	SLS	2017	[160]
2	PECDA, PAAm, PEGDA	CSMA, PNIPAAm	calcium gluconate and alginate	phase separation; thermal crosslinking	2017	[161]
3	PCL	PCL	N/A	electrospinning; FDM	2017	[162]
2	methacrylated triblock (F127-P123)/CaP	methacrylated triblock (F127-P123)	N/A	FDM	2017	[163]
2	PVA/HAp	PVA	N/A	Electrophoresis; freeze-drying	2017	[164]
2	PVA/β-TCP	PVA	N/A	SCPL; freeze-drying	2017	[165]
3	PCL/30% HAp	PCL	PCL/15% HAp	FDM	2018	[166]
2	PCL/10% graphene	N/A	N/A	SCPL	2018	[167]
2	alginate/HAp	alginate/hyaluronic acid	N/A	diffusion controlled, directed ionotropic gelation	2018	[168]
3	PEGDA/A6ACA/CaP	PEG-DA	PEG-DA	freeze-drying	2018	[169]
2	chitosan/alginate/HAp	chitosan/hyaluronic acid	N/A	TIPS; freeze-drying	2019	[170]
2	PLGA/tyramine	PLGA/tyramine	N/A	SCPL; freeze-drying	2019	[171]
3	silicon-zirconium SZ2080	silicon-zirconium SZ2080	silicon-zirconium SZ2080	stereolithography	2019	[172]
2	PDLLA/camphene	PDLLA	N/A	SCPL; freeze-drying	2019	[173]
2	β-TCP	PEG-DA	N/A	stereolithography	2019	[174]

1.5. Recent Materials-Guided Approaches.

A variety of instructive scaffold designs have emerged in recent years that target healing of OCDs using a synthetic materials-guided regenerative engineering approach (**Table 1-1**). Given the known influence of morphological features on directing cell behavior,[30-34] scaffolds with spatially controlled morphology and chemistry are expected to improve regeneration, particularly in combination with materials whose chemical and physical properties are known to be instructive. In this section, we highlight recent examples of osteochondral scaffolds that have leveraged different fabrication strategies (**Figure 1-3**).
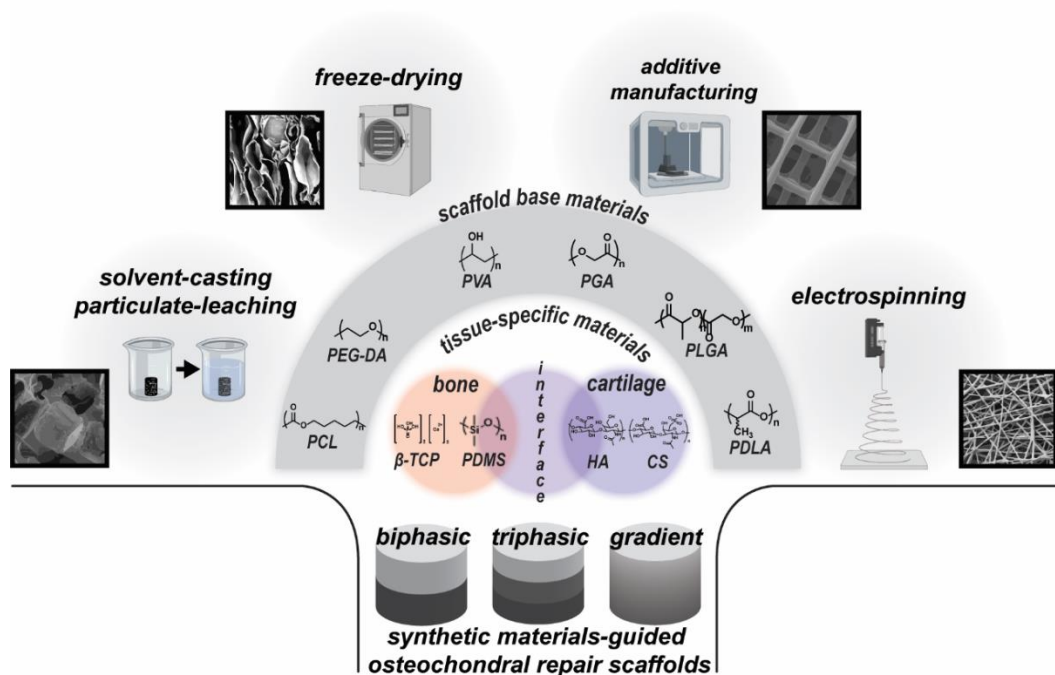
Figure 1-3. Synthetic materials-guided osteochondral regeneration has utilized four major fabrication techniques - SCPL, freeze-drying, additive manufacturing, and electrospinning - with a variety of materials in configurations of biphasic, triphasic, or gradient scaffolds.

1.5.1. Electrospinning

Electrospinning involves charging and drawing a viscous polymer solution into fibers at the micro- or nanometer scale onto a collector of opposite polarity.[175] Deposition of these fibers results in a nonwoven fibrous mesh with tunable porosity, interconnectivity, mechanical properties, and surface area. Extensive research has demonstrated the fabrication of complex fiber shapes (e.g., solid, helical, and hollow) via phase separation of two materials spun from the same solution and controlled alignment (e.g., mesh, parallel, and patterned) by using unique counter electrode arrangements and movements.[176] Utilization of magnetically responsive polymers affords the opportunity for magnetically assisted fabrication, in which fibers can be aligned with direction of an applied magnetic field.[177, 178] Electrospinning is a versatile fabrication technique suitable for many polymers, including synthetic and natural polymers and combinations of the two. Furthermore, bioceramics can be electrospun either as a sol−gel or as a composite with a polymer in solution.[179] A number of new studies have utilized electrospinning to prepare instructive osteochondral scaffolds that span from the articular cartilage to the cancellous bone.[176, 180] Most often, these scaffolds have been formed by combining individually prepared, discrete electrospun layers using solvent-bonding, freeze-drying, or other methods. For example, Yunos et al. formed a biphasic scaffold by electrospinning poly(D,L-lactide) (PDLLA) (the cartilage phase) of varying thicknesses (up to 150 µm) onto a bioglass foam (the bone phase).[181] This scaffold was able to support chondrocytic proliferation on the fibers and graded HAp formation as a function of PDLLA thickness (during exposure to simulated body fluid). Thus, while a biphasic scaffold, the formation

17

of mineralized fibers at the interface paralleled the calcified cartilage layer of the native osteochondral interface. As this fabrication strategy advances for OCD regenerative strategies, magnetically assisted fabrication may help to form tighter interfaces between discrete layers and complex spatially aligned fibers that can be used to form more biomimetic phases.

1.5.2. Solvent-Casting Particulate-Leaching

Solvent-casting particulate-leaching (SCPL) is useful to produce materials with tunable pore sizes and shapes. In SCPL, a polymer is dissolved in a solvent, introduced to an insoluble porogen, and then cross-linked and/or solvent evaporated. Following leaching of the porogen, a network of pores is produced whose size and shape are dictated by the porogen. A wide variety of salts or other materials have been utilized as porogens for SCPL (e.g., NaCl salt, paraffin beads, and gelatin beads) and chosen for properties such as their solubility, shape, size, and/or thermal stability. By first fusing the porogen template, interconnected porosity may also be achieved. For instance, we utilized a fused salt template, prepared by the addition of a small quantity of water to sieved NaCl crystals, to form interconnected macropores of tunable size in PEG-DA hydrogels and PCLDA shape memory polymers for osseous scaffolds.[182, 183]

The use of SCPL to prepare instructive osteochondral scaffolds has largely relied on preparing biphasic or multiphasic scaffolds whose differing pore sizes or shapes are leveraged to direct cell behavior. For example, in Mahapatra et al., a biphasic PDLLA scaffold was prepared with a small salt porogen for the dense layer (cartilage phase) whereas the nanofibrous layer (bone phase) was created with a large salt porogen as well

as with camphene to induce phase separation, creating two distinct layers.[173] Scaffaro et al. also prepared a biphasic scaffold using leachable porogens but utilized melt mixing rather than solvent-casting.[184] Each of the mixtures of polymer and porogen - PLA/larger-sized salt and PCL/PEG/smaller sized-salt - were sequentially melt-mixed and compression molded into cylindrical layers, followed by fusing the layers together with a heat treatment and last leaching the porogens. Tang et al. created a PLGA triphasic scaffold with graded pore size by utilizing gelatin-microspheres of three sizes to form a trilayered porogen template, fused by the addition of a small amount of ethanol/water solution as well as heat treatment.[185]

1.5.3. Freeze-Drying

Freeze-drying (including also thermally induced phase-separation [TIPS]), wherein ice acts as the porogen, is also utilized to fabricate porous scaffolds.[186] This method involves the freezing of an aqueous polymeric solution and subsequent sublimation of the ice. Upon formation and growth of ice, phase separation occurs as polymer chains are excluded and thereby form an interconnected network.[187] The utility of freeze-drying is attributed to the lack of harmful solvents as well as the ability to refine scaffold morphology, namely, pore directionality and pore homogeneity. For instance, to control pore directionality, the cooling source can be introduced at a specific portion of the scaffold, causing freezing to travel from one point to another and thus producing pores oriented in that direction. Also, to influence pore homogeneity, cooling rate can be changed, wherein faster rates lead to heterogeneous pore sizes due to nonuniform ice nucleation, and slower rates lead to a uniform pore network. Pore size can be influenced

based on precise control of freezing time, temperature, material, and other strategy-specific variables.[188-190]

Freeze-drying has been utilized to create instructive scaffolds for osteochondral regeneration having different degrees of complexity. Erickson et al. designed a biphasic scaffold by layering two distinct polymer solutions and subsequently freeze-drying.[170] The cartilage layer was a 4% chitosan and hyaluronic acid (CHA) mixture, and the bone layer consisted of 6% chitosan and alginate (CA) and 0.5% hydroxyapatite. For fabrication, the bone layer mixture was added over the refrigerated cartilage layer mixture, centrifuged to remove bubbles and create a tight interface, and then refrigerated, frozen, and lyophilized. Kang et al. designed a more complex trilayer scaffold by a similar method but where PBS was used to wash out frozen crystals from pores.[169] This scaffold consisted of a cartilage layer of PEG-DA, a transition layer of PEG-DA with pore anisotropy, and a mineralized bone layer of PEG-DA, CaP, and N-acryloyl 6-aminocaproic acid (A6ACA). The bottom two layers were fabricated by polymerizing the first layer of PEG-DA and A6ACA at −20 °C for 24 h, followed by adding the second PEG-DA layer on top and polymerizing at the same temperature. The resulting lower layer contained smaller, uniform crystals due to the 24 h uniform freeze, while the middle layer had columnar pore structures due to the frozen gel beneath it. The resulting bilayer scaffold was incubated in simulated body fluid for mineralization and subjected to cell culture. Finally, to create the final trilayer scaffold, a small amount of cell-laden PEG-DA was photopolymerized on the upper surface of the bilayer scaffold. This study showcased the ability to control pore directionality, which can mimic the anisotropic nature of chondral tissue. Such an approach may be utilized to

20

prepare instructive osteochondral scaffolds that mimic tissue collagen fiber alignment with the potential to achieve interfacial complexity.

1.5.4. Additive Manufacturing

With the emergence of additive manufacturing (i.e., 3D-printing), scaffolds may be prepared with a high degree of morphological and compositional complexity through computer-aided design (CAD). The formation of printed structures, most often in a layer-by-layer manner, affords a high degree of spatial control to prepare multiple, unique zones.[191] A wide variety of materials can be 3D-printed, including thermoplastics, hydrogels, polysaccharides, ceramics, and composites merged by melting, UV-crosslinking, particle fusion, and more.[192] Recently, instructive osteochondral scaffolds have utilized three major types of 3D printing, including stereolithography, fused deposition modeling, and selective laser sintering.[191]

Extrusion based 3D printing (i.e., fused deposition modeling) is a process in which a melt or gel "ink" is deposited in a layer-by layer fashion.[191] This method has been utilized for the generation of osteochondral scaffolds with spatially controlled composition and morphology. For instance, Bittner et al.[166] utilized multiple nozzles to coextrude three mixtures of PCL and HAp. A triphasic scaffold was prepared with zones of different pore sizes and HAp concentrations: osseous phase (900 μm, 30% HAp), transition phase (500 μm, 15% HAp), and cartilage phase (200 μm, 0% HAp). While bioprinting has emerged as a type of fused deposition 3D printing, wherein cells are incorporated into the resin prior to printing, the typical inclusion of growth factors does not constitute a synthetic materials-driven approach.[193] However, polysaccharide printing has been achieved,[194] and

recently, a method for bioprinting of growth-factor free materials as gradients has been reported in Idaszek et al.[195] This involved the controlled rapid mixing of multiple bioinks prior to extrusion, producing gradients representing the transition from bone to cartilage.

Stereolithography (SLA), also known as optical fabrication or photosolidification, uses the solidification of liquid resins to form complex structures. This process typically involves a bath of a liquid resin that is solidified in a layer-by-layer fashion with a focused laser beam. Favorably for tissue engineering scaffolds, this strategy consistently produces structures with higher resolution than traditional fused deposition modeling, as the determination is made by the optical spot size of the laser rather than the extruding nozzle size.[196] However, the use of a resin bath typically limits printing to a single material, thus hindering printing of scaffolds with multiple phases in a single step. More recently, multimaterial systems have been developed,[197] which could provide a format for SLA printing of osteochondral scaffolds. For example Wu et al. reported a scaffold composed of PEG-DA and β-TCP that was formed by multimaterial mask projection stereolithography, a process that effectively allows the use of multiple materials in one scaffold.[174] This was accomplished by a bottom-up process designed to print with "material A" (β-TCP), wash the scaffold to remove liquid resin, and then print with "material B" (PEG-DA), resulting in a well-integrated biphasic scaffold. Another promising technology in stereolithography is the use of two-photon polymerization. This technology induces resin polymerization by the absorption of two photons using a femtosecond laser, allowing for an extremely high precision cure. This permits a fabrication feature size as small as 100 nm. Strategies using this method have shown

promise in tissue engineering.[198] Recently, Maciulaitis et al. utilized two-photon polymerization to form an osteochondral repair scaffold of a material deemed SZ2080 [consisting of 20% "inorganics" (i.e., methacryloxypropyl trimethoxysilane and zirconium propoxide) and 80% organics (i.e., 2-(dimethylamino)ethyl methacrylate)].[172] The scaffold was designed with hexagonal pores, set at a diameter of 100 μm and height of 51 μm, displaying extremely precise morphological control.

Selective laser sintering (SLS) is an additive manufacturing strategy that utilizes a high-power laser to fuse particles of a set size and composition. This technique is conducive for gradient production as it is completed layer-by-layer, wherein a layer of particle powder is added and then fused, and the process is repeated. Furthermore, the complex surfaces and pore shapes in these scaffolds are more like that of native tissue, rather than the geometrical and consistent alignment of extrusion printed scaffolds. Du et al. highlights the use of SLS to fabricate a unique gradient-based scaffold of PCL and HAp.[160] This study utilized PCL microspheres and PCL microspheres modified with HAp nanoparticles, both with diameters of ∼100 μm. Decreasing ratios of PCL/HAp to PCL microspheres were added manually at designated positions along the fabrication process. Thus, a gradient of HAp was developed, from 30% modified to 0% at 5% increments making for seven seamless layers with interconnected pore sizes in the range 400−500 μm.

1.6. Conclusions

Synthetic polymer scaffolds have the potential to guide the regeneration of complex osteochondral tissues through their instructive chemical and physical properties.

Herein, we have highlighted how synthetic material-based scaffolds have been utilized in recent years for osteochondral tissue engineering. Early work relied on biphasic scaffolds, merged across a hard interface, with only two synthetic materials-guided examples advancing to clinical studies. Thus, recent efforts have focused on developing instructive, multiphasic scaffolds with spatially complex chemical and morphological features by leveraging advanced fabrication methods. In doing so, the complex osteochondral interface, consisting of calcified cartilage and the subchondral bone plate, is better recapitulated and anticipated to enhance biomechanical functionality. As exemplified herein, further refinements to the chemical and morphological features, along with a greater degree of spatial control, are expected to enhance instructive behavior. To potentially increase the potency and efficacy of such synthetic-based osteochondral scaffolds, the use of coculturing (i.e., controlling culture of multiple cell lineages in separate scaffold zones),[134, 199-201] bioreactors (i.e., dynamic *in vitro* environment to mimic native environment),[202-204] and microcarriers (i.e., 100−400 μm particles that facilitate cell growth/expansion)[201, 205, 206] may be employed. Microfluidic advancements represent significant promise in increased understanding of the microenvironments necessary for osteochondral regeneration.[207] Mechanically robust double network (DN) hydrogels may provide an opportunity to produce osteochondral scaffolds with surfaces that can withstand articulating forces prior to tissue regeneration.[57, 208-212] New synthetic materials-guided osteochondral repair strategies are constantly emerging, and those that further address the spatial and compositional complexities of the native tissue will significantly advance the potential of the field to treat OCDs. While protein-based scaffolds have been

widely studied and are known to be instructive, scaffolds that exclude proteins rely solely

on material properties to direct regeneration and therefore isolate the potency of these cues

such that they can be leveraged more effectively.

CHAPTER II

INCORPORATION OF A SILICON-BASED POLYMER TO PEG-DA TEMPLATED

HYDROGEL SCAFFOLDS FOR BIOACTIVITY AND OSTEOINDUCTIVITY[†]

2.1. Overview

A scaffold that is inherently bioactive, osteoinductive and osteoconductive may guide mesenchymal stem cells (MSCs) to regenerate bone tissue in the absence of exogenous growth factors. Previously, we established that hydrogel scaffolds formed by crosslinking methacrylated star poly(dimethylsiloxane) (PDMS$_{star}$-MA) with diacrylated poly(ethylene glycol) (PEG-DA) promote bone bonding by induction of hydroxyapatite formation (''bioactive'') and promote MSC lineage progression toward osteoblast-like fate (''osteoinductive''). Herein, we have combined solvent induced phase separation (SIPS) with a fused salt template to create PDMS$_{star}$-PEG hydrogel scaffolds with controlled PDMS$_{star}$-MA distribution as well as interconnected macropores of a tunable size to allow for subsequent cell seeding and neotissue infiltration (''osteoconductive''). Scaffolds were prepared with PDMS$_{star}$-MA of two number average molecular weights (M$_n$s) (2k and 7k) with varying PDMS$_{star}$-MA:PEG-DA ratios and template salt sizes. The distribution of PDMS$_{star}$-MA within the hydrogels was examined as well as pore size, percent interconnectivity, dynamic and static moduli, hydration, degradation and *in vitro*

[†] Reprinted with permission from "Incorporation of a Silicon-based Polymer to PEG-DA Templated Hydrogel Scaffolds for Bioactivity and Osteoinductivity" by Frassica. M.T., Jones. S.K., Diaz-Rodriguez, P., Hahn, M.S., and Grunlan, M.A., 2019. *Acta Biomater.,* 99, 100-109, Copyright 2019 Elsevier Ltd.

bioactivity (i.e. mineralization when exposed to simulated body fluid, SBF). Finally, cell culture with seeded human bone marrow-derived MSCs (hBMSCs) was used to confirm non-cytotoxicity and characterize osteoinductivity. Tunable, interconnected macropores were achieved by utilization of a fused salt template of a specified salt size during fabrication. Distribution of $PDMS_{star}$-MA within the PEG-DA matrix improved for the lower M_n and contributed to differences in specific material properties (e.g. local modulus) and cellular response. However, all templated SIPS $PDMS_{star}$-PEG hydrogels were confirmed to be bioactive, non-cytotoxic and displayed $PDMS_{star}$-MA dose-dependent osteogenesis.

2.2. Introduction

Bone tissue regeneration holds potential to be achieved with an instructive scaffold whose chemical and physical properties direct the behavior of associated mesenchymal stem cells (MSCs), even in the absence of exogenous growth factors.[25, 27, 28] This "materials-based" approach to bone regeneration would mitigate cost and risks of off-target responses associated with added growth factors.[213-215] Ideally, such a scaffold would be osteoinductive (to stimulate differentiation of cells into the bone-forming lineage), bioactive (to promote bonding with adjacent bone tissue by hydroxyapatite mineralization) and osteoconductive (to permit bone growth on its surface or down into pores).[68, 69, 101] Osteoconductivity may be obtained when scaffolds are produced with optimized pore size (i.e. between 200 and 400 µm) as well as pore interconnectivity.[16, 74, 113] Approaches to achieve osteoinductivity and bioactivity have often relied on the incorporation of inorganic and hydrophobic materials, particularly bioactive glasses and ceramics used as

27

fillers.[44, 85-87] However, such composite scaffolds typically suffer from low fracture toughness, limited or low resorption rates and a lack of ideal pore features.[101, 103] Scaffolds that mitigate these issues while achieving these instructive behaviors would represent a significant advancement in bone regeneration.

It has been demonstrated that silicon plays a key role in bone mineralization and gene activation,[108, 109] thus prompting the use of certain glasses or ceramics. Instead, we have demonstrated that bioactivity and osteoinductivity could be obtained by introducing silicon-based, inorganic polymer to a conventional organic hydrogel.[88, 216] Specifically, inorganic star poly (dimethylsiloxane) methacrylate (PDMS$_{star}$-MA) was introduced to organic poly (ethylene glycol) diacrylate (PEG-DA) to form PDMS$_{star}$-PEG hydrogels,[216, 217] up to a 30:70 wt/wt% ratio of PDMS$_{star}$-MA:PEG-DA. As ''biological blank slates'', resisting non-specific protein and cell adhesion, PEG-DA hydrogels have been extensively studied as instructive scaffolds.[48, 218] To control cell adhesion, cell adhesive ligands, such as the peptide RGDS, can be readily introduced.[219] In this way, specific material properties (e.g. stiffness and hydration) may be tuned and readily correlated to associated cellular responses. However, PEG-DA hydrogels lack inherent osteoinductivity and bioactivity. On the other hand, the PDMS$_{star}$-PEG hydrogels maintained the biological blank slate nature of PEG-DA hydrogels but also induced osteogenic responses of photoencapsulated bone marrow-derived mesenchymal stem cells (BMSCs).[88, 216, 217] Due to the insolubility of PDMS$_{star}$-MA in the aqueous precursor solution, it was heterogeneously distributed as microdroplets throughout the PEG-DA matrix.[217] Thus, to improve PDMS$_{star}$-MA distribution, these hydrogels were later prepared via solvent induced phase separation

28

(SIPS) by employing an organic solvent (dichloromethane, DCM) to prepare the precursor solutions.[216, 220] Following sequential UV-cure, removal of the DCM and hydration, the resulting SIPS PDMS$_{star}$-PEG hydrogels revealed improved PDMS$_{star}$ distribution as well as the presence of pores of increased size (up to 200 µm) with PDMS$_{star}$-MA content. However, these pores lacked interconnectivity necessary for cell seeding and eventual neotissue infiltration.[216]

Herein, we sought to produce instructive PDMS$_{star}$-PEG hydrogels – having controlled porosity and pore interconnectivity as well as enhanced distribution of PDMS$_{star}$-MA – by fabrication via SIPS in combination with a fused salt template. Tight control over pore size and maximized pore interconnectivity has been shown to be achieved with fused salt templates.[221, 222] Our recent work has shown that templating is effective to prepare SIPS PEG-DA hydrogels with interconnected macropores of tunable sizes >100 µm[182]; however, these hydrogels remain lacking in osteoinductivity and bioactivity. Thus, we prepared a series of templated SIPS PDMS$_{star}$-PEG-DA hydrogels based on different number average molecular weights (M$_n$) of PDMS$_{star}$-MA (2k and 7k). These were incorporated into a DCM-based precursor solution at increasing wt/wt% ratios (0:100, 10:90, 20:80, and 30:70) of PDMS$_{star}$-MA to PEG-DA (M$_n$ = 3.4k). The distribution of PDMS$_{star}$-MA was evaluated along with the ability to achieve tunable pore size and pore interconnectivity. The effect of templated SIPS hydrogel composition on hydration and modulus was examined, as these material properties are known to influence cellular behavior.[35, 36, 41, 46] The bioactivity and degradation rates were also investigated. Scaffolds were further evaluated to confirm non-cytotoxicity and degree of osteogenic

capacity after seeding with human bone marrow-derived mesenchymal stem cells (hBMSCs).

2.3. Materials and Methods

2.3.1. Materials

1-vinyl-2-pyrrolidinone (NVP), 2,2-dimethyl-2-phenylacetophenone (DMAP), acryloyl chloride, allyl methacrylate, calcium chloride, dibasic potassium phosphate, HCl (12M), hexamethyldisilazane (HMDS), magnesium chloride hexahydrate, magnesium sulfate, Nile red, NMR grade deuterated chloroform (CDCl$_3$), poly (ethylene glycol) 3350 (PEG-3350), potassium carbonate, potassium chloride, silica gel, sodium bicarbonate, sodium chloride (NaCl; salt), sodium hydroxide (NaOH), sodium sulfate, triethylamine, trifluoromethanesulfonic acid (triflic acid), tris-hydroxymethyl aminomethane, Triton X-100 (0.1%) and all solvents were obtained from Sigma-Aldrich. HPLC-grade toluene, dichloromethane, and NMR grade CDCl$_3$ were dried over 4Å molecular sieves. Salt was sieved (ASTME-11 Specification, No.40, 425 µm opening; No.60, 250 µm opening) to obtain the following salt sizes: ''small salt'' (SS): 181 ± 29 µm, ''medium salt'' (MS): 268 ± 35 µm and ''large salt'' (LS): 459 ± 69 µm. Average salt sizes were calculated using ImageJ software, as done previously.[182] Silver nitrate and sodium thiosulfate were obtained from American Mastertech. Fetal bovine serum (16.5%; FBS) was obtained from Atlanta Biologicals. Glutamax, Minimum Essential Medium Alpha (α-MEM), Penicillin-Streptomycin and 1% glutamine (Glutamex) were obtained from Gibco. Phosphate-buffered saline (1x without Ca and Mg; PBS) and Dulbecco's Modified Eagle Media (DMEM) was obtained from Corning. Octamethylcyclotetrasiloxane (D4), Pt-

divinyltetramethyldisiloxane complex in 2wt% xylene (Karstedt's catalyst), and tetrakis(dimethylsiloxy)silane (tetra-SiH) were obtained from Gelest. Activated carbon, buffered formalin, DAPI, dialysis cassettes (3.5k MWCO), anhydrous ethyl ether, and rhodamine phalloidin were obtained from Fisher Scientific. Von Kossa staining kit was obtained from American Mastertech Scientific. Acryloyl-PEG-succinimidyl valerate was obtained from Laysan Bio, Inc. Dulbecco's phosphate-buffered saline (DPBS) was obtained from Lonza. Peptide RGDS was obtained from Bachem. Cytotoxicity detection kit (LDH) was obtained from Roche, multiplex immunoassay kits were obtained from R&D Systems and the Pico-Green assay kit was obtained from Invitrogen.

2.3.2. Synthesis

2.3.2.1. PDMS$_{star}$-MA Synthesis

PDMS$_{star}$-MA (M_n = 2k and 7k g/mol) was prepared as previously reported.[216, 217] First, silane (SiH)-terminated PDMS$_{star}$ was prepared by the acid-catalyzed equilibration of D$_4$ ("2k": 30.0 g, 101.4 mmol; "7k": 29.9 g, 101.0 mmol) with tetra-SiH ("2k": 7.8 g, 23.8 mmol; ''7k": 1.1 g, 3.4 mmol) utilizing triflic acid (60 mL) and subsequent neutralization with HMDS (0.15 g, 0.93 mmol). The resulting PDMS$_{star}$-SiH (for "2k" and "7k") were each precipitated three times in toluene/methanol and dried under reduced pressure, resulting in a colorless liquid. Next, photoreactive groups were added via hydrosilylation to the terminal ends of each arm of PDMS$_{star}$-SiH ("2k": 7.0 g, 2.5 mmol; "7k": 7.0 g, 0.53 mmol) by Pt-catalyzed [Karstedt's catalyst (50mL)] reaction with allyl methacrylate ("2k": 3.6 mL, 26.8 mmol; "7k": 0.314 mL, 2.33 mmol) in toluene (30 mL). Both M_n's of PDMS$_{star}$-MA were obtained after a 2h activated carbon spin and flash

column chromatography. The structures of each M_n of PDMS$_{star}$-SiH and PDMS$_{star}$-MA were confirmed by ^{1}H NMR and was in agreement with that previously reported.

2.3.2.2. PEG-DA Synthesis

PEG-DA (M_n = 3.4k g/mol) was prepared as previously reported.[217] PEG-3350 (23.5 g, 7.0 mmol) was dissolved in DCM, then triethylamine (1.95 mL, 14.0 mmol) and subsequently acryloyl chloride (2.27 mL, 28.0 mmol) were added dropwise to the solution and allowed to react overnight. HCl was removed by 2M K_2CO_3 wash in a separatory funnel. The reaction was then dried in the organic phase with $MgSO_4$ spin and precipitated in anhydrous ethyl ether. After vacuum filtration to obtain the white solid, PEG-DA was vacuum dried to remove residual solvent. The structure was confirmed by ^{1}H NMR and was in agreement with that previously reported.

2.3.2.3. ACRL-PEG-RGDS Synthesis

ACRL-PEG-RGDS was synthesized as previously reported.[88] The cell adhesion peptide RGDS was reacted with acryloyl-PEG-SVA at a 1:1M ratio for 2 h in 50 mM sodium bicarbonate buffer. ACRL-PEG-RGDS was purified by dialysis, lyophilized, and stored at -20°C under nitrogen (N_2). ACRL-PEG-RGDS was included in all hydrogels utilized for cell culture at 1 mmol/mL of precursor solution.

2.3.3. NMR

^{1}H NMR spectra were obtained on an 'INOVA500' 500 MHz spectrometer operating in the Fourier transform mode. Solutions of 5% (w/v) CDCl$_3$ were used to obtain spectra. Residual CHCl$_3$ served as an internal standard.

2.3.4. Salt Template Formation

Salt templates were formed with each of the three average salt sizes: "small salt" (~180 µm), "medium salt" (~270 µm) and "large salt" (~460 µm). Molds for making the salt template and subsequently curing the precursor solution were prepared as follows. One end of a borosilicate glass tube (5/8" OD, 1/2" ID, 1.5" H) was covered with aluminum foil, pushed into a custom Teflon cap (1" OD, 5/8" ID) that contained a small hole (0.05" D) directly through its center and then tightly wrapped with Parafilm to secure the glass tube to the cap (**Figure A-1**). Salt of the designated size (16 g) was mixed gently with 5 wt% DI water (using a metal spatula) in a 25 mL beaker and 3.5 g of the mixture added to the mold. The salt mixture was then compacted into the mold using a flat-ended glass rod, covered with Parafilm, and centrifuged 5 min at 2000 rpm within a 50 mL centrifuge tube (Eppendorf 5810R centrifuge, A-4-62 rotor). Afterwards, the Parafilm cover was removed and the fused template allowed to air dry at room temperature (RT) for 24 h within the glass mold.

2.3.5. Templated Hydrogel Fabrication

DCM-based precursor solutions were prepared containing 30 wt% total macromer (based on total solution mass) with increasing wt/wt% ratios of PDMS$_{star}$-MA to PEG-DA: 0:100 (PEG-DA control), 10:90, 20:80, and 30:70. Photoinitiator solution (30 wt% DMAP in NVP) was added at 100 mL/g of macromer. Solutions were vortexed in a sealed vial for 1 min after addition of each component. The precursor solution (~1.5 mL) was immediately deposited atop the aforementioned dried salt template via syringe. After ~30 s, the aluminum foil at the base of the mold was punctured through the hole in the Teflon

cap. Using PVC tubing (3/8" ID, 9/16" OD) held against the top of the glass mold, compressed air was used to gently force the solution throughout the salt template until the solution began to exit through the cap hole. Removal of the air in let caused the flow of precursor solution to cease. The filled mold was UV-cured for 15 min (12 min standing on Teflon cap and 3 min standing on the glass top) via exposure to a UV-transilluminator (6 mWcm^2, 365 nm). After air-drying 24 h to evaporate the solvent, the cylindrical specimen was removed from the mold and sectioned into 1.2 mm thick discs using a vibratome (Leica VT1000S; cutting speed = 1.75 mm/s; frequency = 30 Hz). Only discs from the central portion of the cylinder were used for testing, discarding ~4 mm from each end. Discs were soaked in DI water for 48 h on a rocker table (100 rpm; water changes 3x daily) to leach the salt template and swell the hydrogels to their final hydrated form (~15 mm diameter, ~1.5 mm thick). Discs were allowed to soak an additional 72 h prior to testing, for which they were punched to a desired size (8 or 13 mm) from the central region of the disc using a die.

2.3.6. Sol Content

Discs (N = 5; 13 mm diameter) were air dried 30 min then placed in an open scintillation vial and dried at RT in a vacuum oven (14.7 psi, 24 h). Dried discs were weighed (W_d1), placed in a new scintillation vial with 10 mL of DCM, and set on a rocker table (100 rpm) for 48 h. Removed discs were placed in new scintillation vials, allowed to air dry (30 min) and dried again at RT in the vacuum oven (14.7 psi, 24 h). The final weight was taken (W_d2) and the sol content calculated as $[(W_d1 - W_d2)/Wd1] \times 100$.

2.3.7. Equilibrium Swelling

Discs (N = 5; 13 mm diameter) were each placed in a sealed vial with 15 mL of DI water on a rocker table (100 rpm) for 48 h at RT. Discs were then removed and weighed (W_s). Discs were dried (14.7 psi, 60°C, 24 h) and weighed again (W_d). Equilibrium swelling ratio was calculated as $(W_s - W_d)/W_d$.

2.3.8. Distribution of PDMS$_{star}$-MA and Pore Morphology

2.3.8.1. Confocal Laster Scanning Microscopy (CLSM)

Discs (8 mm diameter) were soaked for 24 h in 60 mL Nile Red solution, followed by daily changes with PBS for 3 days. Nile red solution contains 75 mL of a solution containing 20 mg Nile red and 1 mL methanol mixed into 8 mL of DI water and added to 120 mL of PBS, as previously reported.[216] Discs were placed in a coverglass-bottom chamber and imaged on an Olympus FV1000 confocal microscope, equipped with a UPLSAPO 10x/0.4 objective. Excitation and emission were 488 nm and 500–600 nm, respectively. The confocal aperture was set to 1 Airy unit. Z-stacks (80 slices) were acquired with a 4.0 µm step. Confocal zoom and resolution setting resulted in XY pixel size of 2.485 µm. Representative slices of the stacks were exported. The fluorescence images were pseudo-colored green. Brightfield imaging was conducted simultaneously and used to measure hydrated pore size. Images were taken of three locations on two different samples for each salt size (20:80 wt/wt% PDMS$_{star}$-MA:PEG-DA) with one pore measured per image (N = 6). ImageJ Software was used to calculate pore size, determined by the mean of the diagonal and central cross-section.

2.3.8.2. Scanning Electron Microscopy (SEM)

Discs (8mm diameter) were allowed to air dry (30 min), and dried in a vacuum oven (14.7 psi, 24 h, RT). Dried discs were subjected to Au-sputter coating (Cressington Sputter Coater 108) and viewed with a field emission scanning electron microscope (FE-SEM; JEOL NeoScope JCM-5000) at an accelerated electron energy of 10 keV. Pore size was measured using ImageJ software by the same method described in Section 2.3.8.1.

2.3.8.3. Percent Interconnectivity

Discs (N = 3; 13 mm diameter) were evaluated to determine interconnectivity with a water wicking procedure adapted from Bencherif et al.[223] Each disc was soaked for 24 h in DI water on a rocker table (100 rpm) to ensure no air bubbles existed within pores. Discs were removed and weighed in a glass Petri dish (W_{total}). A folded Kimwipe was then gently pressed on the disc for 1 min to wick away the interconnected volume, and the disc was weighed again ($W_{interconnected}$). Percent interconnectivity was calculated as $[(W_{total} - W_{interconnected})/W_{total}]$ x 100.

2.3.9. Mechanical Properties

2.3.9.1. Bulk Compressive Young's Modulus and Damping – Static and Dynamic Mechanical Analysis

Discs (8 mm diameter) were used for the measurement of Young's modulus (N = 4) as well as dynamic moduli (N = 8) using a dynamic mechanical analyzer (DMA; TA Instruments Q800) with a parallel-plate compression clamp equipped with plates of 40 mm (bottom) and 15 mm (top). Hydrated discs were placed between the plates and several drops of DI water were dropped onto the hydrogel to maintain hydration. Analyses were

conducted at RT. For static testing, samples were tested at RT in a controlled strain rate mode (20%/min to 12% strain) with a preload force of 0.1N. Young's modulus was obtained from the slope of the linear portion of the stress-strain curve (1–5%). For dynamic testing, samples were tested using a multi-frequency strain mode (1–30 Hz) with an amplitude of 10 µm and preload force of 0.1N. The obtained values of loss (G'')and storage (G') were used to calculate tan δ (i.e. damping).

2.3.9.2. Local Young's Modulus – Atomic Force Microscopy (AFM)

Discs (N = 2; 8 mm diameter) were used to measure local Young's modulus using a Dimension ICON AFM (Bruker) with a Nanoscope V controller. A modified silicon nitride probe (NovaScan, USA) having a nominal spring constant of 0.6 N/m with a 5 mm diameter bead attached to the cantilever was used. Standard detector calibration was performed on a clean mica disc to determine deflection sensitivity. Standard thermal tuning calculated a spring constant of ~0.75–0.9 N/m. For each sample, hydrogels were fixed to 15 mm metal AFM specimen discs (Ted Pella, Inc.) with water droplets added to the sample surface to maintain hydration. Indentation was carried out at the pore walls using 1 Hz loading rates. The ramp size was 1 mm and the indentation force was 15 nN. Young's modulus values were calculated using Nanoscope Analysis software (Bruker) with a Hertzian fit model after baseline correction and boxcar filter. A sample Poisson's ratio of 0.5 was used. Individual force-displacement curves were taken 6 times at each sampled point of the hydrogel, with 5 total points from 2 hydrogels sampled.

2.3.10. Accelerated Degradation

Discs (N = 3 per timepoint; 8 mm diameter) underwent accelerated degradation analysis. All hydrogel discs were vacuum dried (14.7 psi, 12 h) and weighed. Each disc was then placed in a 1 dram vial with 1 mL of 0.05M NaOH and stored in a shaking incubator (100 rpm, 37 °C). At 12 h time points, one disc was removed, dried (14.7 psi, 12 h), and weighed to determine mass loss percentage. At each timepoint, solutions for all samples were exchanged with new 0.05M NaOH.

2.3.11. Bioactivity

2.3.11.1. Simulated Body Fluid (SBF) Soak

SBF was fabricated as detailed by Kokubo et al. and in previous studies.[216, 224] Individual discs (N = 2; 8 mm diameter) were placed in sealed 50 mL centrifuge tubes containing 40 mL of 1x SBF and incubated in a water bath at 37 °C. Discs were removed after 4 weeks, washed with DI water and vacuum dried (14.7 psi, 24 h). Dried hydrogels were subjected to SEM imaging (Section 2.3.8.2)and X-ray diffraction spectroscopy (Section 2.3.11.2).

2.3.11.2. X-ray diffraction spectroscopy (XRD)

Powder X-ray diffraction data was collected on a Bruker D8 diffractometer fitted with a LynxEYE detector. The X-ray source was a 1 kW Cu X-ray tube maintained at an operating current of 40 kV and 25 mA (Bragg-Brentano geometry; scan range 3–70°; step size: 0.015°).

2.3.12. Cell Culture

Bone marrow derived human mesenchymal stem cells (hBMSCs) were obtained from the Texas A&M Institute for Regenerative Medicine. By flow cytometry, hBMSCs tested positive (>95%) for CD29, CD44, CD49c, CD59, CD73a, CD90, CD105, CD146, CD147, CD166, and HLA-I:ABC and negative (<5%) for CD3, CD11b, CD14, CD19, CD34, CD36, CD45, CD49b, CD49d, CD79a, CD106, CD184, CD271, HLA-II:DR, and HGFR (c-Met). hBMSCs were expanded in α-MEM supplemented with 16.5% FBS and 1% glutamine. Twenty-four hr prior to seeding, cells at passage 4 were transitioned to DMEM containing 10% FBS and 1% Penicillin/Streptomycin (P/S)).

2.3.13. Seeding and Culture of Scaffold Constructs

Scaffolds were fabricated with ACRL-PEG-RGDS (Section 2.3.2.3) and cut to 8 mm discs. Scaffolds were seeded with hBMSC s at $5x10^6$ cells/mL and cultured at 37 °C and 5% CO2 in DMEM containing 10% FBS and 1% P/S. Culture medium was exchanged every 2 days through the duration of culture. Osteogenic supplements were not utilized so as to assess the intrinsic osteogenic potential of the scaffolds.

2.3.14. Cytotoxicity

Cytotoxicity assessments were performed after 48 h culture by measuring the secretion of lactate dehydrogenase (LDH) with a commercial kit. Briefly, cell culture supernatants were collected, reacted with the kit working solution, and absorbance was measured following 25 min of development. Cell morphology and distribution were also evaluated after 48 h of culture. Scaffolds were washed with DPBS and fixed with 10% buffered formalin. Fixed cells were then washed twice with DPBS and permeabilized with

0.1% Triton X-100. Cell distribution was evaluated after SYBR Green staining while cell morphology was assessed by rhodamine phalloidin and DAPI staining. Confocal images were taken to evaluate both stains using a multiphoton microscope (Zeiss LSM 510Meta).

2.3.15. Endpoint Construct Analyses

Samples were collected after 48 h (cytotoxicity) or 14 days of culture (osteogenic potential) by rinsing them with DPBS and snap freezing with liquid N_2. Scaffolds were stored at 80 °C until analysis. Protein samples were extracted by sample homogenization in lysis buffer and collection of the correspondent supernatant after centrifugation.

2.3.15.1. Biochemical Analyses

hBMSC protein expression was evaluated by means of specific multiplex immunoassay kits following manufacturer's instructions. Proteins selected for analysis included Collagen 1A1 and osteonectin (secreted protein acidic and rich in cysteine; SPARC) for both 2k and 7k PDMS$_{star}$-MA containing scaffolds, and additionally osteopontin (OPN) and bone morphogenic protein-2 (BMP-2) for exclusively 2k PDMS$_{star}$-MA containing scaffolds. Samples were properly diluted with the assay buffer and loaded into well plates containing the appropriate bead suspension. Bound analyte was then reacted with detection antibodies, followed by the addition of streptavidin-phycoerythrin. Protein concentrations were determined by the median fluorescence intensity (MFI) using a MAGPIX (Luminex) in comparison to an analyte-specific standard curve. The obtained values were normalized to the DNA content of each construct and assessed via PicoGreen assay.

2.3.15.2. Histological Analyses

Von Kossa staining was used to assess cellular calcium deposition by manufacturer's protocol. Rehydrated sections were rinsed with distilled water, after which a 5% silver nitrate solution was applied, followed by the exposure of the samples to full spectrum light for 1 h. Samples were then sequentially rinsed with distilled water, exposed to 5% sodium thiosulfate for 3 min, and rinsed with distilled water.

2.3.16. Statistics

Data is reported as the mean ± standard deviation. Data set mean values were compared in GraphPad Prism via ANOVA followed by Tukey's posthoc test where p-value < 0.05 was considered statistically significant.

2.4. Results and Discussion

2.4.1. SIPS/Salt Fabrication

Templated SIPS PDMS$_{star}$-PEG hydrogels were prepared by photocuring a DCM-based precursor solution over a fused salt template followed by sequential evaporation of the DCM solvent, template dissolution and hydration. Series of hydrogels were prepared based on different salt sizes ("small" ~180 µm, "medium" ~270 µm, and "large" ~460 µm) as well as two different M_n's of PDMS$_{star}$-MA (2k and 7k) wherein the wt/wt% ratio of PDMS$_{star}$-MA to PEG:DA was systematically increased: 0:100, 10:90, 20:80 and 30:70. In our previous report, templated SIPS PEG-DA scaffolds (i.e. no PDMS$_{star}$-MA) were similarly prepared using a combination of SIPS and a fused salt template based on these salt sizes.[182] It was determined that a macromer concentration of 30% (wt/wt) in DCM produced mechanically robust, microporous hydrogels. This is in contrast to fabrication

of conventional hydrogels from aqueous precursor solutions without a salt template, where macromer concentrations of 5–15% (wt/wt) produce robust hydrogels owing to their low porosity.[217, 225] When we previously prepared non-templated SIPS PDMS$_{star}$-PEG hydrogels, the total macromer concentration was only 10% (wt/wt) in DCM.[216] However, in the present study, when the total macromer concentration was increased to 30% (wt/wt), this resulted in extremely hazy precursor solutions, particularly as the concentration and M$_n$ of PDMS$_{star}$-MA increased. Moreover, within several minutes, the solution exhibited signs of substantial phase separation, partitioning into a clear (i.e. PDMS$_{star}$-MA-rich layer) and cloudy layer (**Figure A-2**). Thus, it was critical to increase the flow rate of the precursor solution through the fused salt template so that it could be promptly photocured. Previously, the salt template was prepared in a glass vial and the precursor solution distributed through the template by centrifuging for 10 min.[182] Instead, herein, a mold was prepared from a glass tube and a Teflon cap (containing a small hole) secured to the base. After addition of the precursor solution to the top of the salt template, it was quickly pushed through the mold with compressed air and then exposed to UV light. Using this method, templated PDMS$_{star}$-PEG hydrogels were prepared with low sol content values (<5 wt%) indicating effective photocuring (**Table A-1**).
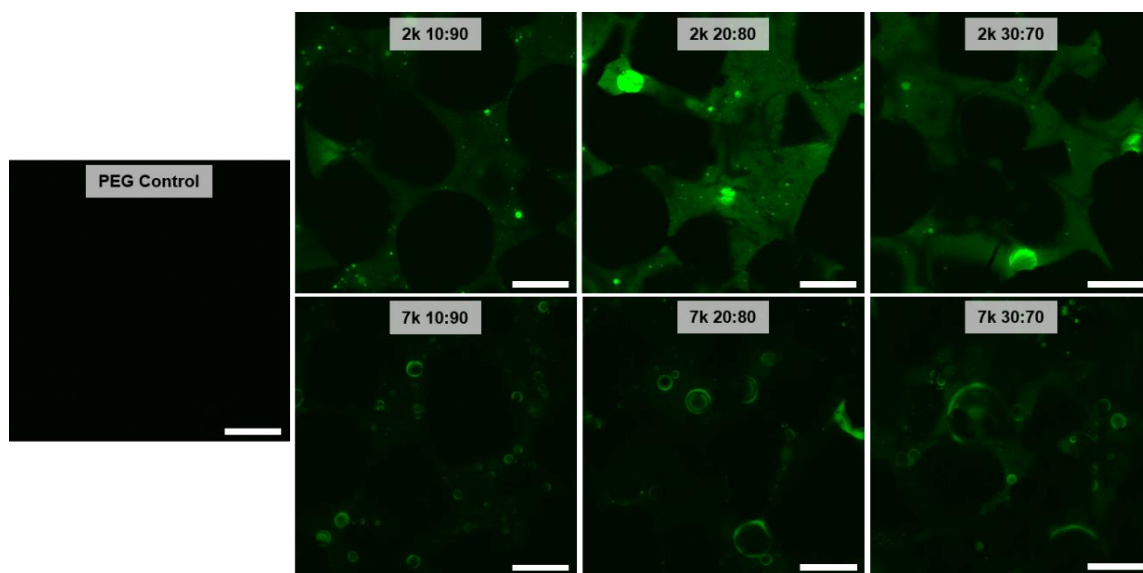
Figure 2-1. CLSM images of templated SIPS PDMS$_{star}$-PEG hydrogels prepared with increasing amounts of 2k and 7k PDMS$_{star}$-MA and a templated PEG control. All hydrogels were prepared with medium salt (270 µm). Green is assigned to PDMS$_{star}$-MA-rich regions, stained by hydrophobic dye (Nile red). Photos are adjusted +20% brightness and -20% contrast for clarity. Scale bars = 250 µm.

2.4.2. PDMS$_{star}$-MA distribution and Scaffold Morphology

Distribution of PDMS$_{star}$-MA within the templated SIPS PDMS$_{star}$-PEG hydrogels was examined by CLSM imaging with hydrophobic PDMS$_{star}$-MA-rich regions stained by hydrophobic Nile red dye. For the fabrication of non-templated PDMS$_{star}$-PEG hydrogels, an aqueous precursor solution produced exclusively discrete PDMS$_{star}$-MA-rich microparticles within a PEG-DA matrix[217] whereas SIPS fabrication produced a much more uniform distribution.[216] In general, the templated SIPS PDMS$_{star}$-PEG hydrogels exhibited PDMS$_{star}$-MA distribution throughout the pore walls (**Figure 2-1**). This was attributed to the improved solubility of PDMS$_{star}$-MA in DCM versus in water, even at higher precursor solution concentrations. Since solution phase separation increased with

43

PDMS$_{star}$-MA M$_n$, it was expected that the 2k hydrogel series would exhibit a more uniform distribution of PDMS$_{star}$-MA versus the 7k series. Indeed, the 7k series showed the presence of PDMS$_{star}$-MA-rich microdroplets that was not observed for the 2k series. SEM was used to visually confirm pore interconnectivity of templated SIPS PDMS$_{star}$-PEG hydrogels prepared with the different template salt sizes (**Figure 2-2**). While expected differences in pore sizes were apparent depending on template salt size, the measured average pore size was reduced due to specimen shrinkage associated with vacuum drying (**Table 2-1**). However, SEM images did reveal pore interconnectivity, a product of the fused salt template. Pore size for hydrated hydrogels was measured using brightfield microscopy (**Figure 2-2**). As anticipated, hydrated pore sizes were swollen beyond the original salt size of the template (**Table 2-1**). To quantify interconnectivity of hydrated specimens, a water wicking test was adapted from Bencherif et al.[223] Templated SIPS PDMS$_{star}$-PEG hydrogels (20:80 wt/wt% and 2k PDMS$_{star}$-MA) were compared to the analogous non-templated SIPS hydrogels as well as conventionally fabricated hydrogels (i.e. from an aqueous precursor solution) (**Figure 2-3A**).[216, 217] For the templated hydrogel only, due to its high pore interconnectivity, water was quickly wicked away using a Kimwipe and pore interconnectivity was > 50% (**Figure A-3**). In contrast, conventionally and SIPS fabricated, non-templated PDMS$_{star}$-PEG hydrogels demonstrated interconnectivity below 15%.

44
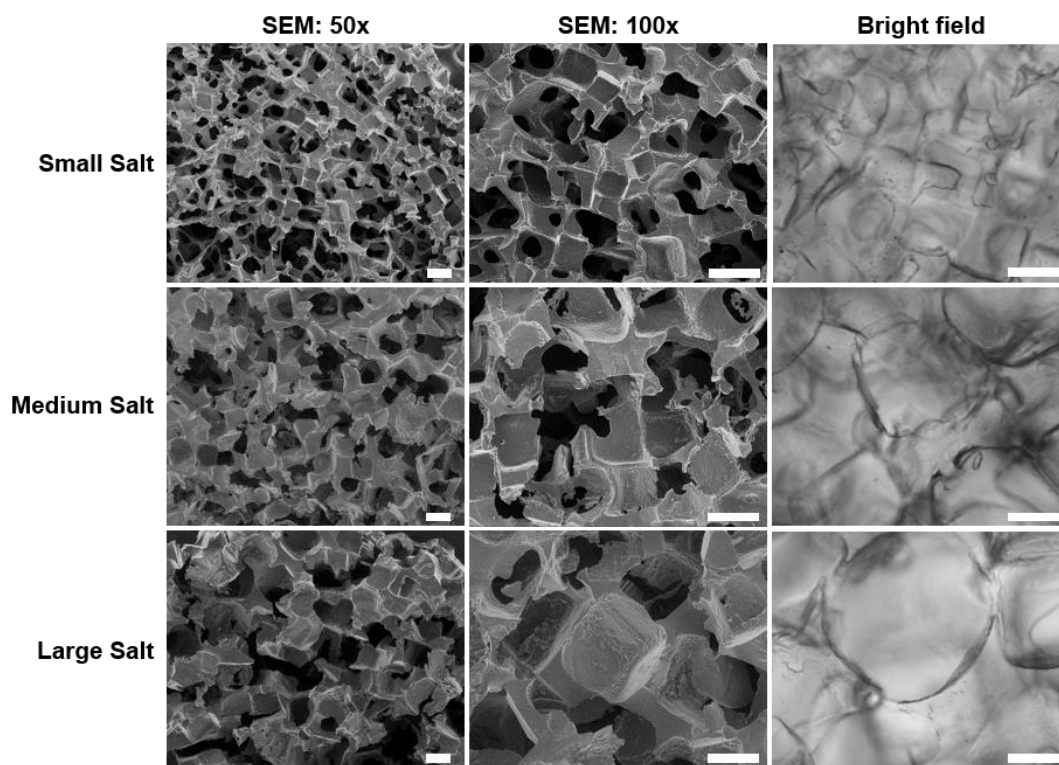
Figure 2-2. SEM images of templated SIPS PDMS$_{star}$-PEG hydrogels fabricated with each salt size [20:80 wt/wt% and 2k PDMS$_{star}$-MA] (left and middle column). Representative brightfield images were taken during confocal imaging (right column). Scale bars = 200 µm.

Table 2-1. Pore size measurements of templated SIPS PDMS$_{star}$-PEG hydrogels fabricated with each template salt size [20:80 wt/wt% and 2k PDMS$_{star}$-MA] determined by ImageJ software using SEM images (acquired at 100x magnification) for "dry" measurements [i.e. after vacuum drying] and brightfield microscopy images for "hydrated" measurements [i.e. in the hydrated state].

	Small Salt	**Medium Salt**	**Large Salt**
Salt size:	181 ± 29 µm	268 ± 35 µm	459 ± 69 µm
Dry:	124 ± 17 µm	199 ± 13 µm	282 ± 60 µm
Hydrated:	268 ± 19 µm	367 ± 16 µm	428 ± 60 µm

2.4.3. Material Characterization

To assess the impact of PDMS$_{star}$-MA concentration (0:100, 10:90, 20:80 and 30:70 wt/wt% PDMS$_{star}$-MA:PEG-DA) and M$_n$ (2k or 7k), templated SIPS PDMS$_{star}$-PEG hydrogels were prepared with the intermediate salt size (medium salt, 270 µm) and subjected to characterization of key properties – hydration, modulus and degradation rate. Because the hydration (i.e. equilibrium swelling) is known to profoundly impact most hydrogels' mechanical and degradation properties,[47, 226] this was initially measured (**Figure 2-3B**).

All hydrogels exhibited statistically similar swelling ratios (~13) compared to the analogous templated SIPS PEG-DA control. It is hypothesized that the high pore volume and resulting high water content effectively masked any contribution from pore wall hydrophobicity based on PDMS$_{star}$-MA content, M$_n$ or its distribution therein. As expected, it was noted that the high pore volume of these templated SIPS hydrogels produced a significantly higher swelling ratio versus the analogous non-templated SIPS PDMS$_{star}$-PEG hydrogels (~8).[216]

The bulk compressive modulus of these templated SIPS PDMS$_{star}$-PEG hydrogels was also assessed (**Figure A-4**). All hydrogels displayed similar moduli (~8 kPa) that were not statistically different versus the analogous PEG-DA control. This may be attributed to their similar high bulk hydration (i.e. swelling), resulting from their macroporosity. However, additional mechanical analyses were conducted that were anticipated to reveal differences among hydrogels based on the PDMS$_{star}$-MA content and M$_n$ that comprised the pore walls. An indicator of the damping or energy absorption ability of a material, tan

δ (based on the ratio of loss [G''] and storage [G'] moduli) was also measured (**Figure 2-3C**). In this case, templated SIPS hydrogels based on 2k PDMS$_{star}$-MA produced a reduction in tan δ versus the PEG-DA control whereas those based on 7k PDMS$_{star}$-MA did not. The more homogeneous distribution of 2k PDMS$_{star}$-MA within the PEG-DA matrix of the pore walls (**Figure 2-1**) is believed to give rise to this difference in damping. Thus, when the PDMS$_{star}$-MA is not uniformly distributed (i.e. for 7k), the resulting hydrogels retain more of the native properties of the PEG-DA control. Next, AFM was used to probe the local modulus values for templated SIPS PDMS$_{star}$-PEG hydrogels based on 2k PDMS$_{star}$-MA. Versus bulk analyses, AFM has been used to measure the local modulus of scaffold of the pore walls at a scale commensurate with cellular interaction.[28] Per **Figure 2-3D**, the uniform dispersion of 2k PDMS$_{star}$-MA within the templated SIPS PDMS$_{star}$-PEG hydrogels was determined to decrease the Young's modulus values versus the analogous PEG-DA control. Despite this decrease, however, modulus values (~15 kPa) within the range associated with osteogenesis.[36, 97]

The relative differences in degradation rates of templated SIPS PDMS$_{star}$-PEG hydrogels versus the analogous PEG-DA control was assessed by measuring mass loss under accelerated (basic) conditions (**Figure A-5**). Despite the introduction of hydrophobic PDMS$_{star}$-MA, no distinguishable differences in mass loss were observed, irrespective of PDMS$_{star}$-MA content, at all time points. This is attributed to their similarities in pore size (**Figure 2-2**) and bulk swelling (**Figure 2-3B**) that dominate any contributions from the hydrophobic comacromer. However, based on the known accelerated degradation of porous materials having larger pore sizes[227] and our previous

studies with templated SIPS PEG-DA scaffolds of varying pore sizes,[182] increasing and decreasing the pore size of these templated hydrogels is expected to increase and decrease degradation rates, respectively.
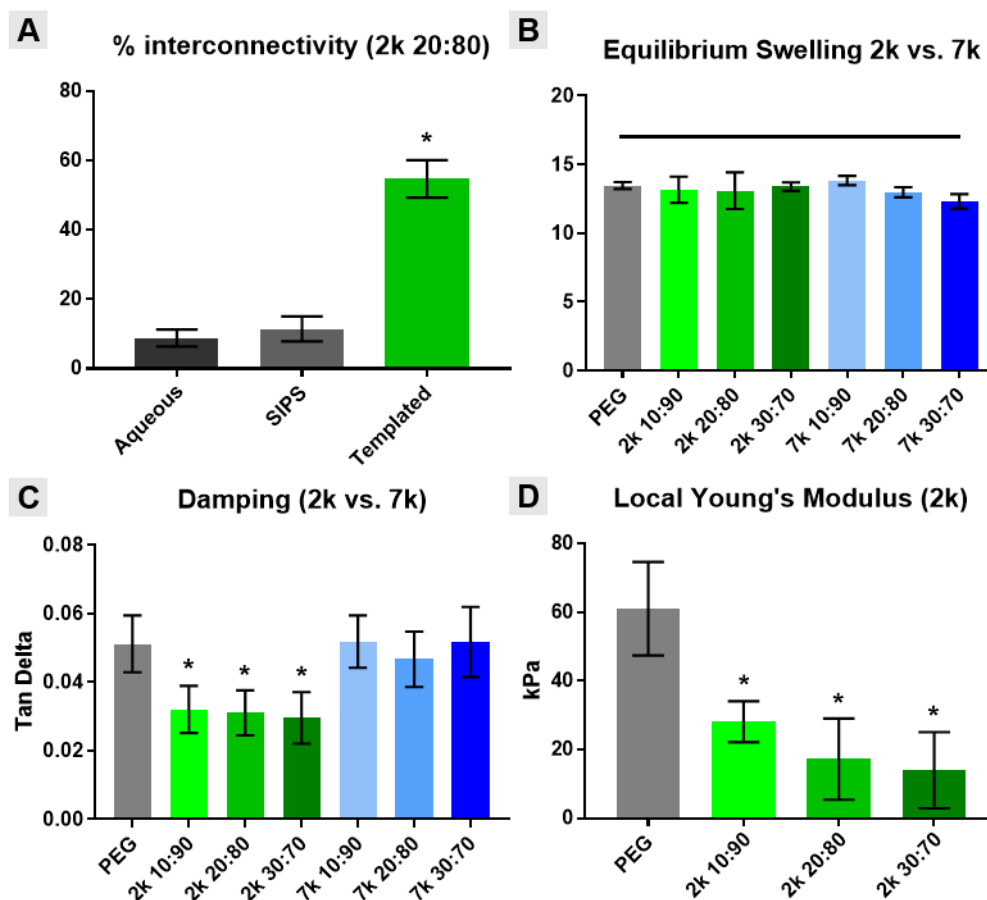
Figure 2-3. Templated SIPS PDMS$_{star}$-PEG hydrogels and analogous PEG-DA control material properties: **(A)** % interconnectivity, **(B)** equilibrium swelling, **(C)** damping and **(D)** local Young's modulus. All hydrogel scaffolds were fabricated with medium salt (~270 µm). Statistical difference versus the analogous templated SIPS PEG-DA control is represented as * = p <0.05.

2.4.4. Bioactivity

Bioactivity can be examined *in vitro* by exposing hydrogels to conditions that mimic the implant environment (i.e. ionic concentration, pH and temperature) via soaking in simulated body fluid (SBF, 1x) at 37 °C.[224] A series of templated SIPS hydrogels were prepared with 2k PDMS$_{star}$-MA of varying concentrations (0:100, 10:90, 20:80 and 30:70 wt/wt% PDMS$_{star}$-MA:PEG-DA) using the intermediate salt size (medium salt, ~270 µm). All PDMS$_{star}$-PEG hydrogels exhibited mineralization after 4 weeks of incubation while the analogous PEG-DA control showed none (**Figure 2-4**). XRD confirmed that observed mineral present was hydroxyapatite (HAp) with peaks at 31.7, 45.3, and 56.2 indicating reflections from 112, 222 and 004 crystal planes, respectively.[216, 228-230] Thus, the presence of inorganic PDMS$_{star}$-MA introduced bioactivity to the otherwise biologically inert PEG-DA hydrogel.
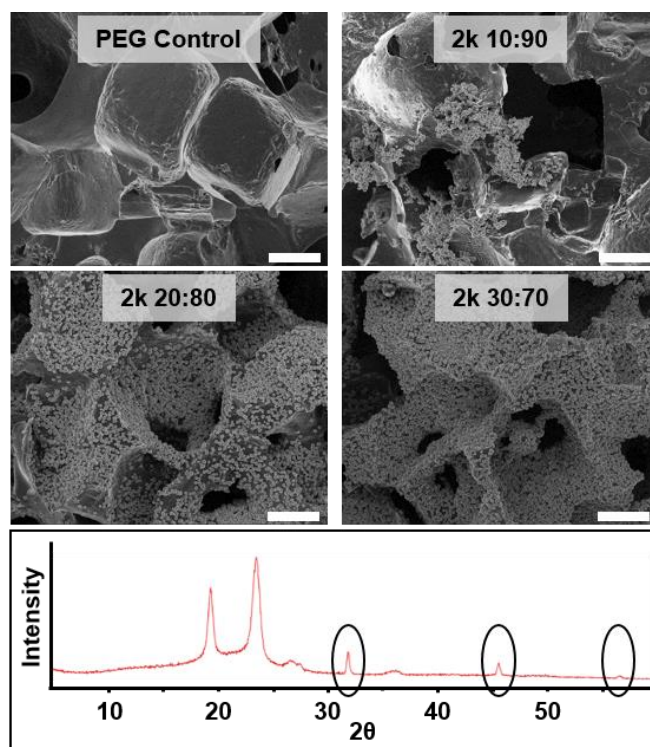
Figure 2-4. Templated SIPS PDMS$_{star}$-PEG hydrogel and analogous PEG-DA control following exposure to simulated body fluid (SBF, 1x, 37 °C, 4 weeks). Hydrogels were fabricated with medium salt (~270 µm) and 2k PDMS$_{star}$-MA. SEM images (top) displayed HAp growth on all PDMS$_{star}$-MA-containing hydrogels. XRD analysis of "20:80 wt/wt%" composition (bottom) confirmed HAp identity by characteristic peaks at 31.7, 45.5 and 56.5. Scale bar = 100 µm.

2.4.5. Cytotoxicity, Cell Seeding and Cellular Morphology

All cell-contacting templated SIPS PDMS$_{star}$-PEG scaffolds and the analogous PEG-DA control (prepared with medium salt; ~270 µm) were made with ACRL-PEG-RGDS for controlled cell adhesion and induction. Cytotoxicity was determined by LDH assay after 48 h culture with hBMSCs (**Figure 2-5**). Normalized to the corresponding templated SIPS PEG-DA control, all PDMS$_{star}$-MA-containing hydrogels (2k and 7k) were determined to be non-cytotoxic. To verify consistent cell seeding distribution, SYBR

50

green DNA staining was used to visualize cells. Further staining with DAPI and rhodamine phalloidin indicated that cells were elongated and spread along the pore walls, as expected with the presence of the cell adhesion ligand RGDS (**Figure 2-5**). Cell morphology and abundance were similar for all PDMS$_{star}$-PEG scaffold compositions compared to the PEG-DA control (**Figure 2-5**). Thus, all compositions were subsequently subjected to 14-day culture for examination of intrinsic osteoinductivity.
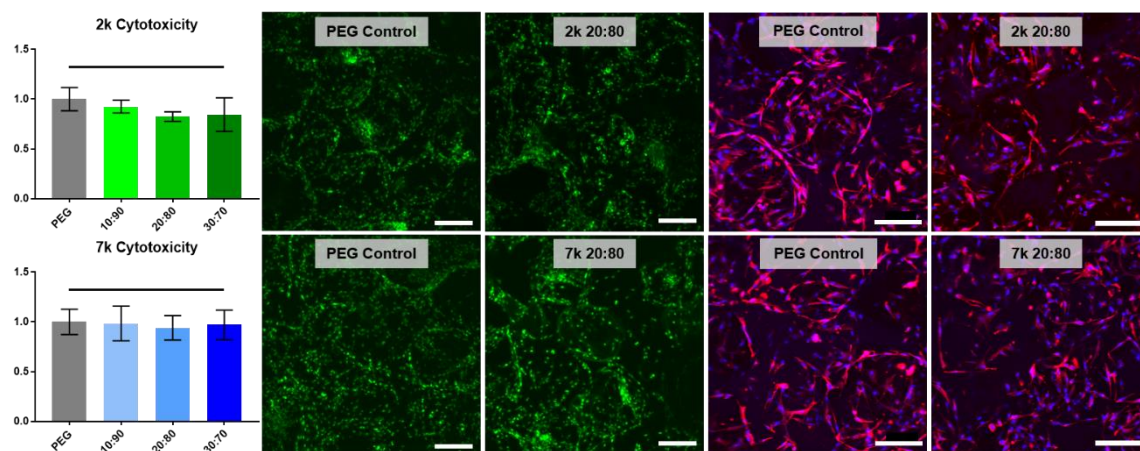
Figure 2-5. Scaffold non-cytotoxicity after 48 h culture with hBMSCs, as determined by LDH assay (left), SYBR green stain (middle) and rhodamine phalloidin (red) and DAPI (blue) stacked confocal images (right). Statistically significant difference compared to the control is represented as * = p<0.05. The complete set of images can be found in **Figure A2-6**. All templated SIPS PDMS$_{star}$-PEG and analogous PEG-DA control scaffolds were prepared with medium salt (~270 µm). Scale bars = 200 µm.

2.4.6. Scaffold-Induced Osteogenesis of hBMSCs

RGD-containing, templated SIPS PDMS$_{star}$-PEG scaffolds (prepared with medium salt; ~270 µm) were evaluated for their potential to control hBMSC fate by evaluating the

relative presence of ECM molecules relevant to osteogenesis after a 14-day culture. Protein level multiplex analysis was conducted to determine relative levels of collagen 1, the primary collagen found in bone, and osteonectin (secreted protein acidic and rich in cysteine or SPARC), a calcium-binding glycoprotein found in bone (**Figure 2-6A&B**). All templated SIPS PDMS$_{star}$-PEG scaffolds displayed evidence of PDMS$_{star}$-MA-dose dependent osteogenesis. For those based on 7k PDMS$_{star}$-MA, a 30:70 (wt/wt%) was associated with an increase in collagen 1 and SPARC relative to the analogous PEG-DA control. Scaffolds containing 2k PDMS$_{star}$-MA also displayed significant increases in collagen 1 and SPARC but at 20:80 (wt/wt%). However, when 2k PDMS$_{star}$-MA content was increased to a 30:70 (wt/wt%), collagen 1 and SPARC production fell below that of the PEG-DA control. Relative DNA levels tested verified that no significant cell death occurred for this particular scaffold (**Figure A-7**). Thus, we speculate that the more uniform dispersion of 2k PDMS$_{star}$-MA at this high concentration (30:70 wt/wt%) may have impacted scaffold surface hydrophobicity, resulting in protein adhesion inhibiting function of RGD receptors.
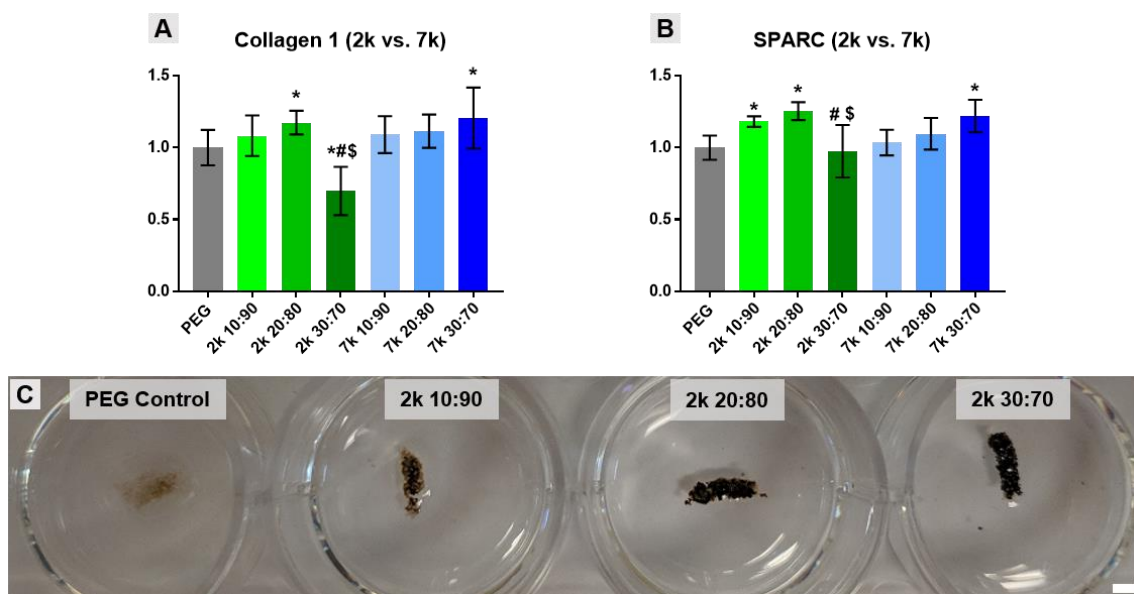
Figure 2-6. Protein-level multiplex immunoassay results for **(A)** Collagen 1 and **(B)** SPARC presence after 14-day culture on templated SIPS PDMS$_{star}$-PEG and analogous PEG-DA control scaffolds were prepared with medium salt (~270 µm). **(C)** Von Kossa staining (brown-black color) for mineralization after 14-day culture with hBMSCs on scaffolds prepared with 2k PDMS$_{star}$-MA. Due to the intensity of staining, only macro-images could be taken due to over-saturation during imaging. Statistically significant difference compared to the control is represented as * = $p < 0.05$, to the corresponding 10:90 (wt/wt%) as # = $p < 0.05$, and to the corresponding 20:80 as \$ = $p < 0.05$. Scale bar = 2 mm.

Given the enhanced osteogenesis observed with templated SIPS PDMS$_{star}$-PEG scaffolds based on 2k PDMS$_{star}$-MA at 20:80 (wt/wt%), further studies were conducted for the 2k scaffold series. Specifically, levels of osteopontin (OPN), a bone ECM protein involved in biomineralization, and bone morphogenic protein-2 (BMP-2), a potent osteogenic growth factor, were analyzed by immunoassay. Although no statistical differences were observed for BMP-2 expression levels, the 20:80 (wt/wt%) scaffold supported a 1.5-fold increase in OPN levels relative to the PEG-DA control (**Figure A-8**). However, when 2k PDMS$_{star}$-MA levels were further increased to 30:70 (wt/wt%), OPN

levels were reduced below that of the 10:90 and 20:80 (wt/wt%) formulations as seen previously with collagen 1 and SPARC (**Figure 2-6A&B**). Von Kossa staining was used as a visual indicator of matrix mineralization and also revealed considerable enhancement in calcium deposition with increasing 2k PDMS$_{star}$-MA content (represented by a brown-black color)(**Figure 6C**). Despite the reductions in collagen 1, SPARC, and BMP-2 noted for the 30:70 (wt/wt%) scaffold, this formulation appeared to support increased mineralization relative to remaining formulations, denoting a possible disconnect between bioactivity and osteoinductivity of the scaffold based on distribution of the PDMS$_{star}$-MA.

2.5. Conclusions

Herein, we describe the preparation of templated SIPS PDMS$_{star}$-PEG hydrogels and their utility as instructive scaffolds (absent of exogenous growth factors) for bone regeneration. These hydrogels utilized an inorganic hydrophobic comacromer, PDMS$_{star}$-MA, to introduce bioactivity and osteoinductivity. Fabrication with a fused salt template, in Conjunction with SIPS employing a DCM precursor solution (followed by drying and hydration), created interconnected macropores of tunable sizes to permit post-fabrication cell seeding and for osteoconductivity. Hydrogels were produced with two M_n's of PDMS$_{star}$-MA (2k and 7k) and varying wt/wt% ratios (0:100, 10:90, 20:80, and 30:70) of PDMS$_{star}$-MA to PEG-DA (M_n = 3.4k). CLSM images revealed the improved distribution of the 2k PDMS$_{star}$-MA within the PEG matrix, attributed to its superior solubility in the DCM precursor solution. Pore size tunability and interconnectivity for osteoconductivity were confirmed by SEM imaging and a water wicking test. Templated SIPS PDMS$_{star}$-PEG hydrogels all had similarly high bulk hydration, resulting in similar bulk Young's

moduli. However, for the 2k-containing scaffolds, a lower modulus was seen at a local level (via AFM probe measurement), but they remained in the range associated with osteogenesis in hydrogels. While absent for the PEG-DA control, bioactivity was confirmed for templated SIPS PDMS$_{star}$-PEG hydrogels (2k series) with HAp formation observed (via SEM and XRD) following soaking in SBF. Under accelerated conditions, owing to their similarity in pore size and bulk swelling, these hydrogels exhibited temporal mass loss similar to that of the PEG-DA control. Finally, all RGD-containing templated SIPS PDMS$_{star}$-PEG scaffolds were confirmed non-cytotoxic and showed PDMS dose-dependent increases in key indicators of osteogenesis. However, this was dependent on comacromer M_n, wherein the better dispersed comacromer (lower M_n) showed statistical differences at lower concentrations. Von Kossa staining was used to reveal dose-dependent increases in calcium deposition by hBMSCs seeded on 2k-containing scaffolds. Overall, these templated SIPS PDMS$_{star}$-PEG hydrogels displayed the potential to serve as instructive scaffolds for bone regeneration without the inclusion of added growth factors. The achievement of the observed bioactivity and osteoinductivity without the inclusion of glass or glass-ceramic fillers but rather a polymeric component (i.e. PDMS$_{star}$-MA) is notable.

CHAPTER III

ENHANCED OSTEOGENIC POTENTIAL OF PHOSPHONATED-SILOXANE

HYDROGEL SCAFFOLDS

3.1. Overview

In a materials-guided approach, instructive scaffolds that leverage potent chemistries may efficiently promote bone regeneration. A siloxane macromer has been previously shown to impart osteoinductivity and bioactivity when included in poly(ethylene glycol) diacrylate (PEG-DA) hydrogel scaffolds. Herein, phosphonated-siloxane macromers were evaluated for enhancing the osteogenic potential of siloxane-containing PEG-DA scaffolds. Two macromers were prepared with different phosphonate pendant group concentrations, poly(diethyl(2-(propylthio)ethyl) phosphonate methylsiloxane) diacrylate (PPMS-DA) and 25%-phosphonated analogue (PPMS-DA 25%). Macroporous, templated scaffolds were prepared by crosslinking these macromers with PEG-DA at varying mol% (15:85, 30:70 and 45:55 PPMS-DA to PEG-DA; 30:70 PPMS-DA 25% to PEG-DA). Other scaffolds were also prepared by combining PEG-DA with PDMS-MA (i.e. no phosphonate) or with vinyl phosphonate (VP) (i.e. no siloxane). Scaffold material properties were thoroughly assessed, including pore morphology, hydrophobicity, swelling, modulus, and bioactivity. Scaffolds were cultured with hBMSCs (normal media) and calcium deposition and protein expression assessed at 14 and 28 days.

3.2. Introduction

Bone regeneration using a materials-guided strategy[231] relies exclusively on the scaffold's physical and chemical properties, including morphology,[30-34] modulus,[35-39] chemical functionality,[40, 42, 43, 232] and hydrophobicity.[44-46, 233] Such instructive scaffolds eliminate the use of exogenous growth factors which are costly and risk off-target responses.[68, 234, 235] Scaffolds that combine several of these properties, especially in a decoupled fashion, represent a particularly potent approach to regeneration. Functional bone regenerative scaffolds require osteoconductivity (i.e. ability to encourage and support new bone formation), osteoinductivity (i.e. ability to induce differentiation to an osteoblast-like lineage), and osseointegration (i.e. ability to integrate with native tissue).[69, 236] Inorganics, including silicon- and calcium phosphate-containing materials, have been shown to be particularly osteoinductive and osteoconductive.[66, 71] Most commonly used are ceramics [e.g. bioglass, hydroxyapatite (HAp), and β-tricalcium phosphate (β-TCP)], which are known to induce a thin surface layer of carbonated HAp (i.e. bioactivity).[67] However, their low toughness and variable resorption rates limit their utility in bone regeneration.[74, 101]

Previously, we demonstrated that an inorganic silicon-based polymer, polydimethylsiloxane (PDMS), can be utilized to impart osteoinductivity to poly(ethylene glycol) (PEG) scaffolds.[88] In contrast to ceramic fillers, the low glass transition (T_g, -120 ºC) of PDMS does not render brittleness to scaffolds. Recently, macroporous scaffolds with interconnected pores were produced by the UV cure of precursor solutions comprising PEG-diacrylate (PEG-DA) and star PDMS methacrylate (PDMS$_{star}$-MA) over

fused salt templates.[89] The use of an organic solvent to form the precursor solutions improved PDMS solubility and distribution within the resulting PDMS$_{star}$-MA/PEG-DA scaffolds which were subsequently dried and hydrated with water. These scaffolds induced osteoblast-like differentiation of human bone marrow-derived mesenchymal stems cells (hBMSCs) and promoted mineralization.

The osteoinductive and bioactive potency of siloxane-containing PEG-DA hydrogel scaffolds may be increased by leveraging additional chemical functionality. When incorporated into scaffolds, tethered small molecules have been shown to enhance osteogenic potential via local changes to the chemical environment that impact cellular behavior.[40, 232, 237, 238] Such small molecules showing strong indications for osteogenesis and mineralization, by a variety of mechanisms, include amines, alcohols, and phosphates/phosphonates.[232, 237-240] Specifically, phosphorus-containing groups have shown promise due to their native roles in calcium binding and mineralization in bone tissue formation.[241] Phosphonate-based chemistries have been independently explored with hydrogels, composites, ceramics and metal implants and shown to promote bone tissue regeneration.[238, 240-243]

Herein, towards enhancing osteoinductivity and bioactivity, hydrogel scaffolds were prepared by combining phosphonate-containing siloxane macromers with PEG-DA, poly(diethyl(2-(propylthio)ethyl) phosphonate methylsiloxane) diacrylate (PPMS-DA), and a 25%-phosphonated analogue (PPMS-DA 25%) (**Figure 3-1**). Diethyl vinylphosphonate was selected in lieu of phosphonic acid alcohols for diminished adhesivity and greater hydrophobicity which is considered favorable to bone

regeneration.[44, 45, 244] These novel macromers were crosslinked with PEG-DA at varying mol% (15:85, 30:70 and 45:55 PPMS-DA to PEG-DA; 30:70 PPMS-DA 25% to PEG-DA) to form templated scaffolds with our previously reported methods.[182] To discern the contribution of the siloxane versus the phosphonate pendant group, scaffolds were also prepared by combining PEG-DA with PDMS-MA (i.e. no phosphonate) at two concentrations, or with vinyl phosphonate (VP) (i.e. no siloxane). Templated scaffolds were evaluated in terms of distribution of the phosphonated-siloxane and pore morphology as well as key material properties, such as hydrophobicity, swelling, bulk and local compressive moduli, and bioactivity (i.e. HAp formation with exposure to simulated body fluid). Finally, all scaffold compositions were seeded with hBMSCs and cultured with normal media for evaluation of non-cytotoxicity (48 h) as well as calcium deposition and protein expression at 14- and 28-days.
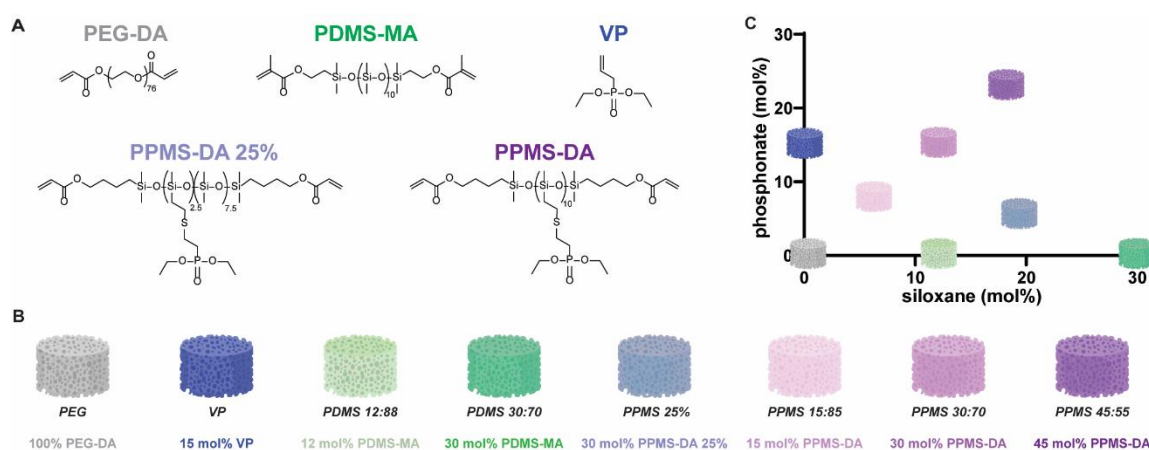
Figure 3-1. Scaffolds used to investigate the effect of phosphonated-siloxane macromers on enhancing the osteogenic potential of siloxane macromers when used to form PEG-DA-based scaffolds. **(A)** Macromers used to prepared scaffolds. **(B)** Scaffold composition

legend with mol% ratio of inorganic monomer/macromer to PEG-DA. **(C)** Graphical plot of scaffolds in terms of mol% phosphonate and siloxane.

3.3. Experimental Section

3.3.1. Materials

2,2'-Azobis(2-methylpropionitrile) (AIBN), acryloyl chloride, ammonium hydroxide, calcium chloride, deuterated chloroform ($CDCl_3$), diethyl vinyl phosphonate (VP), dipotassium hydrogen phosphate trihydrate, dithiothreitol (DTT), hexamethyldisilazane (HMDS), hydrochloric acid (HCl), magnesium chloride hexahydrate, magnesium sulfate ($MGSO_4$), Nile red, poly(ethylene glycol) 3350 (PEG-3350), potassium carbonate (K_2CO_3), potassium chloride (KCl), sodium bicarbonate ($NaHCO_3$), sodium chloride (NaCl), sodium hydroxide (NaOH), sodium sulfate, thiolacetic acid, triethylamine, trifluoromethanesulfonic acid (triflic acid), Tris-(hydroxymethyl) aminomethane (Tris), Tris-(hydroxymethyl) aminomethane (Trizma® base) and all solvents were obtained from Sigma-Aldrich. 1,3,5,7-tetravinyl-1,3,5,7-tetramethylcyclotetrasiloxane (D_4-vinyl), 1,3-bis(3-methacryloxypropyl)tetramethyldisiloxane (tetra-SiMA), 1,3-bis(4-hydroxybutyl)tetra-methyldisiloxane (HBTMDS), and octamethylcyclotetrasiloxane (D_4) were obtained from Gelest. 10% formalin solution, acetic acid, diethyl ether, ethylenediaminetetraacetic acid (EDTA), lithium chloride (LiCl), and lithium dodecyl sulfate (LiDS) were obtained from Fisher Scientific. Glutamax, penicillin (10,000 IU/mL), and streptomycin (10,000 µg/mL) were obtained from Life Technologies. Dulbecco's modified essential medium (DMEM), Dulbecco's phosphate buffered saline (DPBS), and phosphate buffered saline (No, Ca, or

Mg; PBS) were obtained from Corning. Heat-inactivated fetal bovine serum (MSC grade; FBS) and minimum essential medium-α (MEM-α) were obtained from Gibco. Acryloyl-PEG-succinimidyl valerate (ACRL-PEG-SVA) was obtained from Laysan Bio, Inc. Alizarin Red S was obtained from Acros Organics. Ethyl (2,4,6-trimethylbenzoyl) phenylphosphinate was obtained from Combi-Blocks. Peptide RGDS was obtained from Bachem. The lactate dehydrogenase (LDH) assay was obtained from Roche, the MAGPIX immunoassay was obtained from Luminex, the Luminex human magnetic assay was obtained from R&D Systems, and the Quant-iT PicoGreen dsDNA Assay was obtained from Invitrogen. Cryopreserved human bone-marrow derived mesenchymal stem cells were obtained from three different donors (Texas A&M Institute for Regenerative Medicine).
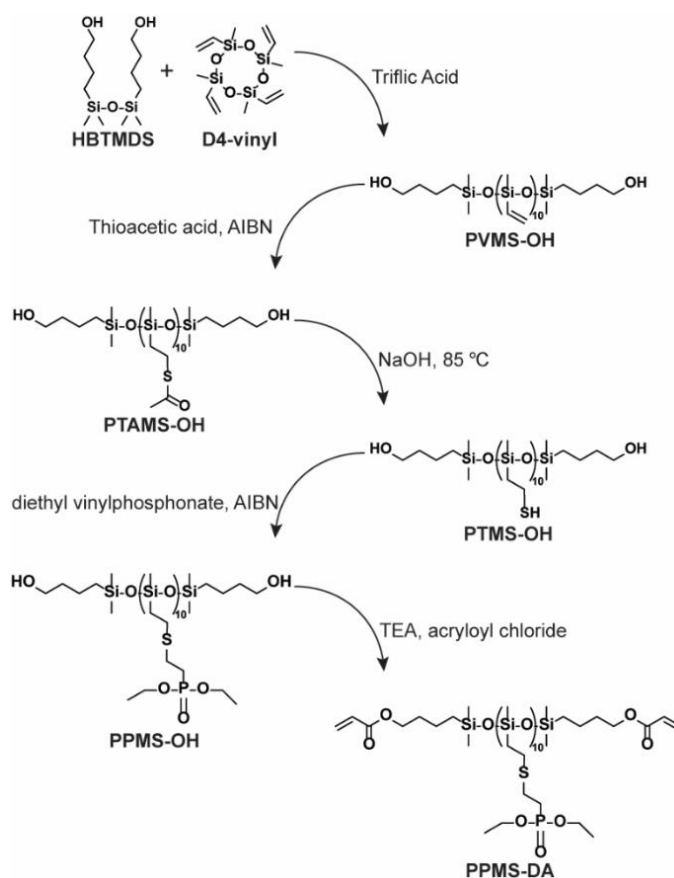
Figure 3-2. Synthesis of PPMS-DA ($n = 10$).

3.3.2. Synthesis

3.3.2.1. PPMS-DA and PPMS-DA 25% Synthesis

Synthesis of poly(diethyl(2-(propylthio)ethyl) phosphonate methylsiloxane) diacrylate (PPMS-DA) ($M_n = 3231$ g/mol, $n = 10$) (**Figure 3-2**) and a 25% phosphonated version (PPMS-DA 25%) ($M_n = 1653$ g/mol, $n = 2.5$ and $m = 7.5$) (**Figure A-9**) were each carried out via five synthetic steps. All reactions contained a Teflon-covered stir bar to agitate the reaction mixture and each product was vacuum-dried overnight (14.7 psi) at room temperature (RT) prior to the following reaction. First, PVMS-OH or PVMS-OH

25% were prepared by the acid catalyzed equilibration of 1,3,5,7-tetravinyl-1,3,5,7-tetramethylcyclotetra-siloxane (PPMS-DA: 15 g, 43.5 mmol; PPMS-DA 25%: 7.5 g, 21.8 mmol) with 1,3-bis(4-hydroxybutyl)tetramethyldisiloxane (PPMS-DA: 4.85 g, 17.4 mmol; PPMS-DA 25%: 9.7 g, 34.8 mmol) in a 100 mL round bottom (rb) flask equipped with a rubber septum and triflic acid (PPMS-DA: 60 µL, 0.678 mmol; PPMS-DA 25%: 120 µL, 1.36 mmol) added via micropipette. D_4 (19.37 g, 65.2 mmol) was added to this reaction to lower the frequency of reactive vinyl side groups of PVMS-OH 25% while maintaining the same repeat units as PVMS-OH. The mixture was allowed to stir 12 h at 75 °C then HMDS (PPMS-DA: 194 µL, 0.930 mmol; PPMS-DA 25%: 388 µL, 1.86 mmol) was added to neutralize the mixture. Each polymer mixture was precipitated in a 1:1 methanol (MeOH) to deionized water (DI) solution to isolate the PVMS-OH or PVMS-OH 25%. Next, PTAMS-OH or PTAMS-OH 25% was prepared via thiolene click chemistry by combining thioacetic acid (PPMS-DA: 12.05 mL, 171.0 mmol; PPMS-DA 25%: 10.08 mL, 143.0 mmol) with PVMS-OH or PVMS-OH 25% (PPMS-DA: 13 g, 11.40 mmol; PPMS-DA 25%: 10 g, 9.53 mmol) and AIBN (PPMS-DA: 0.374 g; 2.28 mmol; PPMS-DA 25%: 0.314 g, 1.91 mmol) in a 50 mL rb flask equipped with a rubber septum under UV light (2 mW/cm^2, 365 nm). The mixture was allowed to react overnight at RT and precipitated in 1:1 MeOH:DI as in the previous step. Third, PTMS-OH or PTMS-OH 25% was prepared via deprotection of PTAMS-OH or PTAMS-OH 25% (PPMS-DA: 15 g, 7.89 mmol; PPMS-DA 25%: 7.5 g, 6.05 mmol) in ethanol (PPMS-DA: 85 mL; PPMS-DA 25%: 42.5 mL) under basic conditions with 2M NaOH (PPMS-DA: 21 mL; PPMS-DA 25%: 2.6 mL) at 85 °C in a rb flask equipped with a reflux condenser for

2 h. 2M HCl (PPMS-DA: 100 mL; PPMS-DA 25%: 12.5 mL) was added to neutralize the reaction. PTMS-OH or PTMS-OH 25% was then isolated in a 1000 mL separatory funnel with diethyl ether (200 mL) and washed with water (2 x 100 mL) and brine (1 x 100 mL), each time removing the aqueous layer to isolate the product. In the fourth step, PPMS-OH or PPMS-OH 25% was prepared via thiolene click chemistry by combining diethyl vinylphosphonate (PPMS-DA: 18.45 g, 112.4 mmol; PPMS-DA 25%: 4.5 g, 27.56 mmol) and AIBN (PPMS-DA: 0.20 g, 1.22 mmol; PPMS-DA 25%: 0.145 g, 0.882 mmol) with PTMS-OH or PTMS-OH 25% (PPMS-DA: 9.0 g, 6.08 mmol; PPMS-DA 25%: 5 g, 4.41 mmol) in a 50 mL rb flask equipped with a rubber septum under UV light (2 mW/cm^2, 365 nm). The final product was precipitated as done previously in 1:1 MeOH:DI. In the final step, PPMS-OH or PPMS-OH 25% (PPMS-DA: 7 g, 2.26 mmol; PPMS-DA 25%: 4.0 g, 2.59 mmol) was dissolved in DCM (PPMS-DA: 35 mL; PPMS-DA 25%: 20 mL) in a rb flask equipped with a rubber septum and subsequently purged with nitrogen (N_2). Triethylamine (PPMS-DA: 0.629 mL, 4.51 mmol; PPMS-DA 25%: 0.721 mL, 5.18 mmol) and acryloyl chloride (PPMS-DA: 0.729 mL, 9.03 mmol; PPMS-DA 25%: 0.836 mL, 10.36 mmol) were sequentially added dropwise via syringe for diacrylation of PPMS-OH or PPMS-OH 25% to form PPMS-DA or PPMS-DA 25%, respectively. The reaction mixture was allowed to stir at RT overnight. PPMS-DA or PPMS-DA 25% was then sequentially dissolved in DCM (100 mL), precipitated in 2M K_2CO_3 (10 mL), and washed with water (10 mL) in a 250 mL separatory funnel. The organic layer was removed and precipitated in a 1:1 MeOH:DI solution to isolate PPMS-DA or PPMS-DA 25% as a

colorless liquid. Yield, glass transition temperature (T_g), and ^1H NMR for each reaction product are as follows.

PVMS-OH ($n = 10$). Yield: 75.2%. T_g: -124 ℃. ^1H NMR (δ, ppm): 0.08 (12H, Si*CH₃*), 0.14 (30H, *CH₃*SiCHCH₂), 0.56 (4H, Si*CH₂*CH₂CH₂CH₂OH), 1.40 (4H, SiCH₂*CH₂*CH₂CH₂OH), 1.57 (4H, SiCH₂CH₂*CH₂*CH₂OH), 3.64 (4H, SiCH₂CH₂CH₂*CH₂*OH), 5.79 (10H, CH₃Si*CH*CH₂), 5.96 (20H, CH₃SiCH*CH₂*).

PTAMS-OH ($n = 10$). Yield: 80.0%. T_g: -73 ℃. ^1H NMR (δ, ppm): 0.10 (12H, Si*CH₃*), 0.18 (30H, *CH₃*SiCHCH₂), 0.56 (4H, Si*CH₂*CH₂CH₂CH₂OH), 0.91 (20H, CH3Si*CH₂*CH₂), 1.42 (4H, SiCH₂*CH₂*CH₂CH₂OH), 1.59 (4H, SiCH₂CH₂*CH₂*CH₂OH), 2.3 (30H, SC(O)*CH₃*), 2.9 (20H, CH₃SiCH₂*CH₂*) 3.64 (4H, SiCH₂CH₂CH₂*CH₂*OH).

PTMS-OH ($n = 10$). Yield: 82.5%. T_g: -82 ℃. ^1H NMR (δ, ppm): 0.10 (12H, Si*CH₃*), 0.15 (30H, *CH₃*SiCHCH₂S), 0.58 (4H, Si*CH₂*CH₂CH₂CH₂OH), 1.00 (20H, CH₃Si*CH₂*CH₂S), 1.41 (4H, SiCH₂*CH₂*CH₂CH₂OH), 1.56 (4H, SiCH₂CH₂*CH₂*CH₂OH), 2.62 (20H, CH₃SiCH₂*CH₂*S), 3.66 (4H, SiCH₂CH₂CH₂*CH₂*OH).

PPMS-OH ($n = 10$). Yield: 58.3%. T_g: -83 ℃. ^1H NMR (δ, ppm): 0.09 (12H, Si*CH₃*), 0.14 (30H, *CH₃*SiCHCH₂S), 0.58 (4H, Si*CH₂*CH₂CH₂CH₂OH), 0.94 (20H, CH₃Si*CH₂*CH₂S), 1.33 (60H, SCH₂CH₂P(O)CH₂*CH₃*), 1.40 (4H, SiCH₂*CH₂*CH₂CH₂OH), 1.54 (4H, SiCH₂CH₂*CH₂*CH₂OH), 2.03 (20H, SCH₂*CH₂*P(O)OCH₂CH₃), 2.60 (20H, CH₃SiCH₂*CH₂*S), 2.73 (20H, S*CH₂*CH₂P(O)CH₂CH₃), 3.64 (4H, SiCH₂CH₂CH₂*CH₂*OH), 4.1 (40H, SCH₂CH₂P(O)O*CH₂*CH₃).

PPMS-DA ($n = 10$). Yield: 98.5%. T_g: -62 ℃. ^1H NMR (δ, ppm): 0.09 (12H, Si*CH₃*), 0.14 (30H, *CH₃*SiCHCH₂S), 0.58 (4H, Si*CH₂*CH₂CH₂CH₂O(O)CHCH₂), 0.89 (20H,

CH₃SiCH₂CH₂S), 1.33 (60H, SCH₂CH₂P(O)CH₂CH₃), 1.40 (4H, SiCH₂CH₂CH₂CH₂O(O)CHCH₂), 1.54 (4H, SiCH₂CH₂CH₂CH₂O(O)CHCH₂), 2.02 (20H, SCH₂CH₂P(O)OCH₂CH₃), 2.58 (20H, CH₃SiCH₂CH₂S), 2.74 (20H, SCH₂CH₂P(O)CH₂CH₃), 2.94 (4H, SiCH₂CH₂CH₂CH₂O(O)CHCH₂), 4.1 (40H, SCH₂CH₂P(O)OCH₂CH₃), 6.11 (2H, SiCH₂CH₂CH₂CH₂O(O)CHCH₂), 6.33 (4H, SiCH₂CH₂CH₂CH₂O(O)CHCH₂).

PVMS-OH 25% ($n = 2.5$ and $m = 7.5$). Yield: 69.2%. T_g: -121 ºC. ¹H NMR (400 MHz; δ, ppm): 0.07 (57H, Si*CH₃*), 0.14 (7.5H, *CH₃*SiCHCH₂), 0.56 (4H, Si*CH₂*CH₂CH₂CH₂OH), 1.40 (4H, SiCH₂*CH₂*CH₂CH₂OH), 1.60 (4H, SiCH₂CH₂*CH₂*CH₂OH), 3.65 (4H, SiCH₂CH₂CH₂*CH₂*OH), 5.82 (2.5H, CH₃Si*CH*CH₂), 5.96 (5H, CH₃SiCH*CH₂*).

PTAMS-OH 25% ($n = 2.5$ and $m = 7.5$). Yield: 82.6%. T_g: -100 ºC. ¹H NMR (400 MHz; δ, ppm): 0.07 (64.5H, Si*CH₃*), 0.56 (4H, Si*CH₂*CH₂CH₂CH₂OH), 0.87 (5H, CH₃Si*CH₂*CH₂S), 1.40 (4H, SiCH₂*CH₂*CH₂CH₂OH), 1.59 (4H, SiCH₂CH₂*CH₂*CH₂OH), 2.29 (7.5H, SC(O)*CH₃*), 2.92 (5H, CH₃SiCH₂*CH₂*S), 3.64 (4H, SiCH₂CH₂CH₂*CH₂*OH).

PTMS-OH 25% ($n = 2.5$ and $m = 7.5$). Yield: 64.3%. T_g: -102 ºC. ¹H NMR (400 MHz; δ, ppm): 0.07 (64.5H, Si*CH₃*), 0.57 (4H, Si*CH₂*CH₂CH₂CH₂OH), 0.98 (5H, CH₃Si*CH₂*CH₂S), 1.41 (4H, SiCH₂*CH₂*CH₂CH₂OH), 1.60 (4H, SiCH₂CH₂*CH₂*CH₂OH), 2.92 (5H, CH₃SiCH₂*CH₂*S), 3.64 (4H, SiCH₂CH₂CH₂*CH₂*OH).

PPMS-OH 25% ($n = 2.5$ and $m = 7.5$). Yield: 68.4%. T_g: -95 ºC. ¹H NMR (400 MHz; δ, ppm): 0.07 (64.5H, Si*CH₃*), 0.56 (4H, Si*CH₂*CH₂CH₂CH₂OH), 0.96 (5H, CH₃Si*CH₂*CH₂S), 1.33 (15H, SCH₂CH₂P(O)CH₂*CH₃*), 1.40 (4H, SiCH₂*CH₂*CH₂CH₂OH),

1.58 (4H, SiCH$_2$CH$_2$*CH$_2$*CH$_2$OH), 2.03 (5H, SCH$_2$*CH$_2$*P(O)OCH$_2$CH$_3$), 2.61 (5H, CH$_3$SiCH$_2$*CH$_2$*S), 2.73 (5H, S*CH$_2$*CH$_2$P(O)CH$_2$CH$_3$), 3.65 (4H, SiCH$_2$CH$_2$CH$_2$*CH$_2$*OH), 4.1 (10H, SCH$_2$CH$_2$P(O)O*CH$_2$*CH$_3$).

PPMS-DA 25% (n = 2.5 and m = 7.5). Yield: 38.3%. T$_g$: -94 ℃. ^{1}H NMR (400 MHz; δ, ppm): 0.07 (64.5H, Si*CH$_3$*), 0.56 (4H, Si*CH$_2$*CH$_2$CH$_2$CH$_2$O(O)*CH*CH$_2$), 0.96 (5H, CH$_3$Si*CH$_2$*CH$_2$S), 1.33 (15H, SCH$_2$CH$_2$P(O)CH$_2$*CH$_3$*), 1.40 (4H, SiCH$_2$*CH$_2$*CH$_2$CH$_2$O(O)*CH*CH$_2$), 1.58 (4H, SiCH$_2$CH$_2$*CH$_2$*CH$_2$O(O)*CH*CH$_2$), 2.03 (5H, SCH$_2$*CH$_2$*P(O)OCH$_2$CH$_3$), 2.61 (5H, CH$_3$SiCH$_2$*CH$_2$*S), 2.73 (5H, S*CH$_2$*CH$_2$P(O)CH$_2$CH$_3$), 3.65 (4H, SiCH$_2$CH$_2$CH$_2$*CH$_2$*O(O)*CH*CH$_2$), 4.1 (10H, SCH$_2$CH$_2$P(O)O*CH$_2$*CH$_3$), 6.12 (2H, SiCH$_2$CH$_2$CH$_2$CH$_2$O(O)*CH*CH$_2$), 6.36 (4H, SiCH$_2$CH$_2$CH$_2$CH$_2$O(O)CH*CH$_2$*).

3.3.2.2. PDMS-MA (n = 10) Synthesis

Linear PDMS-MA (M$_n$ = 1044 g/mol) was prepared by a modification of a prior report.[245] D$_4$ (7 g, 23.60 mmol) and tetra-SiMA (3.65 g, 9.44 mmol) underwent acid-catalyzed ring-opening polymerization by triflic acid (60 µL, 0.68 mmol) for 24 h and was subsequently quenched with HMDS (194 µL, 9.30 mmol) with stirring for 1 h. The resulting PDMS-MA was filtered and dried under reduced pressure, resulting in a colorless liquid. Yield: 68.8%. T$_g$: -117 °C. ^{1}H NMR (400 MHz; δ, ppm): 0.07 (72H, *CH$_3$*SICH$_2$CH$_2$O), 0.57 (4H, CH$_2$Si*CH$_2$*CH$_2$O), 1.94 (6H, OC(O)C(*CH$_3$*)CH$_2$), 4.1 (4H, CH$_3$SiCH$_2$*CH$_2$*O), 5.54 (2H, OC(O)C(CH$_3$)*CH$_2$*), 6.10 (2H, OC(O)C(CH$_3$)*CH$_2$*).

3.3.2.3. PEG-DA Synthesis

PEG-DA (M_n = 3.4k g/mol) was prepared as previously reported.[217] Briefly, PEG-3350 (23.5 g, 7.0 mmol) was dissolved in 120 mL of DCM and reacted with triethylamine (1.95 mL, 14.0 mmol) and acryloyl chloride (2.27 mL, 28.0 mmol). The reaction was neutralized by a 2 M K_2CO_3 wash, the organic phase dried in $MgSO_4$, and finally the PEG-DA was precipitated in ethyl ether and obtained by vacuum filtration. The resulting white powder was dried under reduced pressure (14.7 psi), and its' structure was confirmed by ^{1}H NMR in agreement with what was previously reported.

3.3.2.4. ACRL-PEG-RGDS Synthesis

ACRL-PEG-RGDS was synthesized as previously reported.[88, 89] Briefly, RGDS was reacted with acryloyl-PEG-SVA at a 1:1 molar ratio for 2 h in 50 mM sodium bicarbonate. The resulting ACRL-PEG-RGDS product was purified by dialysis and subsequently lyophilized. ACRL-PEG-RGDS was included in all hydrogels utilized for cell culture at 1 µmol/mL of precursor solution.

3.3.2.5. NMR

^{1}H-NMR spectra were obtained on an 'INOVA 500' 500 MHz or 'Ascend 400' 400 MHz spectrometer operating in the Fourier transform mode. Solutions of 5% (w/v) $CDCl_3$ were used to obtain spectra. Residual $CHCl_3$ (δ 7.26) served as an internal standard.

3.3.3. Fabrication

3.3.3.1. Precursor Solution Preparation

A total of eight scaffold compositions were prepared (**Figure 3-1**). DCM-based precursor solutions were prepared with the same total moles of macromers (coinciding to

the number of moles to prepare the **PEG** scaffold) but with varying mol% ratio of inorganic monomer or macromer to PEG-DA. A photoinitiator (ethyl (2,4,6-trimethylbenzoyl) phenylphosphinate) was added at 0.01 g/g of macromer. Solutions were vortexed 1 min after combination of each component and again prior to addition to the mold.

3.3.3.2. Templated Hydrogel Fabrication

Templated SIPS hydrogels were fabricated as previously reported.[89, 182] Salt templates were formed with sieved NaCl [ASTM E-11 specification, between No. 40 (425 µm opening) and No. 60 (250 µm opening)] at a size of 268 ± 35 µm. Molds for templating and curing were prepared by pushing one end of a borosilicate glass tube (ID: ½") covered with aluminum foil into a custom Teflon cap with a small hole in the bottom and securing with Parafilm. 3.5 g of a 5 wt% DI water and sieved salt mixture was then added to the mold and subsequently compacted using a flat-ended glass rod, covered with Parafilm, and centrifuged 5 min at 2000 rpm (Eppendorf 5810R centrifuge, A-4-62 rotor). Afterwards, the cover was removed and the template was dried at RT in a fume hood for 24 h. The precursor solution was deposited atop the dried salt template via syringe, and the aluminum foil in the mold was subsequently punctured through the small hole in the base of the Teflon cap. Compressed air was used to force the solution quickly through the salt template and the filled mold was UV-cured for 15 min via UV-transilluminator (6 mW cm^2, 365 nm). After 24 h fume hood evaporation, the cylindrical specimen was sectioned into 1.2 mm thick discs using a vibratome (Leica VT1000S; cutting speed = 1.75 mm/s; frequency = 30 Hz). Discs from the top and bottom of the cylinder were excluded from

testing. Discs were soaked in DI water for 48 h on a rocker table (100 rpm; water changes 3X daily) to leach salt and to hydrate the hydrogels. Fully hydrated disc diameters were measured after complete swelling and leaching, followed by die punching to the same size (8 or 10 mm diameter) for testing.

3.3.3.3. Non-porous hydrogel slab fabrication

Planar molds were prepared, in the absence of a salt template, similar to previously reported.[216] Briefly, 2 mm thick rectangular silicone molds (60 mm x 35 mm) were clamped between two glass slides (75 x 50 mm) with a small slit. A precursor solution was injected into the mold and exposed to UV-light (UV-transilluminator; 6 mW cm^2, 365 nm) for 3 min on each side. The slab was then removed from the mold, rinsed with DCM and allowed to evaporate the remaining DCM for 30 min at RT. The slab was then hydrated in 60 mL of DI water with 4 changes in the first hour and then 3 changes daily for 2 days to ensure removal of impurities. Finally, discs were punched from the slab with a die of the same size (6 or 8 mm diameter) and the corresponding thickness was ~3 mm.

3.3.4. Sol Content

Discs [$N = 5$, scaffold, diam. 10 mm; $N = 4$, non-porous slab, diam. 8 mm] were each dried at RT in a vacuum oven (14.7 psi, 24 h) in an open scintillation vial and weighed (W_{d1}). Specimens were then placed in a new scintillation vial with 10 mL of DCM, and set on a rocker table (100 rpm) for 48 h to leach any sol. Next, each disc was placed in a new scintillation vial and dried again at RT in the vacuum oven (14.7 psi, 24 h). The final weight was taken (W_{d2}) and the % sol content calculated as [($W_{d1} - W_{d2}$)/W_{d1}] x 100.

3.3.5. Hydration

Discs ($N = 10$; scaffold, diam. 10 mm; $N = 10$, slab, diam. 6 mm) were each placed into a scintillation vial, vacuum dried (14.7 psi, 24 h, RT), and weighed (W_d). Five hydrogels of each composition were subsequently placed into vials with 10 mL of DI water and another five were placed into vials with 10 mL of aqueous 70% isopropanol (IPA). All vials were placed onto a rocker table at 100 rpm for 36 h. Each disc was then weighed (W_s), and the equilibrium swelling ratio of each disc was calculated by $q_k = (W_s/W_d)$ with k being either 'h2o' for DI water or 'ipa' for isopropanol. The H-index was calculated by $H = (q_{ipa}/q_{h2o})$ for each pair (DI water and IPA) in each composition. The reported equilibrium swelling ratio in water was calculated as $(W_s - W_d)/W_d$.

3.3.6. Morphology

3.3.6.1. Scanning Electron Microscopy (SEM)

Scaffold discs (diam. 8 mm) were dried in a vacuum oven (14.7 psi, 24 h, RT). Dried discs were subjected to Au-sputter coating (Cressington Sputter Coater 108) and viewed with a field emission scanning electron microscope (SEM; JEOL NeoScope JCM-5000) at an accelerated electron energy of 10 keV.

3.3.6.2. Confocal Laser Scanning Microscopy (CLSM)

Discs (scaffolds and slabs, diam. 8 mm) were soaked for 24 h in a 60 mL Nile red solution,[89, 216] followed soaking in PBS with daily changes for 3 days. Discs were placed in a coverglass-bottom chamber and imaged on an Olympus FV1000 confocal microscope, equipped with a UPLSAPO 10X/0.4 objective. The confocal aperture was set to 1 Airy

unit and excitation and emission were 488 nm and 500-600 nm, respectively. Representative slices of the stacks were exported and images were pseudo-colored green.

3.3.6.3. Pore Measurement

Pore size of hydrated scaffold discs (diam. 8 mm) were measured using ImageJ software, and determined by the mean of the longest and shortest cross-sectional areas of the rectangular pores. Brightfield images (taken with Nikon Eclipse TE2000-S, 4X magnification) were used for hydrated measurement, and SEM images for dry measurement. For each composition, three images were taken of two scaffold discs with three pores measured per image ($N = 18$ pores).

3.3.7. Mechanical Properties

3.3.7.1. Compression Tests

Compressive properties of slab discs ($N = 6$, diam. 6 mm) and scaffolds ($N = 6$, diam. 10 mm) were evaluated with an Instron 5944 at RT. Samples were placed between two compression plates (50 mm D) and subjected to a constant displacement rate (0.5 mm/min). From the resulting stress-strain curves, the bulk Young's modulus, E, was determined using the linear portion (0 to 10 % strain).

3.3.7.2. Atomic Force Miscroscopy (AFM)

Local Young's modulus of scaffold discs ($N = 2$, diam. 10 mm) were measured using a Dimension ICON AFM (Bruker) with a Nanoscope V controller by similarly reported methods.[89] A modified silicon nitride probe (NovaScan, USA) having a nominal spring constant of 0.6 N/m with a 20 µm diameter bead attached to the cantilever was used. Standard detector calibration was performed on a clean mica disc to determine

deflection sensitivity. Standard thermal tuning calculated a spring constant of ~0.65 N/m. A scaffold disc was affixed to a 15 mm diameter metal AFM specimen disc (Ted Pella, Inc.) with double-sided tape. Water droplets were added to the sample surface to maintain hydration. Indentation was carried out at the pore walls using 1 Hz loading rates. The ramp size was 2 μm and the indentation force was 15 nN. Young's modulus values were calculated using Nanoscope Analysis software (Bruker) with a Hertzian fit model after baseline correction and boxcar filter. A sample Poisson's ratio of 0.5 was used. Individual force-displacement curves were taken at each sampled point of the hydrogel, with 4 total points from 2 hydrogel scaffolds sampled.

3.3.8. Bioactivity

Simulated body fluid (SBF) was fabricated as detailed by *Kokubo et al.*.[216, 224] Individual scaffold discs ($N = 4$; diam. 8 mm) were placed in 40 mL of SBF in 50 mL centrifuge tubes and incubated in a water bath at 37 °C. Designated discs were removed each week for 4 weeks, washed with DI water and vacuum dried (14.7 psi, 24 h). Specimens were imaged with SEM as described above. Discs from a designated time point (i.e. 1-, 2-, 3- or 4 weeks) were used exclusively for only that time point (i.e. not returned to SBF).

3.3.9. Cell Culture

Cryopreserved hBMSCs from three different donors (Texas A&M Institute for Regenerative Medicine) were thawed and expanded in Minimum Essential Medium-α (MEM-α; Gibco) supplemented with 10% MSC-qualified, heat-inactivated FBS and 1% glutamine in a 37 °C-5% CO_2 jacketed incubator. The cells were grown and harvested for

seeding into scaffolds at passage 5. Two days prior to harvesting, hBMSCs were transitioned to media containing DMEM supplemented with 10% MSC-qualified, heat-inactivated FBS and 1% antibiotic solution (10,000 IU/mL penicillin, 10,000 µg/mL streptomycin).

3.3.10. Seeding and Culture of Scaffolds

Scaffolds (diam. 8 mm) were placed in 24-well plates, dried for 48 h under ambient conditions, and further dried under vacuum for 12 h. The scaffolds were then sterilized using ethylene oxide for 12 h. Following sterilization, the scaffolds were hydrated using DPBS and washed 3 additional times with DPBS. To seed the scaffolds, hBMSC cell suspension, pooled from three donors at a total concentration of 3.5 $\times 10^6$ cells/mL, was pipetted three times on each side of the scaffolds to promote homogenous seeding. The scaffolds were cultured in non-tissue culture treated 24-well plates in DMEM + 10% MSC-qualified, heat-inactivated FBS and 1% antibiotic solution at 37 °C in a 5% CO_2 jacketed incubator. After 24 h, the scaffolds were moved to a new non-tissue culture treated 24 well-plates with fresh media to remove any non-adherent cells. Cells designated for long-term culture had culture media exchanged every 2 days from the start of seeding through the duration of culture. Osteogenic supplements were not utilized as to assess the intrinsic osteoinductivity of the scaffolds.

3.3.11. Non-cytotoxicity

Following 48 h of culture, the non-cytotoxicity of scaffolds ($N = 4$, diam. 8 mm) was assessed by measuring the secretion of LDH using a commercial kit. Briefly, cell culture supernatants were collected and reacted with the kit working solution for 25 min.

Following the reaction, the stop solution was added and absorbance was measured at 490 nm (Biotek Synergy HTX multi-mode reader). The non-cytotoxicity of the scaffolds was presented relative to the non-cytotoxic **PEG** scaffold ($N = 4$, diam. 8 mm).

3.3.12. Cell Morphology and Distribution

Following 48 h of culture, scaffolds ($N = 4$, diam. 8 mm) were washed with DPBS and fixed with 10% formalin solution. Thereafter, the scaffolds were washed twice with DPBS and the fixed cells were permeabilized with 0.1% Triton X-100. Cell morphology and distribution within the scaffolds were assessed through staining with DAPI and rhodamine phalloidin. Confocal images were taken to evaluate staining using a Leica TCS SP8 STED microscope.

3.3.13. MAGPIX Immunoassay Multiplexing

Following 14 and 28 days of culture, scaffolds ($N = 5$, diam. 8 mm) were harvested, rinsed with DPBS for 5 min, flash frozen using liquid N_2 and stored at -80 ℃ in 1.7 mL microcentrifuge tubes. Protein was extracted from each of the scaffolds using a modified version of a previously described extraction protocol.[246, 247] Briefly, 250 µL of lysis buffer (100 mM Trizma® base, 500 mM LiCl, 10 mM EDTA, 1% LiDS, 5 mM dithiothreitol, pH~7.8) was added to each scaffold-containing tube. The samples were then homogenized using plastic, RNase-free pestles (VWR) and frozen at -80 ℃ for 20 min. Following, an additional 50 µL of lysis buffer was added to the samples and they were further homogenized using the plastic pestles. Homogenized samples were then mixed using a vortex for 20 min at 4 ℃, and centrifuged at 16,000 x g for 20 min at 4 ℃ to pellet the scaffold particulates. The supernatant (homogenate) was collected for protein analysis.

Total DNA content was quantified using Quant-iT™ PicoGreen dsDNA Assay (Invitrogen) according to manufacturer's protocol. DNA levels were utilized to normalize protein levels on a per cell basis. Selected bone extracellular matrix proteins and growth factors produced by hBMSCs were quantitatively assessed using MAGPIX immunoassay multiplexing (Luminex). Sample homogenates were reacted using a Luminex human magnetic assays (R&D Systems) containing bone morphogenetic protein-2 (BMP-2), secreted protein acidic and rich in cysteine (SPARC) and collagen type 1 α1 (COL1A1) according to the manufacturer's protocol. Concentrations of proteins of interest were obtained from measured median fluorescence intensities and associated standard curves. Results were normalized to total DNA content measured from each sample.

3.3.14. Calcium Deposition

Following 14 and 28 days of culture, calcium deposition was assessed using Alizarin Red S staining and quantified spectrophotometrically using a technique adapted from Gregory et al.[248] Scaffolds ($N = 4$, diam. 8 mm) were washed twice with DPBS (containing no magnesium or calcium) and fixed with 10% formalin for 10 min. Following, the samples were washed twice with DPBS (containing no magnesium or calcium) and stained for 5 min with a 2% Alizarin Red S (w/v) solution adjusted to a pH of 4.2. The scaffolds were then washed 5 times with distilled, DI water for 1 min per wash. To quantify the stain, the samples were placed in 800 µL 10% acetic acid solution for 30 min, heated at 85 ºC for 10 min and placed on ice for 5 min. Thereafter, the samples were centrifuged at 16,000 x g for 15 min, and 500 µL of the supernatant was collected and added to a 1.7 mL microcentrifuge tube. To neutralize the acid, 200 µL of 10% ammonium

hydroxide solution was added. For each sample, 150 μL of the neutralized supernatant was added to a 96-well plate in triplicates and the absorbance was read at 405 nm (Biotek Synergy HTX multi-mode reader). The obtained values for each sample were normalized to the scaffold weight.

3.3.15. Statistics

Material characterization data is reported as the mean ± standard deviation. Data set mean values were compared in GraphPad Prism via one-way ANOVA followed by Tukey's post hoc test. *In vitro* data is reported as the mean ± standard error of mean. These statistical analyses were performed using SPSS software (Version 24.0). Homogeneity of variance was confirmed using Levene's test. Experimental means were compared using a one-way ANOVA followed by a Tukey HSD or Games-Howell (in cases where Levene's tested returned a significant result) post hoc test, as appropriate, to compare means from the experimental groups. A *p* value < 0.05 was considered statistically significant for all data herein.

3.4. Results and Discussion

3.4.1. PPMS-DA and PPMS-DA 25% Synthesis

The synthesis of a siloxane macromer bearing pendant phosphonate groups, PPMS-DA ($n = 10$), was successfully accomplished via a robust dual thiolene click chemistry strategy (**Figure 3-2**). The PPMS-DA macromer was prepared with a degree of polymerization (*n*) of 10, producing an M_n similar to that of the PEG-DA (3.4k g/mol) co-macromer used to form scaffolds. The PPMS-DA 25% ($n = 10$) macromer, containing just 25% phosphonate pendant groups, was similarly prepared to provide a reduced

phosphonate to siloxane content (**Figure A-9**). The degree of polymerization was also maintained for the PDMS-MA ($n = 10$) in order to affect a similar crosslink density.

3.4.2. Fabrication

Eight scaffold compositions were prepared to systematically evaluate the potential of phosphonated-siloxane macromers (i.e. PPMS-DA and PPMS-DA 25%) to enhance the osteogenic potential of siloxane macromers used to form PEG-DA-based scaffolds (**Figure 3-1**). The total moles of macromer in the precursor solution was maintained for all composition while the mol% ratio of inorganic component to PEG-DA was varied. A series of 3 scaffolds were fabricated with an increasing mol% ratios of PPMS-DA ($n = 10$) to PEG-DA: 15:85 (***PPMS 15:85***), 30:70 (***PPMS 30:70***), and 45:55 (***PPMS 45:55***). Another scaffold composition (***PPMS 25%***) was prepared with PPMS-DA 25% at a 30:70 mol% ratio of PPMS-DA 25% to PEG-DA. Several scaffold compositions were prepared as controls, including: a ***PEG*** scaffold (i.e. no siloxane, no phosphonate), a vinyl phosphonate (**VP**) scaffold (i.e. no siloxane) and two PDMS-MA-based scaffolds (i.e. no phosphonate), ***PDMS 12:88*** and ***PDMS 30:70***. For the ***VP*** and ***PDMS 12:88*** scaffolds, the mol% ratios of diethyl vinyl phosphonate:PEG-DA (15:85) and PDMS-MA:PEG-DA (12:88) were maintained to parallel total moles of phosphonate and siloxane, respectively, in the ***PPMS 30:70*** scaffold. The ***PDMS 30:70*** scaffold was also prepared with a 30:70 mol% ratio of PDMS-MA:PEG-DA, coinciding to the mol% ratio of the ***PPMS 30:70*** and ***PDMS 25%*** scaffolds. Linear PDMS-MA ($n = 10$) was utilized for both PDMS-based compositions in order to maintain a crosslink density similar to that of the PPMS-based scaffolds. This higher concentration of PDMS-MA also parallels the concentration of

78

PDMS$_{star}$-MA combined with PEG-DA in our prior studies, where osteoinductivity and bioactivity of siloxane-containing scaffolds were established.[89]

Templated scaffolds were prepared by photocuring of DCM-based precursor solution, followed by subsequent drying and hydration, with methods previously reported.[89, 216] Due to their hydrophobicity, siloxane (e.g. PDMS-MA) and phosphonated-siloxane macromers (e.g. PPMS-DA and PPMS-DA 25%) have limited solubility in water. Our prior work demonstrated that, for PDMS$_{star}$MA/PEG-DA scaffolds, the distribution of the siloxane macromer within the hydrogel was improved when a DCM precursor solution was used in the fabrication; however, some phase separation of the solution was still observed.[89] Additionally, the mold design (i.e. 'hole-in-cap') afforded a faster penetration of the precursor solution through the fused salt template such that it could be quickly subjected to UV cure, reducing the potential phase separation. Herein, DCM precursor solutions based on PPMS-DA and PPMS-DA 25% were clear and exhibited no signs of phase separation. CLSM images of Nile-red stained scaffolds permitted assessment of the distribution of siloxane and phosphonated-siloxane macromers within the PEG-DA matrix (**Figure 3-3**). For scaffolds based on PPMS-DA (i.e. ***PPMS 15:85, PPMS 30:70,*** and ***PPMS 45:55***) and PPMS-DA 25% (i.e. ***PPMS-25%***), the distribution was very uniform and greater levels of PPMS-DA produced the expected greater intensity. A uniform distribution was also observed for scaffolds containing PDMS-MA (i.e. ***PDMS 12:88*** and ***PDMS 30:70***), despite some degree of phase separation of the precursor solution. For the ***VP*** scaffold, the hydrophilicity of the vinyl phosphonate prohibited staining as confirmed in the CLSM image. Lastly, indicative of efficient crosslinking over

the fused salt template, the sol content of the scaffolds was minimized (< 8 wt%) and similarly observed for analogous non-porous slabs (**Figure A-10**).
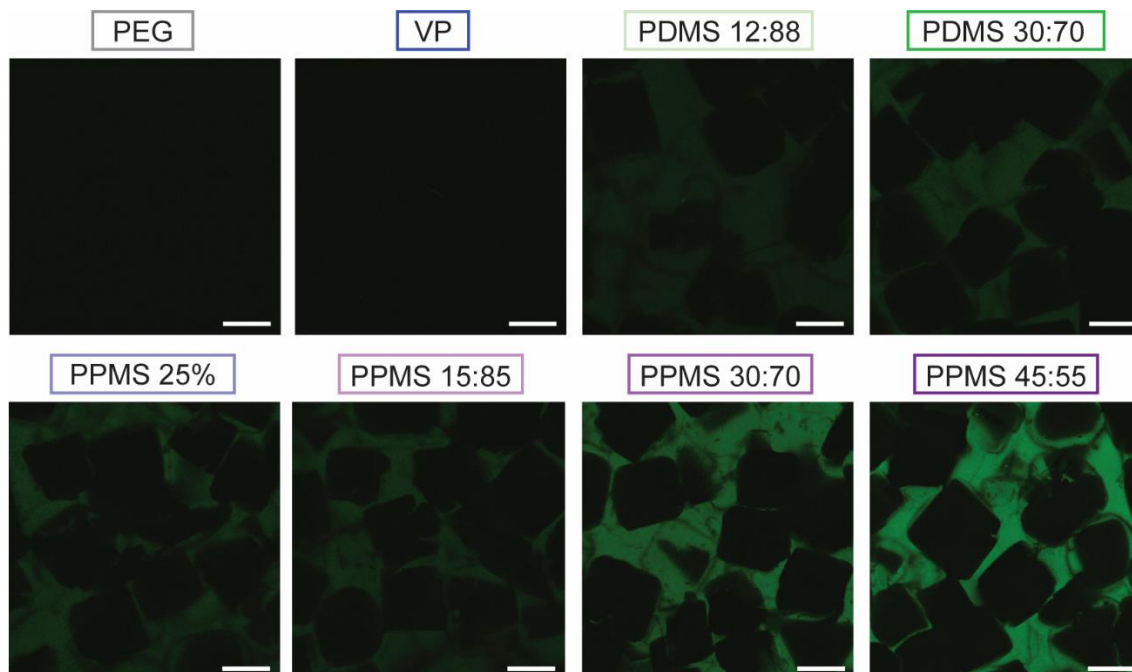
Figure 3-3. CLSM imaging of stained scaffolds. Green is assigned to siloxane- or phosphonated siloxane-rich regions, stained by hydrophobic Nile red. Photos are adjusted +20% brightness and -20% contrast for clarity. Scale bars = 250 µm.

3.4.3. Pore Size & Morphology

Scaffold pore size (**Figure 3-4A**) and morphology (**Figure A-11**) was examined by SEM (dehydrated specimens) and brightfield microscopy (hydrated specimens). For all compositions, given the use of the same salt template (i.e. salt sieved to 268 ± 35 µm and fused), no differences in pore sizes in the dry state were observed. Further, when hydrated, despite varying content of hydrophobic siloxane- or phosphonated-siloxane, a similar average hydrated pore size of ~370 µm was achieved and is within the range associated with promoting bone regeneration.[74] For all compositions, SEM images revealed the

expected high degree of pore interconnectivity, similar to that which was previously observed with fused salt templating.[89]
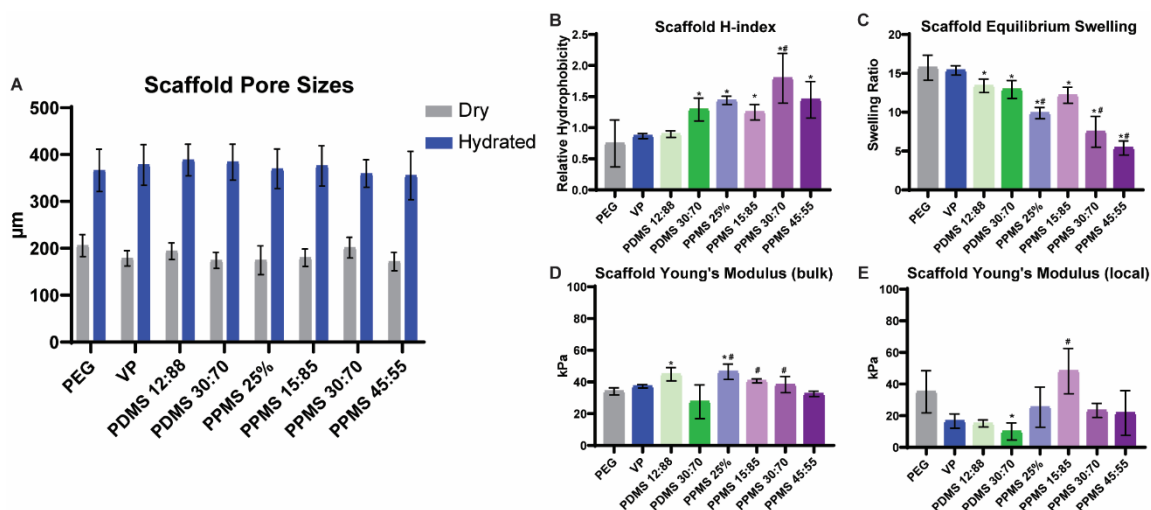
Figure 3-4. (A) Scaffold average pore size in dry and hydrated states, **(B)** scaffold equilibrium swelling, **(C)** scaffold hydrophobicity index (H-index)**, (D)** scaffold bulk Young's modulus, and **(E)** scaffold local Young's modulus. Statistical difference versus the *PEG* is represented as * and versus the *PDMS 30:70* is represented as # ($p < 0.05$).

3.4.3. Hydration and Modulus

Given the relationship between hydrogel swelling (i.e. hydration) and modulus, these properties were measured and considered collectively. The inclusion of hydrophobic phosphonated-siloxane macromers was anticipated to impact hydrophobicity and thus hydration. The H-index has been shown to better resolve differences in hydrogel hydrophobicity versus goniometry or protein adsorption studies.[249] An increase in hydrogel hydrophobicity is reflected in an increase in the H-index due to a corresponding increase in material affinity for the lower-polarity solvent (IPA) relative to DI water. Thus,

81

the H-indices of the scaffolds were measured (**Figure 3-4B**). Versus *PEG*, inclusion of PPMS-DA and PPMS-DA 25% significantly increased scaffold hydrophobicity as did PDMS-MA at the higher concentration (*PDMS 30:70*). For scaffolds containing VP (*VP*) and the lower concentration of PDMS-MA (*PDMS 12:88*), scaffold hydrophilicity was similar to that of *PEG*. The *PPMS 30:70* scaffold was slightly more hydrophobic than the *PDMS 30:70* scaffold. While phosphonate groups are generally hydrophilic, the affiliated carbon-containing portions herein (i.e. ethyl groups in diethyl phosphonate and carbon chain connecting to siloxane) may have contributed to this slight increase in hydrophobicity. Overall, the increase in hydrophobicity of these scaffolds was anticipated to promote calcium phosphate nucleation.[233] The equilibrium swelling of the scaffolds was also measured (**Figure 3-4C**). As expected, based on their increased hydrophobicity, swelling of scaffolds containing PPMS-DA and PPMS-DA 25% decreased relative to *PEG*. Compared to the **PDMS** *30:70* scaffold, the *PPMS 30:70* scaffold exhibited lower swelling. Interestingly, despite reduced swelling, all scaffolds maintained similar pore sizes which may be attributed to pore wall hydration (**Figure 3-4A**). In this way, hydrophobicity and hydration are decoupled from pore size.

Both the bulk (**Figure 3-4D**) and local (**Figure 3-4E**) modulus values of scaffolds were assessed. While a reduction in hydrogel swelling is associated with an increase in modulus, differences in bulk moduli were rather minor and is attributed to their high macroporosity. Scaffolds based on PPMS-DA exhibited moduli similar to that of *PEG* (~40 kPa). For the *PPMS 25%* and *PDMS 30:70* scaffolds, moduli were statistically higher than *PEG*. The local Young's modulus of scaffolds, at a scale on the order of

cellular interactions,[28] may be measured using AFM by pore wall indentation. The **_PDMS 30:70_** scaffold showed a significant decrease in local modulus versus **_PEG_**, as expected with previous results.[89] However, all other scaffolds, including those based on PPMS-DA and PPMS-DA 25%, exhibited statistically similar local moduli values compared to **_PEG_**. In this way, these scaffolds exhibit hydrophobicity that is decoupled from modulus.

Finally, analogous non-porous slabs were prepared and evaluated in terms of equilibrium swelling and compressive moduli were examined to observe effects in the absence of macroporosity (**Figure A-11**). Only for non-porous slabs prepared with a higher concentration of PPMS-DA (i.e. **_PPMS 30:70_** and **_PPMS 45:55_**; ~1 MPa) did the moduli values increase versus other slabs (~0.7 MPa) which coincided with a reduction in swelling.
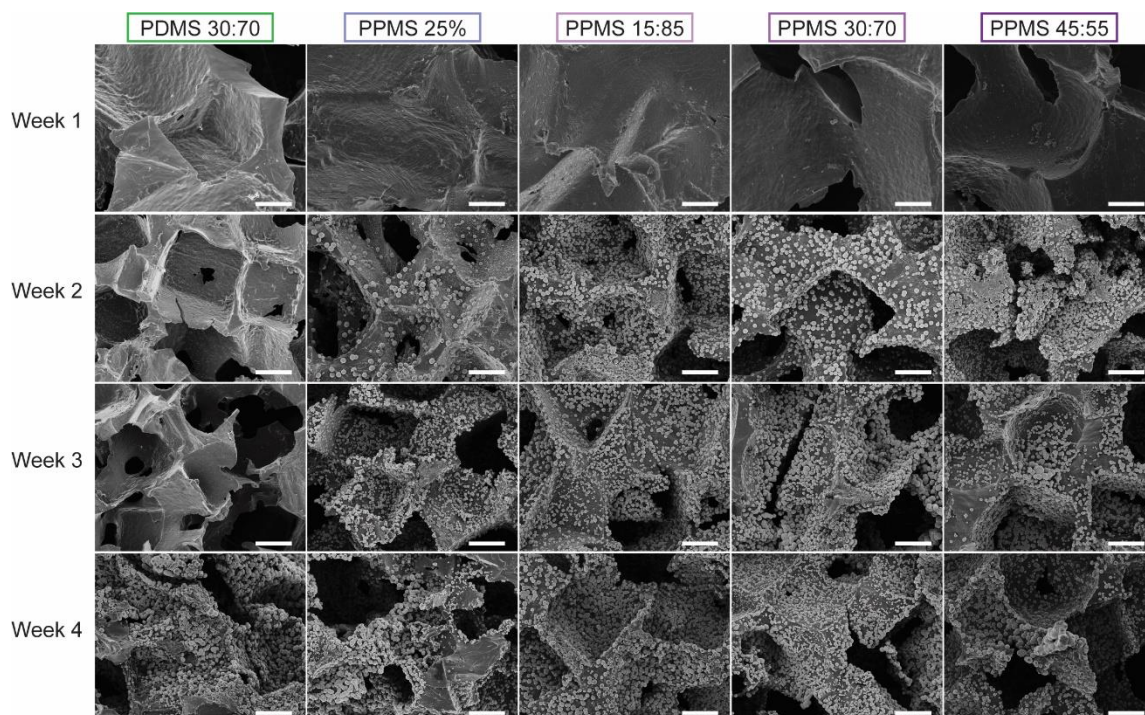
Figure 3-5. SEM images of scaffolds displaying HAp mineralization after soaking in simulated body fluid (SBF, 1X, 37 °C). Week 1 images' scale bars = 50 µm and weeks 2-4 images' scale bars = 100 µm.

3.4.4. Bioactivity

In our earlier report, a scaffold equivalent to **PDMS 30:70** but prepared with PDMS$_{star}$-MA (rather than linear PDMS-MA) demonstrated an ability to induce HAp mineralization after exposure to SBF[224] (1X, 37 °C; 4 weeks) while the **PEG** scaffold did not.[89] Based on the addition of a phosphonate pendant groups to the siloxane and the observed increase in hydrophobicity, scaffolds containing PPMS-DA and PPMS-DA 25% were anticipated to be more bioactive. Thus, scaffold mineralization was evaluated weekly over a 4-week period versus a known bioactive control, **PDMS 30:70**, to determine if there is an enhancement (**Figure 3-5**). The siloxane-containing scaffold (i.e. **PDMS 30:70**) only

exhibited mineralization at 4 weeks. However, scaffolds containing PPMS-DA or PPMS-DA 25% showed mineralization at just two weeks. Interestingly, the *VP* scaffold mineralized only at 4 weeks (**Figure A-13**). Thus, the more rapid mineralization of PPMS-based scaffolds is attributed to the combination of a siloxane backbone and phosphonate pendant groups.

3.4.5. Cell attachment and Cytotoxicity

After 48 h culture in normal media, all RGD-containing scaffolds were determined to be non-cytotoxic relative to the *PEG* control (**Figure 3-6A**). Scaffolds were further examined through confocal microscopy after staining with DAPI and Rhodamine Phalloidin (**Figure 3-6B**), displaying-robust hBMSC attachment and spreading within the 3D hydrogels.
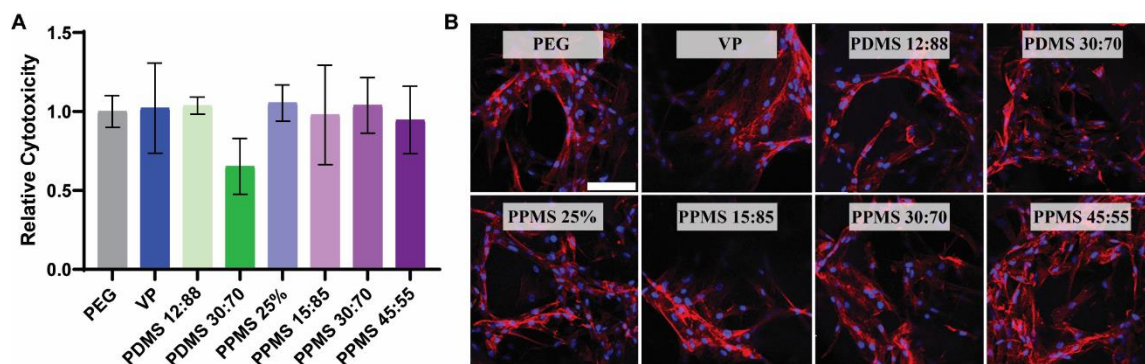
Figure 3-6. Scaffold non-cytotoxicity, relative to *PEG*, following 48 h hBMSC culture as determined by **(A)** LDH assay and **(B)** representative rhodamine phalloidin (red) and DAPI (blue) stacked confocal images Error bars denote standard error of mean. Scale bar = 100 µm.

3.4.6. Scaffold-Induced Mineralization and Osteogenic Protein Expression

RGD-containing scaffolds were evaluated for bioactivity and osteoinductivity after hBMSC culture in non-osteogenic media for 14 and 28 days. Bioactivity (i.e. mineralization) was evaluated by Alizarin Red S staining and quantified spectrophotometrically using a technique adapted from Gregory et al.[248] Scaffold-induced osteogenesis was evaluated by relative protein levels of relevant bone extracellular matrix proteins and growth factors including bone morphogenetic protein-2 (BMP-2), secreted protein acidic and rich in cysteine (SPARC) and collagen type 1 α1 (COL1A1).
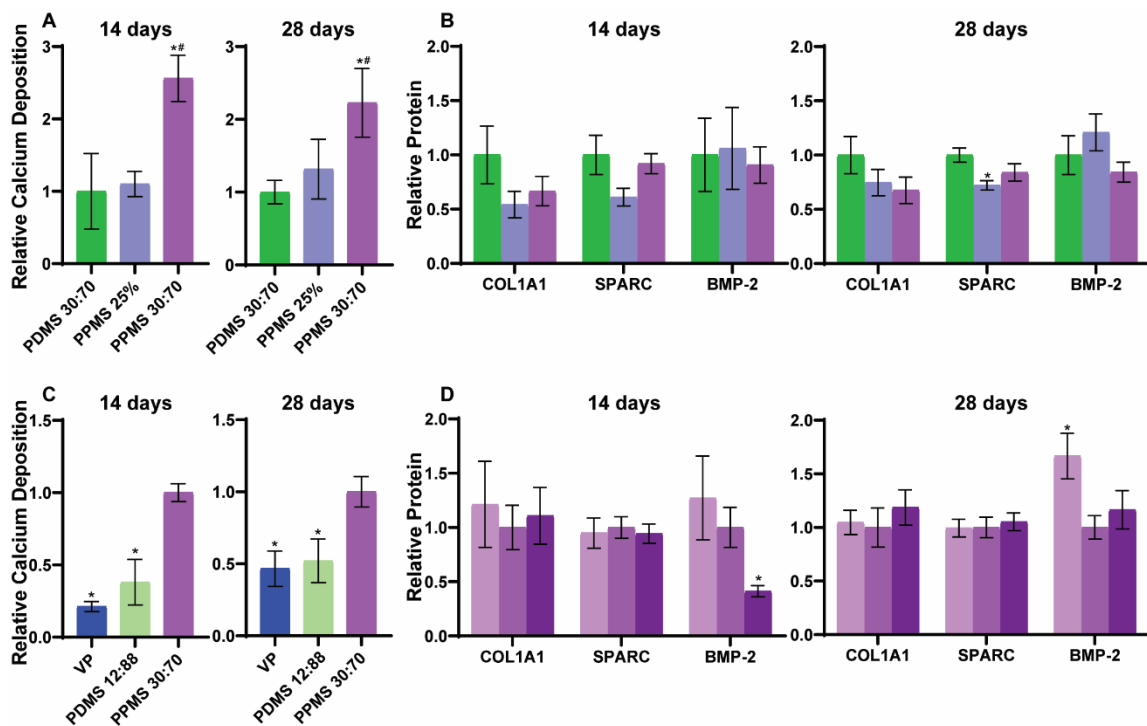
Figure 3-7. Following 14- and 28-day hBMSC culture on scaffolds, for **PPMS 25%** and **PPMS 30:70**: **(A)** relative calcium deposition and **(B)** relative protein levels versus **PDMS 30:70**. Following 14- and 28-day hBMSC culture on scaffolds, **(C)** relative calcium deposition of **PPMS 30:70** versus **VP** and **PDMS 12:88** and **(D)** relative protein levels of

PPMS 15:85 (light purple), ***PPMS 30:70*** (medium purple), and ***PPMS 45:55*** (dark purple). Calcium deposition values were normalized to the scaffold weight. Protein expression values are normalized to DNA measures. Statistically significant difference is represented with * versus ***PDMS 30:70*** and [#] versus ***PPMS 25%*** in **(A)** and **(B)**, and with * versus ***PPMS 30:70*** in **(C)** and **(D)** ($p < 0.05$) and error bars represent standard error of mean.

In the first series of culture experiments, the ***PDMS 30:70*** scaffold served as a control based on the previously observed bioactivity and osteoinductivity of a similar PDMS-containing scaffold.[89] The phosphonated-siloxane scaffold with the similar mol% macromer ratio (i.e. ***PPMS 30:70***) was evaluated as well as the ***PPMS 25 %*** scaffold. After 14 days (**Figure 3-7A, A-16**), hBMSCs cultured on ***PPMS 30:70*** (i.e. higher phosphonate concentration) displayed an increase in calcium deposition relative to ***PDMS 30:70*** (~2.6-fold, $p < 0.001$) and ***PPMS 25%*** (~2.3-fold, $p < 0.001$). The calcium deposition profile displayed a similar trend after 28 days in culture, maintaining a significant increase in ***PPMS 30:70*** relative to ***PDMS 30:70*** (~2.2-fold, $p = 0.001$) and ***PPMS 25%*** (~1.7-fold, $p = 0.008$). Following 14 days of culture, protein expression profile of COL1A1, SPARC and BMP-2 from hBMSCs displayed no statistical differences (**Figure 3-7B**). Although not significant, it is noteworthy to mention, however, the observed decrease in SPARC expression in ***PPMS 25%*** cultures relative to ***PDMS 30:70*** ($p = 0.076$) and ***PPMS 30:70*** ($p = 0.174$). Interestingly, after 28 days, the expression of SPARC displayed a statistically significant decrease in ***PPMS 25%*** cultures relative to ***PDMS 30:70*** (~0.7-fold, $p = 0.014$). Although COL1A1 displays a decreasing trend across our groups, no statistical differences were observed ($p = 0.199$). Cumulatively, these

results suggest that a greater phosphonate content incorporated into the siloxane (i.e. PPMS-DA) elicits a greater osteoinductive response as evident by the increased calcium deposition.

In a second series of culture experiments, the PPMS-DA containing scaffolds were compared to *VP* (i.e. no siloxane) and *PDMS 12:88* (i.e. low siloxane content). Following 14 days of culture, we observed a ~0.2-fold and ~0.4-fold decrease in calcium deposition by hBMSCs in *VP* ($p < 0.001$) and *PDMS 12:88* ($p = 0.030$) cultures, respectively, relative to *PPMS 30:70* (**Figure 7C, A-17**). Similarly, at 28 days, hBMSCs maintained a decreased calcium deposition in *VP* (~0.5-fold, $p = 0.019$) and *PDMS 12:88* (~0.5-fold, $p = 0.033$) cultures relative to *PPMS 30:70*. No differences, however, were observed in the protein expression profile of COL1A1, SPARC and BMP-2 relative to *PPMS 30:70* at either timepoints (**Figure A-14**). Overall, the results suggest that the addition of phoshonate pendant groups to the siloxane macromer's backbone enhances calcium deposition, beyond what is promoted by siloxane or phosphonate alone.

In a final series of culture experiments, the impact on the scaffold concentration of PPMS-DA was evaluated for *PPMS 12:88*, *PPMS 30:70*, and *PPMS 45:55*. Assessment of calcium deposition revealed no differences among these (**Figure A-15, A-18**). Likewise, the expression of COL1A1 and SPARC was not altered by changing the phosphonate molar percentage at either 14 or 28 days (**Figure 3-7D**). In contrast, a ~0.4-fold decrease in BMP-2 expression was observed for the *PPMS 45:55* cultures relative to *PPMS 30:70* ($p = 0.046$) at the 14-day timepoint. Although a similar pattern in BMP-2 expression was observed between *PPMS 15:85* and *PPMS 45:55* cultures, the difference

fell below statistical significance ($p = 0.138$). Interestingly, following 28 days of culture, the observed difference in BMP-2 expression between **PPMS 30:70** and **45:55** was diminished. However, an increase in BMP-2 expression in **PPMS 15:85** cultures relative to **PPMS 30:70** (~1.7-fold, $p = 0.048$) was observed. This finding is particularly interesting in view of the reported enhanced osteogenic differentiation of hBMSCs through autocrine BMP-2 signaling or following BMP-2 treatment.[250, 251] Overall, these results suggest that such changes in the phosphonate content of phosphonated-siloxanes have little effect on calcium deposition, or on expression of osteogenic ECM markers COL1A1 and SPARC. The elevated BMP-2 expression due to decreasing phosphonate content may imply autocrine effects on the cultured h-MSCs, thereby enhancing osteogenic differentiation.

3.5. Conclusions

Herein, we have investigated the effect of a phosphonated-siloxane macromer to enhance the osteogenic potential of templated PEG-DA scaffolds for bone regeneration. Two new siloxane macromers were synthesized containing a relatively high (PPMS-DA) and low (PPMS-DA 25%) phosphonate pendant group concentration. In addition to scaffolds fabricated with these macromers, several scaffold compositions were prepared by incorporation of vinyl phosphonate (i.e. no siloxane) and PDMS-MA (i.e. no phosphonate). The phosphonated-siloxane macromers were uniformly distributed in the scaffolds as observed by CLSM. These scaffolds produced an increase in hydrophobicity versus the PEG scaffold control and an associated decrease in swelling. However, the average scaffold pore size was similar to the control scaffolds (~370 µm). Enhanced

hydrophobicity and such a pore size are associated with osteogenesis. The bulk moduli of scaffolds were not substantially different than one another due to their macroporosity and scaffolds containing phosphonated-siloxanes exhibited local Young's moduli similar to the PEG scaffold control. The enhanced bioactivity of phosphonated-siloxane based scaffolds was demonstrated by the formation of HAp just two weeks after exposure to SBF, faster than for the siloxane-based scaffold (four weeks). RGD-containing scaffolds were cultured in normal media with hBMSCs for 14 and 28 days. For a scaffold prepared with PPMS-DA, calcium deposition was greatly increased while maintaining similar protein expression versus an analogous scaffold prepared with PDMS-MA, which is known to be osteoinductive and bioactive. This suggests a potentially better osteogenic response. However, the concentration of phosphonated-siloxane macromer (PPMS-DA) did not elicit "PPMS-dose dependent" increase in protein expression. In fact, BMP-2 expression was greatest for the lowest PPMS dosage. Such results suggest a more complex mechanism that requires further investigation, including a broader set of markers over additional timepoints. Overall, when incorporated into PEG-DA hydrogel scaffolds, phosphonated-siloxane macromers exhibit enhanced hydrophobicity and calcium deposition versus a siloxane macromer. Instructive scaffolds containing this potent chemistry may ultimately improve bone regenerative potential.

CHAPTER IV

SPATIALLY-CONTROLLED TEMPLATED HYDROGELS FOR ORTHOPEDIC

INTERFACIAL TISSUE REGENERATION

4.1. Overview

Scaffolds that recapitulate the spatial complexity of orthopedic interfacial tissues is essential to their regeneration. This requires a method to readily and flexibly produce scaffolds with spatial control over physical and chemical properties, without resulting in hard interfaces. Herein, we produced hydrogel 'scaffolds with spatially tunable arrangements and chemistries' or SSTACs. Using solvent-induced phase separation/fused salt templating ("SIPS/salt"), scaffold elements are first prepared with a tunable pore size and with one or more UV-reactive macromers. After trimming to the desired di-mensions, these are physically configured and fused together to form the SSTAC. Using this method, three SSTAC designs were prepared, including one that mimicked the osteochondral interface. Maintenance of spatial control of pore size and chemical composition across a relatively soft and integrated interface was verified with microscopy. The influence of the fabrication process on modulus and the integrity of the interface was also examined.

4.2. Letter

The regeneration of orthopedic interfacial tissues critically relies on scaffold designs that recapitulate the interface or enthesis of osteochondral, tendon, and ligament tissues.[252, 253] Spatial control of scaffold chemical and physical properties could leverage materials-guided strategies wherein regeneration is guided by such properties alone, and

in the absence of exogenous growth factors. Examples of instructive scaffold properties include morphology,[113, 254] hydrophobicity,[44] chemistry,[40] and modulus.[96, 133] A strategy permitting the flexible spatial arrangement of these properties would represent a significant advancement in interfacial tissue engineering. Layered scaffolds have been investigated to regenerate orthopedic interfaces.[253, 255] These are often prepared by merging of discrete scaffolds through mechanical attachment, gluing, or freeze-drying.[231] With these approaches, a "hard interface" results, failing to mimic the more gradual transition of native tissues that is critical to avoiding interfacial mechanical failure.[231, 253] While gradient scaffolds exhibit gradual transitions,[256] these are typically only for a single material property and furthermore do not necessarily produce a tissue-like spatial distribution. Simultaneously achieving precise spatial control of several material properties and also avoiding hard interfaces remains a challenge in regeneration of orthopedic interfacial tissues. Towards this goal, we herein demonstrate the preparation of hydrogel 'scaffolds with spatially tunable arrangements and chemistries' or "SSTACs" (**Figure 4-1**).

In our previous work, we developed a method to prepare discrete hydrogel scaffolds with interconnected, macropores of tunable size through a combination of solvent-induced phase separation (SIPS) and salt-templating (i.e. "SIPS/salt").[182, 216] A UV-curable macromer or combination of macromers are dissolved in organic solvent and cast over a fused salt template. Following subsequent cure and evaporation of solvent, exposure to water leaches out the salt template and hydrates the scaffold. Using this method, templated hydrogel scaffolds were produced with poly(ethylene glycol)

diacrylate (PEG-DA). Since PEG-DA hydrogels lack innate osteoinductivity and bioactivity necessary for materials-guided bone regeneration,[48] we sought to incorporate hydrophobic, inorganic co-macromers to enhance these properties. We demonstrated that siloxane-based macromers, such as *star*-polydimethylsiloxane methacrylate (PDMS$_{star}$-MA), successfully did so.[89] Thus, using the above approach, templated PDMS-PEG hydrogel scaffolds were produced with varying siloxane content, exhibiting a uniform distribution of the siloxane macromer. More recently, templated hydrogel scaffolds were likewise prepared with a phosphonated-siloxane macromer, poly(diethyl(2-(propylthio)-ethyl) phosphonate methylsiloxane) diacrylate (PPMS-DA).[257] Such PPMS-PEG hydrogel scaffolds exhibited a further enhanced osteogenic effect. Thus, this SIPS/salt fabrication strategy provides a method to generate macroporous scaffolds with tunable pore size and chemistry. Towards regeneration of native-like orthopedic interfaces, we sought to transform such discrete scaffolds layers into monolithic scaffolds or "SSTACs". In this fabrication process, two or more scaffold "elements" (individually produced via the aforementioned SIPS/salt method) are each formed in the desired geometry and dimensions and then merged together into a SSTAC of a desired configuration. Thus, the chemical and physical properties are spatially controlled, leveraging instructive material properties for regeneration and mimicking native osteochondral tissues with fidelity.
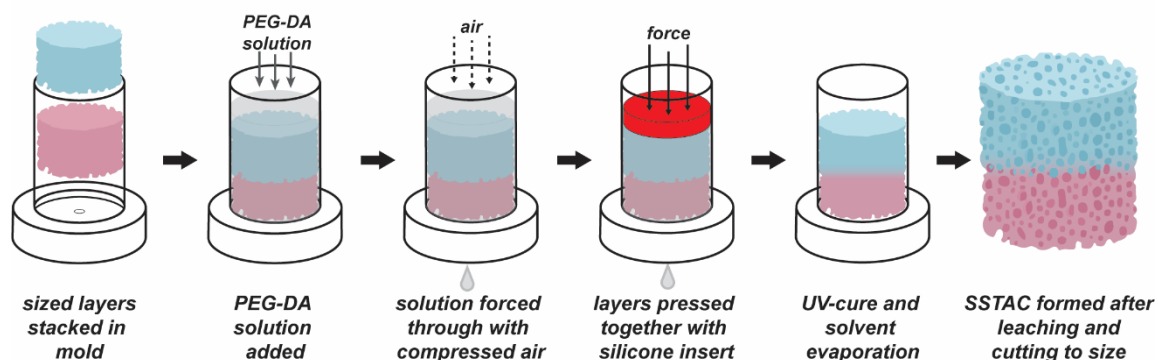
Figure 4-1. General strategy for the fabrication of hydrogel 'scaffolds with spatially tunable arrangements and chemistries' (SSTACs). Two or more scaffold layers of varying physical and chemical properties and having designated thicknesses and/or geometries may be merged across soft interfaces towards the regeneration of osteochondral interfacial tissues.

Fabrication of SSTACs proceeds in a series of common steps. In this report, SSTACs were formed as cylinders to resemble autograft plugs used to treat osteochondral defects (**Figure 4-1**). Prior to salt-leaching, individual scaffold layers (of a designated chemistry and pore size) were trimmed to the desired dimensions and geometries (**Figure A-19**). Two or more layers are then combined in the desired arrangement within the cylindrical mold. This mold is similar to the mold in which each layer was originally fabricated (**Figure A-20**). It is comprised of a glass tube with a Teflon cap containing a small hole in its center with a sheet of aluminum foil separating the two. The scaffold elements are fused together as follows. A DCM-based PEG-DA precursor solution (30 wt%) is added to the mold, the foil pierced, and compressed air used to force the solution through the scaffold components, with the excess exiting the bottom of the mold. Finally, a silicone disc (matching the mold inner diameter) is gently pushed into the mold,

squeezing out residual solution and physically securing the component scaffolds together. The mold is then sequentially exposed to UV-light (15 minutes), the solvent from the precursor solution evaporated overnight, and the salt template leached out by exposure to water, yielding the hydrated SSTAC. In a last step, the outer surface is removed by punching the SSTAC with a die of the desired diameter. This fabrication process affords flexible, precise control over spatial organization of scaffold elements. Because the PEG-DA precursor solution is forced through the salt-containing scaffold elements (i.e. before the template is removed), pores are not undesirably filled. Furthermore, the use of a PEG-DA solution to merge the scaffold layers importantly results in a relatively soft interfaces with good relative interfacial shear strength. This is attributed to the solubility and uniform distribution of the precursor solution throughout the salt-containing scaffold elements. Finally, SSTAC geometries other than cylinders may be likewise produced by simply employing the designated mold geometry. Herein, we demonstrated the efficacy and flexibility of this method by producing three series of hydrogel SSTACs with layered, radial, and osteochondral-like configurations.
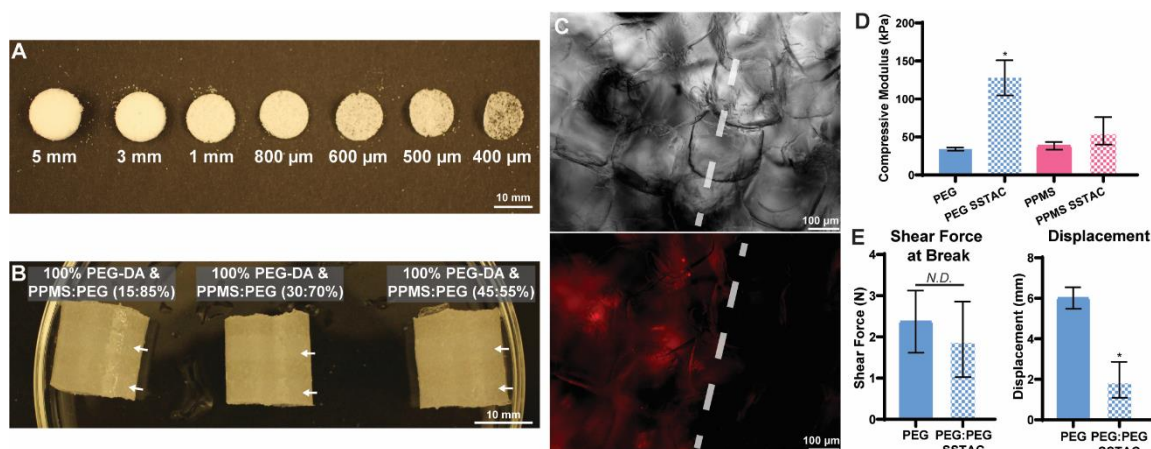
Figure 4-2. (A) Salt-containing scaffold elements may be trimmed to thicknesses as low as 500 µm prior to incorporation into SSTACs. **(B)** Four-layered SSTACs with alternating 100% PEG-DA and PPMS:PEG scaffold elements of varying mol% ratio of PPMS-DA to PEG-DA; arrows denote PPMS-containing layers. **(C)** For a hydrated 4-layered SSTAC [100% PEG-DA & PPMS:PEG (30:70 mol%)], brightfield (top)/fluorescent (bottom) imaging of the interface (denoted with white dashed line) with the PPMS-containing layer stained with Nile red dye. **(D)** For 100% PEG-DA and a PPMS:PEG (30:70 mol%): compressive modulus before and after formation into a SSTAC (* = $p < 0.05$ versus corresponding control; ND = $p > 0.05$). **(E)** For 100% PEG-DA: shear force at break along the interface (left) and corresponding shear displacement (right) before and after formation into a PEG:PEG SSTAC (* = $p < 0.05$ versus corresponding control; ND = $p > 0.05$).

SSTACs comprised of four "alternating" layers were first prepared (**Figure 4-2**). Scaffold elements (i.e. layers) were individually fabricated via SIPS/salt with the same pore size but with different chemistries. For each layer, the salt template was prepared with the same average salt size (268 ± 35 µm). Scaffold elements were made with PEG-DA or with both PPMS-DA and PEG-DA at 15:85, 30:70, and 45:55 mol%. The salt-containing scaffold elements could readily be trimmed to a range of thicknesses using a vibratome (Leica VT1000S; **Figure A-21**), maintaining integrity down to 500 µm (**Figure 4-2A**). At smaller thicknesses of 400 µm or less, salt crystals began to fragment from the

disc. Using the process described above, four scaffold elements of the same thickness (height = 2 mm) were assembled into SSTACs having two PPMS:PEG layers alternated with two PEG layers. Despite the swelling produced during the final step (hydration), intact monolithic SSTACs scaffolds resulted. Layers were visible due to the relative opacity of the PPMS:PEG layers (**Figure 4-2B**). To visualize the interface between layers, the SSTACs were treated with a hydrophobic dye (Nile red) to stain the PPMS-containing layers and examined under brightfield and fluorescence (Zeiss AxioVert.A1) (**Figure 4-2C**). Brightfield imaging revealed the targeted pore size (~370 μm) and interconnected pore morphology. The fluorescent images confirmed the desired, relatively soft interface nature between two layers. Next, the mechanical properties of the SSTACs were evaluated to assess the impact of merging the scaffold layers together. First, from the SSTACs comprised of alternating 100% PEG-DA and PPMS:PEG (30:70 mol%), individual layers were sliced and subjected to an unconfined compression test and compared to analogous scaffolds (i.e. not formed into SSTACs) (**Figure 4-2D**). The 100% PEG-DA layer of the SSTAC exhibited a higher modulus versus the PEG-DA control. However, the PPMS:PEG (30:70 mol%) layer of the SSTAC had a similar modulus versus the corresponding control. These results are attributed to a greater absorption of the passing PEG-DA precursor solution by the salt-containing 100% PEG-DA layer, due to its similar chemistry, versus by the PPMS:PEG (30:70 mol%) layer. Next, the mechanical integrity of the SSTAC interface was investigated. Bilayered SSTACs composed of two layers of 100% PEG-DA were first compared to the corresponding 100% PEG-DA single scaffolds (i.e. not formed as SSTACs). These were tested in a confined shear configuration where

the central interface was aligned with the shear plane. Shear strain was applied at a rate of 2 mm/min until failure. Both the SSTACs and the corresponding conventional scaffolds experienced failure at a similar value of shear force although the displacement at failure was lower for the former (**Figure 4-2E**). These results indicate that SSTACs should be able to withstand shear forces in a confined environment.
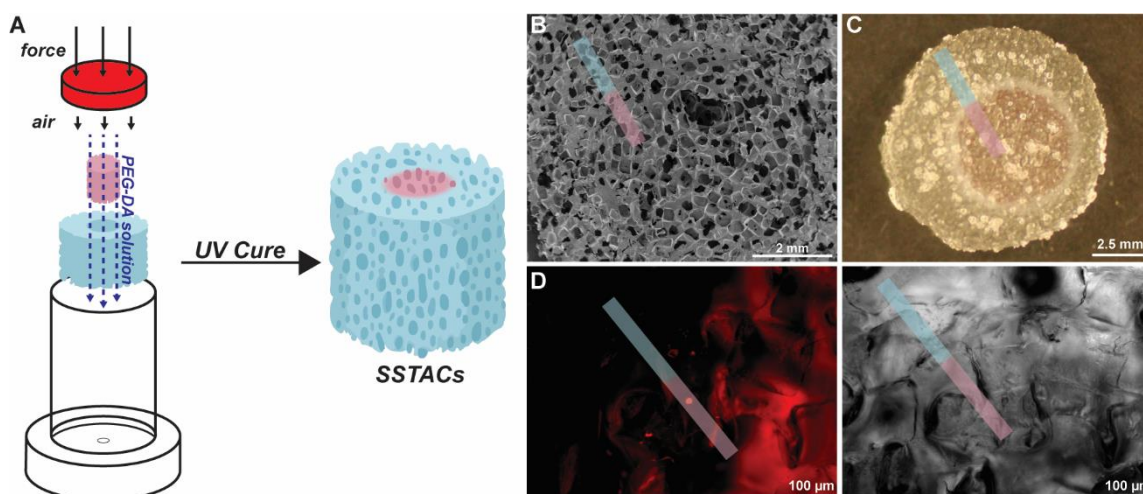
Figure 4-3. (A) Fabrication of hydrogel SSTAC with a radial geometry, comprised of a 100% PEG-DA exterior ring and a PPMS:PEG (30:70%) core. Cross-section of radial SSTAC (colored transparent bar denotes 100% PEG-DA "blue" and PPMS:PEG "pink" along the interface): **(B)** SEM image, **(C)** photograph of Nile Red stained specimen, **(D)** Fluorescent [left] and brightfield [right] image of stained specimen.

Next, with an analogous protocol, SSTACs were formed with a radially layered geometry (**Figure 4-3A**). Both layers were formed with a similar salt template (average salt size of 268 ± 35 μm). The 100% PEG-DA exterior layer was prepared by trimming the salt-containing scaffold to an 8 mm height and creating a central hole with a 6 mm die.

The PPMS:PEG (30:70 mol%) exterior layer was prepared by trimming the salt-containing scaffold to 6 mm x 8 mm (diam. x height) which was then placed into the PEG-DA layer's empty core. Following subsequent steps to fuse the layers together, the final hydrated radial SSTAC was punched with a die to remove the outer surface. The cross-section of a final hydrated SSTAC was analyzed to assess the spatial control of porosity and chemical composition across the radial interface. By SEM, an interconnected pore morphology was observed to be maintained and the interface between the layers lacked a hard interface (**Figure 4-3B**). After exposing the SSTAC to hydrophobic Nile Red to stain the PPMS:PEG (30:70 mol%) core, the spatial control of chemistry was visually confirmed (**Figure 4-3C**). Under fluorescent and brightfield imaging, the radial interface was well integrated despite the targeted differences in chemistry (**Figure 4-3D**).
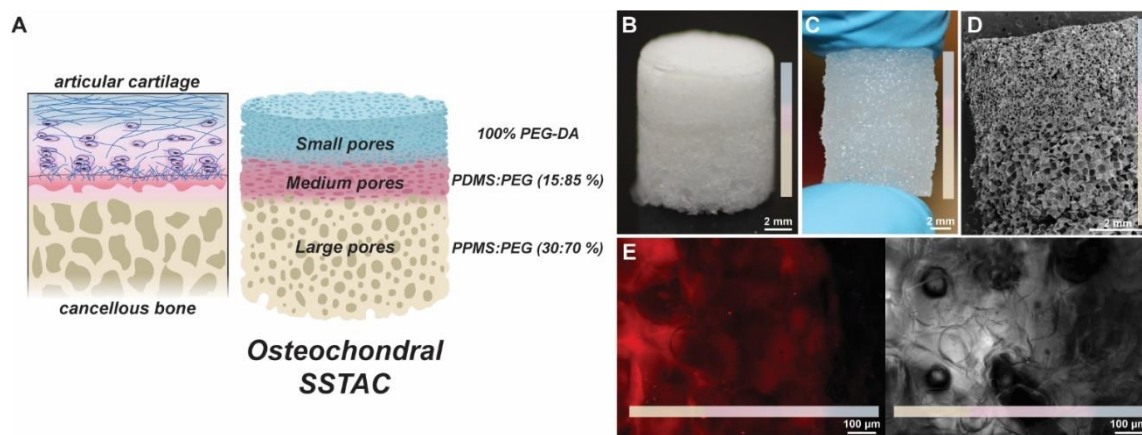
Figure 4-4. **(A)** Mimetic osteochondral SSTAC design: **(B)** Photograph of SSTAC prior to salt template leaching, **(C)** Photograph of final hydrated SSTAC, **(D)** SEM image, and **(E)** Fluorescent [left] and brightfield [right] image of stained specimen.

In a final example, we demonstrated the formation of a triphasic SSTAC that spatially recapitulates the native osteochondral tissue (**Figure 4-4A**). The three layers corresponded to the articular cartilage, osteochondral interface, and subchondral bone. The pore size and chemistry of each layer was based on that which is expected to promote regeneration of each tissue types. First, the SSTAC's "cartilage layer" (height = 2.5 mm), was prepared with 100% PEG-DA and a relative 'small' sized salt template (salt size of 102 ± 20 µm). The smaller pore size and high hydration of this layer are properties associated with instructing cartilage regeneration.[231] Representing the subchondral bone layer, a scaffold layer (height = 5 mm) was prepared with 'large' sized salt template (268 ± 35 µm salt size) and PPMS-DA:PEG-DA (30:70 mol%). The large pore size as well as osteoinductive and bioactive nature of this chemistry would be expected to promote bone.[113, 231, 257] Finally, at the interface, a scaffold layer (height = 500 µm), was prepared with 'medium' sized salt template (181 ± 29 µm salt size), to provide a more gradual transition in pore size from the cartilage to subchondral bone layer. This interface layer was prepared with PDMS-MA at low concentrations, PDMS:PEG (15:85 mol %). This "non-phosphonated" siloxane and lower concentration is expected to provide an intermediate bioactive response versus the other layers, affording the desired biomimetic transition from cartilage to bone. The resulting three-layered osteochondral SSTAC exhibited excellent integration among layers despite the differences in pore size and chemical composition (**Figure 4-4B-E**).

In conclusion, we described a new strategy to prepare templated hydrogel scaffolds with spatially controlled properties. The resulting SSTACs ('scaffolds with spatially

tunable arrangements and chemistries') can be formed from elements prepared with a variety of macromer combinations, different pore sizes, as well as dimensions and geometries. These SSTACs are anticipated to be useful for the regeneration of orthopedic interfacial tissues, particularly the osteochondral interface. The fabrication of SSTACs affords tremendous flexibility. Prior to leaching of the salt template, individually prepared scaffold elements are trimmed to the desired dimensions and assembled in the desired configuration. These elements are fused together into a monolithic SSTAC by passage of a macromer precursor solution and subsequent UV curing. Following salt leaching and hydration, the SSTAC exhibits relatively soft interfaces between the unique areas. Towards enhancing the instructive potency of SSTACs, other macromer chemistries, fillers, or even growth factors could be incorporated.

4.3. Experimental

4.3.1. Materials

2,2'-azobis(2-methylpropionitrile) (AIBN), acryloyl chloride, diethyl vinyl phosphonate (VP), hexamethyldisilazane (HMDS), hydrochloric acid (HCl), magnesium sulfate (MgSO$_4$), Nile red, poly(ethylene glycol) 3350 (PEG-3350), potassium carbonate (K$_2$CO$_3$), sodium chloride (NaCl), sodium hydroxide (NaOH), thiolacetic acid, triethylamine, trifluoromethanesulfonic acid (triflic acid) and all solvents were obtained from Sigma-Aldrich. 1,3,5,7-tetravinyl-1,3,5,7-tetramethylcyclotetrasiloxane (D$_4$ vinyl), 1,3-bis(3-methacryloxypropyl)tetramethyldisiloxane (tetra-SiMA), 1,3-bis(4-hydroxybutyl)tetramethyldisiloxane (HBTMDS), and octamethylcyclotetrasiloxane (D$_4$) were obtained from Gelest. Diethyl ether was obtained from Fisher Scientific. Phosphate

buffered saline (No Ca or Mg; PBS) was obtained from Corning. Ethyl (2,4,6-trimethylbenzoyl) phenylphosphinate was obtained from Combi-Blocks.

4.3.2. Synthesis of Scaffold Components

4.3.2.1. PEG-DA Synthesis

PEG-DA (M_n = 3400 g/mol) was prepared as previously reported.[217]

4.3.2.2. PPMS-DA Synthesis

PPMS-DA (M_n = 3231 g/mol) was prepared as previously reported through a five-step synthetic process.[257]

4.3.2.3. PDMS-MA Synthesis

PDMS-MA (M_n = 1044 g/mol) was prepared as previously reported.[257]

4.3.2.4. NMR

^{1}H-NMR spectra were obtained on an 'Ascend 400' 400 MHz spectrometer operating in the Fourier transform mode. Solutions of 5% (w/v) $CDCl_3$ were used to obtain spectra. Residual $CHCl_3$ served as an internal standard. ^{1}H-NMR spectra of all synthesized materials were in agreement with that which was previously reported.

4.3.3. Precursor Solution Preparation

Dichloromethane (DCM) based precursor solutions at 30 wt% total macromer to DCM were prepared as previously reported.[257] PPMS:PEG (45:55, 30:70, and 15:85) and PDMS:PEG (15:85) compositions represent the mol% ratio of siloxane:PEG-DA, which collectively represent the total macromer added to DCM (~30 wt%). Photoinitiator (ethyl (2,4,6-trimethylbenzoyl) phenylphosphinate) was added at 0.01 g/g of macromer.

Solutions were vortexed 1 min after addition of each component and again prior to addition to the mold.

4.3.4. Salt-Templated Scaffold Fabrication

Hydrogel scaffolds were fabricated via SIPS/Salt as previously reported.[89] Sieved NaCl [ASTM E-11 specifications No. 40 (425 µm opening), No. 60 (250 µm opening), and No. 100 (150 µm opening)] at sizes of ~100 µm, ~180 µm and ~268 µm (as determined by ImageJ analysis of SEM images) were used to form the templates.[182] Molds were formed from a borosilicate glass tube (inside diameter = 0.5 inch) with aluminum foil inside a Teflon cap containing a small hole in the bottom. A 5 wt% water-salt mixture was then added to the mold, compacted and centrifuged (Eppendorf 5810R centrifuge, A-4-62 rotor). The salt template was then allowed to dry in a fume hood for 24 h. A precursor solution was deposited atop the dried salt template via syringe, the aluminum foil punctured through the hole in the Teflon cap, and the solution forced through with compressed air. Once the solution had visibly finished passing through the mold's hole, the mold was exposed to UV light [UV-transilluminator; 6 mW cm2, 365 nm] for 15 min. After the solvent was allowed to evaporate in a fume hood for 24 h, the resulting cured, salt-containing scaffold was sectioned into a desired thickness using a vibratome (Leica VT1000S; cutting speed = 1.75 mm/s; frequency = 30 Hz). In one case, a die was used to punch the scaffold to a smaller diameter.

4.3.5. Fabrication of SSTACs

The cured, salt-containing scaffold "elements" were prepared and sized as described above. These elements were added in the desired configuration to the glass

mold, the same design described above. Next, the 100% PEG-DA precursor solution (~1.5 mL) was added to the mold, and allowed to soak for ~1 min. As described above, the aluminum foil was then punctured through the hole in the Teflon cap, and compressed air applied to push the precursor solution through the template and out the hole. A 3 mm thick silicone rubber insert (matching the ID of the glass mold) was subsequently inserted and any excess precursor solution squeezed out with gentle pressure. The insert was left in place to secure the scaffold elements prior to and during curing. The mold was exposed to UV light [6 mW cm^2, 365 nm] for 15 min with rotation (12 min upright, and 3 min upside down). The Teflon cap was removed from the mold, and the solvent from the resulting salt-containing SSTAC (still contained within the glass tube) allowed to evaporate for 24 h in a fume hood. The salt-containing SSTAC was then removed from the glass tube and soaked for 48 h in DI water (3X daily water changes) to remove the salt template and to hydrate the SSTAC. After words, the top and bottom 1 mm of the cylindrical SSTAC was sliced with a razor blade and lastly punched with a die to the desired diameter, removing the outer surface.

4.3.6. Characterization Techniques

4.3.6.1. Scanning Electron Microscopy (SEM)

SSTACs (8 mm diameter) were dried in a vacuum oven (14.7 psi, 24 hr, room temperature [RT]). Dried discs were subjected to Au-sputter coating (Cressington Sputter Coater 108) and viewed with a field emission scanning electron microscope (SEM; JEOL NeoScope JCM-5000) at an accelerated electron energy of 10 keV.

4.3.6.2. Brightfield/Fluorescent Imaging

Images were captured using a Zeiss AxioCam 503 mono camera attached to a Zeiss Axiovert.A1 fluorescent microscope at 5x magnification under brightfield or fluorescent LED light source (filter # 43; Cy3/Rhodamine/Alexa 546). Images were processed using Zeiss ZEN blue software version 3.1.

4.3.6.3. Compressive Modulus

The compressive elastic modulus of scaffolds or SSTAC sections was determined using an Instron 5944 at RT. Scaffolds were punched into discs (~10 mm x ~2 mm, diameter x thickness) with a 10 mm biopsy punch. A pre-load of 0.1 N was applied to the scaffolds, followed by compression at a constant displacement rate (0.5 mm/min) until 75% strain. The compressive elastic modulus (E) was calculated from the slope of the linear portion of the stress-strain curve (0 – 10% strain).

4.3.6.4. Shear Interface Analysis

Interfacial shear strength of a two-layer SSTAC and corresponding control scaffold was evaluated with a confined shear test. Specimens were punched to a diameter of 10 mm and cut to a height of 8 mm. In the case of SSTAC specimens, the interface between the two layers was located at the mid-point of the height (i.e. 4 mm of each layer per side of the interface). Specimens were evaluated in a custom confined shear set-up, wherein a lower arm remained stationary as an upper arm was displaced (**Figure A-22**). The upper and lower arms were fabricated from ¼ inch thick aluminum bars (McMaster Carr) cut to 5 in X 1 in. Each mount had a 10 mm diameter hole, with the upper arm's hole machined to a depth of 4 mm and the lower arm's cut through the bar. The arms were affixed in tension clamps on an Instron 5944. To ensure alignment of the hole in each arm,

a 10 mm diameter rod was placed between the holes and the arms were clamped together. Furthermore, to ensure vertical alignment, the arms were affixed to the tension clamps using a square and level. Insertion of the scaffold into the fixture was done while the holes in each arm were aligned. Scaffolds were pushed through the hole in the lower arm until it was up against the back of the hole in the upper arm (i.e. aligning the interface at the interface of the arms). A silicone spacer (10 mm diameter X 2.35 mm length) was then press fit into the lower arm to prevent movement of the scaffold. Once inserted, the upper arm was displaced at a rate of 2 mm/min – applying a shear strain to the interface of the scaffold – until failure.

4.3.6.5. Statistics

Data is reported as the mean ± standard deviation. Data set mean values were compared in GraphPad Prism via ANOVA followed by Tukey's posthoc test where *p*-value < 0.05 was considered statistically significant.

CHAPTER V

CONCLUSIONS

5.1. Conclusions

Achieving targeted tissue regeneration using a scaffold's native material properties alone is of interest in the modern era of tissue engineering. The precision with which synthetic material scaffolds can be tuned holds potential to provide a unique level of control to impact regenerative outcomes. Further, this avoids the use of exogenous growth factors and native protein-based systems, which have increased risk and decreased versatility. Particularly, these capabilities of 'materials-guided' approaches have potential to apply to complex and pervasive challenges, such as osteochondral defects, as described in Chapter I. With advancements to both the understanding and the tunability of such materials-guided approaches, there is increasing potential to address this complexity with precise material synthesis and scaffold spatial design. Previously, the Grunlan lab has been the first to report the osteoinductivity and bioactivity of a non-brittle siloxane polymer [star poly(dimethyl siloxane) methacrylate; $PDMS_{star}$-MA] when incorporated within a poly (ethylene glycol) diacrylate (PEG-DA) hydrogel. By utilizing a hydrophobic, inorganic macromer, rather than the frequently used brittle glasses or ceramics, a more tunable system can be achieved. Furthermore, our group has established the use of a fused salt template, in combination with solvent-induced phase separation, for the fabrication of interconnected, macroporous PEG-DA hydrogel scaffolds.

In this work, the Grunlan lab's PEG-DA SIPS/salt-templated fabrication and siloxane chemistry advancements were developed toward the treatment of osteochondral defects. Specifically, while previously fabricated PDMS$_{star}$-MA:PEG-DA hydrogels were determined bioactive and osteoinductive, their osteoconductivity (ability to support cell seeding and neotissue infiltration) was minimal, thus diminishing its capability as a materials-guided regenerative strategy. Herein, this technology was developed toward and osteoinductive and osteoconductive strategy, and further advanced in tunability toward achieving spatial control for osteochondral regeneration.

In Chapter II, PDMS$_{star}$-MA:PEG-DA hydrogels were fabricated with a fused salt template, in conjunction with SIPS employing a DCM precursor solution, creating interconnected macropores of tunable sizes to permit post-fabrication cell seeding and osteoconductivity. The resulting scaffolds were investigated for their efficacy as a bone regenerative strategy. Hydrogels were produced with two M_n's of PDMS$_{star}$-MA (2k and 7k) and varying wt/wt% ratios of PDMS$_{star}$-MA to PEG-DA ($M_n = 3.4k$). CLSM images revealed the improved distribution of the 2k PDMS$_{star}$-MA within the PEG matrix, attributed to its superior solubility in the DCM precursor solution. Pore size tunability and interconnectivity for osteoconductivity were confirmed by SEM imaging and a water wicking test. While absent for the PEG-DA control, bioactivity was confirmed for templated SIPS PDMS$_{star}$-PEG hydrogels (2k series) with HAp formation observed (via SEM and XRD) following soaking in SBF. Finally, all RGD-containing templated SIPS PDMS$_{star}$-PEG scaffolds were confirmed non-cytotoxic and showed PDMS dose-dependent increases in key indicators of osteogenesis. However, this was dependent on

comacromer M_n, wherein the better dispersed comacromer (lower M_n) showed statistical differences at lower concentrations. Von Kossa staining further revealed dose-dependent increases in calcium deposition by hBMSCs seeded on 2k-containing scaffolds. Overall, these templated SIPS PDMS$_{star}$-PEG hydrogels displayed the potential to serve as instructive scaffolds for bone regeneration without the inclusion of added growth factors or glass/ceramic fillers.

In Chapter III, the osteogenic potential of siloxane-containing PEG-DA hydrogel scaffolds were increased by leveraging an additional chemical functionality. Two new siloxane macromers were synthesized containing a relatively high (PPMS-DA) and low (PPMS-DA 25%) phosphonate pendant group concentration to enhance bone regenerative capacity. In this study, several mol% ratio PPMS:PEG scaffolds were fabricated, along with control scaffold compositions containing vinyl phosphonate (i.e. no siloxane) and PDMS-MA (i.e. no phosphonate) with PEG-DA. These scaffolds produced an increase in hydrophobicity versus the PEG scaffold control and an associated decrease in swelling. However, the average scaffold pore size was similar to the control scaffolds (~370 µm). Enhanced hydrophobicity and such a pore size are associated with osteogenesis. The enhanced bioactivity of phosphonated-siloxane based scaffolds was demonstrated by the formation of HAp just two weeks after exposure to SBF, faster than for the siloxane-based scaffold (four weeks). In *in vitro* culture with hBMSCs for 14 and 28 days, a scaffold prepared with PPMS-DA saw greatly increased mineralization while maintaining similar protein expression versus an analogous scaffold prepared with PDMS-MA. This suggests a potentially better osteogenic response. However, the concentration of phosphonated-

siloxane macromer (PPMS-DA) did not elicit "PPMS-dose dependent" increase in protein expression. In fact, BMP-2 expression was greatest for the lowest PPMS dosage, suggesting a more complex mechanism. Overall, when incorporated into PEG-DA hydrogel scaffolds, phosphonated-siloxane macromers exhibit enhanced osteoinductivity and bioactivity versus a siloxane macromer.

In Chapter IV, we designed a fabrication process that adds spatial control to the previously studied salt-templated hydrogel scaffolds. Hydrogel SSTACs, or scaffolds with spatially tunable arrangement and chemistry, achieved this through curing an additional PEG-DA network through non-salt leached SIPS/Salt scaffolds. SSTACs fabricated in various layered geometries with PPMS-DA:PEG-DA and 100% PEG-DA compositions showed the formation of 'soft' interfaces with defined chemistries. When subjected to shear force at the interface in a confined environment, SSTAC hydrogels broke at a similar force to a complete PEG-DA hydrogel, showing the integrity of the interface. Finally. a proof-of-concept osteochondral regenerative device was developed as a tri-layer scaffold to display the current capabilities with materials previously developed and the room for future expansion. By controlling the layer size, chemistry, and pore morphology through the SIPS/Salt fabrication technique, hydrogel SSTACs can be developed to address the complex spatial organization of osteochondral tissue.

5.2. Future Directions

This dissertation established the efficacy of materials-guided strategies for advancing osteochondral defect regeneration. Future work toward chondral and interface regeneration can further enhance the potential of the strategies developed herein.

110

Furthermore, SIPS/Salt hybrid hydrogels could be deployed as bone regenerative scaffolds in other hybrid techniques. Potential directions for expansion are detailed below and in **Figure 5-1**.

Figure 5-1. Future directions for materials-guided regeneration using templated PEG-DA hybrid hydrogels.

5.2.1. Osteochondral Defect Repair - Cartilage

The proof-of-concept osteochondral SSTAC design developed in Chapter IV displayed considerably limited regenerative potential for cartilage. Referring to the materials-guided regeneration of cartilage tissue discussed in Chapter I, the use of glycosaminoglycans, natively found in articular cartilage, is the primary way to induce chondrogenesis in materials-guided strategies. Methacrylated hyaluronic acid (HA-MA), which has been commonly used for cartilage regenerative hydrogels,[258] could be used to accomplish this. Due to the aqueous solubility of HA-MA and many other cartilage regenerative materials, it is likely that inclusion will require investigation of a different

solvent or solvent mixture for utilization in SIPS/Salt templating. Fabrication of an HA-MA-containing scaffold composition with a small pore size, using the proof-of-concept layer structure outlined in chapter IV could provide an effective device strategy. Such scaffolds should be analyzed for chondrogenic potential by *in vitro* evaluation for Sox 9 and Collagen II expression from hBMSC culture. Furthermore, inclusion of HA-MA could enhance the chondrogenic response at the osteochondral interface considerably, assisting in the formation of a calcified cartilage layer.

Another way to address the cartilage regenerative potential of SSTACs would be through morphological changes to the scaffold layers. As shown in **Figure 1-1**, there are three distinct zones in articular cartilage, each with different collagen alignments and cellularity, comprising a complex structure able to bear the load of the joint. Several strategies have attempted to mimic this structure.[259-262] A SSTAC that could leverage different porogens, such as fibrous meshes with designed orientations, could be a step toward enhancing their potency at the cartilage layer.

5.2.2. Osteochondral Defect Repair - Interface

Previously, our collaborators showed that conventional PDMS:PEG hydrogels modified with chondroitin sulfate, and the exogenous growth factors TGFβ-1 and BMP-2, were able to produce the desired response for osteochondral interface regeneration, differentiation of hypertrophic chondrocytes.[135] This is accomplished through a chondrogenic response in a mineralized environment. It is hypothesized that a purely materials-guided approach could achieve a similar outcome. Specifically, for chondrogenesis, the sulfonic acid group has been well indicated in chondrocytic

differentiation, due to its similarity to charged GAGs (e.g. chondroitin sulfate).[263-265] Further, as shown in Chapter II and III, siloxanes are bioactive and able to induce mineralization. Thus, by developing a sulfonated-siloxane a hypertrophic chondrocyte phenotype could be achieved. Two synthetic procedures are proposed for fabrication of such sulfonated siloxanes (**Figure 5-2**). First, a process similar to the synthesis of PPMS-DA in Chapter III is proposed. As seen in step three for 100% PPMS-DA, 'PTMS-OH' is available for addition of a vinyl-functionalized monomer via thiolene click addition. Thus, using a sodium sulfonate-containing monomer, a hypothesized synthetic procedure for a sulfonated-siloxane has been developed using PTMS-OH (**Figure 5-2A**). However, the considerable difference in solubility between the two reactants may require further investigation of the synthesis. Thus, if this method becomes difficult for fabrication of a sulfonated siloxane, a second potential mechanism using a hydrosilylation reaction is proposed (**Figure 5-2B**). Investigation through *in vitro* culture with hBMSCs revealing mineralization while simultaneously achieving higher expression of Collagen X and a higher osterix/Sox 9 ratio would yield a successful result.[135] Markers of osteogenesis should also be investigated as well, and if present the tuning of the ratio of siloxane to sulfonate could be used to potentially reduce this response.
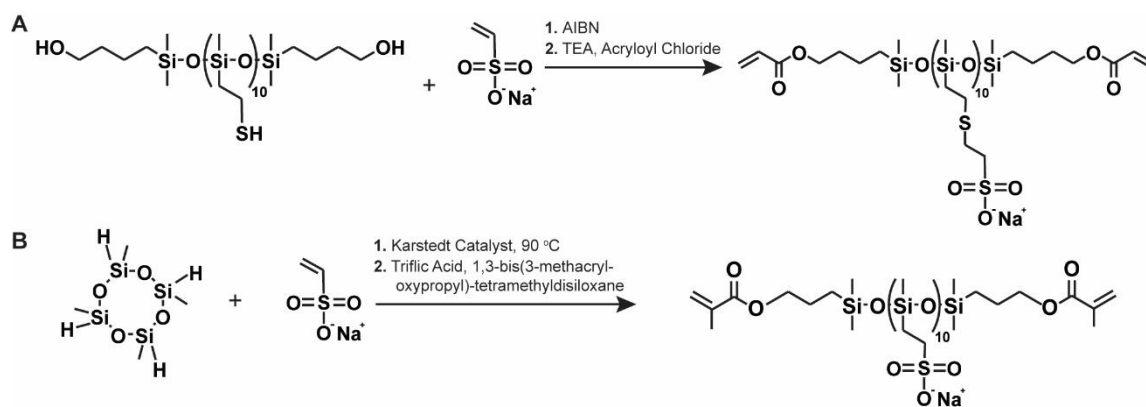
Figure 5-2. Proposed syntheses of sulfonated-siloxane macromers for osteochondral interface regeneration.

5.2.3. Cartilage-Capped Regenerative Osteochondral Plugs (CC-ROPs)

Due to the challenge of regenerating articular cartilage, partial resurfacing strategies, wherein a device is implanted to permanently replace damaged articular cartilage, have been developed for clinical treatment of osteochondral defects. A few of these strategies were discussed in Chapter I as synthetic material-based OCD repair in clinical trials. Our group has recently developed a double network hydrogel for synthetic cartilage that is uniquely able to simultaneously achieve high modulus, strength, and toughness while maintaining the hydration necessary for lubricity.[212] Through combination with the salt templated hydrogel scaffolds for bone regeneration discussed herein, it would be possible to develop a partial resurfacing strategy for OCD repair. Such bioprosthetic devices – cartilage-capped, regenerative osteochondral plugs (CC-ROPs) – would be cylindrical, autograft-sized implants with a biodegradable, bone-regenerative base and a permanent, resurfacing cartilage 'cap.' Similar to grafting strategies, CC-ROPs could be implanted after defect debridement. The scaffold base would regenerate new,

114

healthy bone tissue to subsequently integrate and lock in place the permanent 'cap' of the CC-ROP that would permanently replace the damaged cartilage with a mechanically robust synthetic hydrogel. Thus, both damaged tissues would be suitably replaced.

REFERENCES

1.   Buckwalter, J. A., Articular cartilage: injuries and potential for healing. *J. Orthop. Sports Phys. Ther.* **1998,** *28*, 192-202.

2.   Ambra, L. F.; de Girolamo, L.; Mosier, B.; Gomoll, A. H., Review: interventions for cartilage disease: current state-of-the-art and emerging technologies. *Arthritis Rheumatol.* **2017,** *69*, 1363-1373.

3.   Bruns, J.; Werner, M.; Habermann, C., Osteochondritis Dissecans: Etiology, Pathology, and Imaging with a Special Focus on the Knee Joint. *Cartilage* **2017,** *9*, 346 - 362.

4.   Ytrehus, B.;   Carlson, C. S.; Ekman, S., Etiology and Pathogenesis of Osteochondrosis. *Vet. Pathol.* **2007,** *44*, 429-448.

5.   Sophia Fox, A. J.; Bedi, A.; Rodeo, S. A., The Basic Science of Articular Cartilage: Structure, Composition, and Function. *Sports Health* **2009,** *1*, 461-468.

6.   Lefkoe, T. P.; Trafton, P. G.; Ehrlich, M. G.; Walsh, W. R.; Dennehy, D. T.; Barrach, H.-J.; Akelman, E., An Experimental Model of Femoral Condylar Defect Leading to Osteoarthrosis. *J. Orthop. Trauma* **1993,** *7*, 458-467.

7.   Sellards, R. A.; Nho, S. J.; Cole, B. J., Chondral injuries. *Curr. Opin. Rheumatol.* **2002,** *14*, 134-141.

8.   Gomoll, A. H.; Madry, H.; Knutsen, G.; van Dijk, N.; Seil, R.; Brittberg, M.; Kon, E., The subchondral bone in articular cartilage repair: current problems in the surgical management. *Knee Surg. Sports Traumatol. Arthrosc.* **2010,** *18*, 434-447.

9.   Armiento, A. R.; Stoddart, M. J.; Alini, M.; Eglin, D., Biomaterials for Articular Cartilage Tissue Engineering: Learning from Biology. *Acta Biomater.* **2018,** *65*, 1-20.

10.   Gomoll, A. H.; Farr, J.; Gillogly, S. D.; Kercher, J. S.; Minas, T., Surgical management of articular cartilage defects of the knee. *Instr. Course Lect.* **2011,** *60*, 461-83.

11.   Camp, C. L.; Stuart, M. J.; Krych, A. J., Current concepts of articular cartilage restoration techniques in the knee. *Sports Health* **2014,** *6*, 265-73.

12.   Hangody, L.; Fules, P., Autologous osteochondral mosaicplasty for the treatment of full-thickness defects of weight-bearing joints: ten years of experimental and clinical experience. *J. Bone Joint Surg.* **2003,** *85-A Suppl 2*, 25-32.

13. Demange, M.; Gomoll, A. H., The use of osteochondral allografts in the management of cartilage defects. *Curr. Rev. Musculoskelet. Med.* **2012,** *5*, 229-235.

14. Ansari, S.; Khorshidi, S.; Karkhaneh, A., Engineering of Gradient Osteochondral Tissue: From Nature to Lab. *Acta Biomater.* **2019,** *87*, 41-54.

15. Nukavarapu, S. P.; Dorcemus, D. L., Osteochondral tissue engineering: Current strategies and challenges. *Biotechnol. Adv.* **2013,** *31*, 706-721.

16. Hutmacher, D. W., Scaffolds in tissue engineering bone and cartilage. *Biomaterials* **2000,** *21*, 2529-2543.

17. Park, K. M.; Shin, Y. M.; Kim, K.; Shin, H., Tissue Engineering and Regenerative Medicine 2017: A Year in Review. *Tissue Eng. Part B Rev.* **2018,** *24*, 327-344.

18. Caplan, A. I., Adult mesenchymal stem cells for tissue engineering versus regenerative medicine. *J. Cell. Physiol.* **2007,** *213*, 341-347.

19. Rosenbaum, A. J.; Grande, D. A.; Dines, J. S., The use of mesenchymal stem cells in tissue engineering: A global assessment. *Organogenesis* **2008,** *4*, 23-27.

20. Deng, C.; Chang, J.; Wu, C., Bioactive scaffolds for osteochondral regeneration. *J. Orthop. Translat.* **2019,** *17*, 15-25.

21. Di Luca, A.; Van Blitterswijk, C.; Moroni, L., The osteochondral interface as a gradient tissue: from development to the fabrication of gradient scaffolds for regenerative medicine. *Birth Defects Res., Part C* **2015,** *105*, 34-52.

22. Yan, L.-P.; Oliveira, J. M.; Oliveira, A. L.; Reis, R. L., Current Concepts and Challenges in Osteochondral Tissue Engineering and Regenerative Medicine. *ACS Biomater. Sci. Eng.* **2015,** *1*, 183-200.

23. Babensee, J. E.; McIntire, L. V.; Mikos, A. G., Growth Factor Delivery for Tissue Engineering. *Pharm. Res.* **2000,** *17*, 497-504.

24. Ikada, Y., Challenges in tissue engineering. *J. R. Soc., Interface* **2006,** *3*, 589-601.

25. Dutta, R. C.; Dutta, A. K., Cell-interactive 3D-scaffold; advances and applications. *Biotechnol. Adv.* **2009,** *27*, 334-339.

26. Kleinman, H. K.; Philp, D.; Hoffman, M. P., Role of the extracellular matrix in morphogenesis. *Curr. Opin. Biotechnol.* **2003,** *14*, 526-532.

27. Lutolf, M. P.; Hubbell, J. A., Synthetic biomaterials as instructive extracellular microenvironments for morphogenesis in tissue engineering. *Nat. Biotechnol.* **2005,** *23*, 4315-4323.

28.   Brandl, F.; Sommer, F.; Goepferich, A., Rational design of hydrogels for tissue engineering: Impact of physical factors on cell behavior. *Biomaterials* **2007,** *28*, 134-6.

29.   Pennesi, C.; Scaglione, S.; Gionnoni, P.; Quarto, R., Regulatory influence of scaffolds on cell behavior: How cells decode biomaterials. *Curr. Pharm. Biotechnol.* **2011,** *12*, 151-159.

30.   Nichol, J. W.; Khademhosseini, A., Modular tissue engineering: Engineering biological tissues from the bottom up. *Soft Matter* **2009,** *5*, 1312.

31.   Khetan, S.; Burdick, J. A., Patterning hydrogels in three dimensions towards controlling cellular interactions. *Soft Matter* **2011,** *5*, 830-838.

32.   Woodfield, T. B. F.; Moroni, L.; Malda, J., Combinatorial approaches to controlling cell behaviour and tissue formation via rapid-prototyping and smart scaffold design. *Comb. Chem. High Throughput Screening* **2009,** *12*, 562-579.

33.   Khademhosseini, A.; Langer, R., Microengineered hydrogels for tissue engineering. *Biomaterials* **2007,** *28*, 5087.

34.   McGlohorn, J. B.; Holder, J.; Grimes, L. W.; Thomas, C. B.; Burg, K. J. L., Evaluation of smooth muscle cell response using two types of porous polylactide scaffolds with differing pore topography. *Tissue Eng.* **2004,** *10*, 505-514.

35.   Discher, D. E.; Janmey, P.; Wang, Y.-l., Tissue cells feel and respond to the stiffness of their substrate. *Science* **2005,** *310*, 1139-1143.

36.   Engler, A. J.; Sen, S.; Sweeney, H. L.; Discher, D. E., Matrix elasticity directs stem cell lineage specification. *Cell* **2006,** *126*, 677-689.

37.   Liao, H.; Munoz-Pinto, D.; Qu, X.; Hou, Y.; Grunlan, M. A.; Hahn, M. S., Influence of hydrogel mechanical properties and mesh size on vocal fold fibroblast extracellular matrix production and phenotype. *Acta Biomater.* **2008,** *4*, 1161-1171.

38.   Dado, D.; Levenberg, S., Cell-scaffold mechanical interplay within engineered tissues. *Semin. Cell Dev. Biol.* **2009,** *20*, 656-664.

39.   Lin, S.; Sangaj, N.; Razafiarison, T.; Zhang, C.; Varghese, S., Influence of physical properties of biomaterials on cellular behavior. *Pharm. Res.* **2011,** *28*, 1422-1430.

40.   Benoit, D. S. W.; Schwartz, M. P.; Durney, A. R.; Anseth, K. S., Small functional groups for controlled differentiation of hydrogel-encapsulated human mesenchymal stem cells. *Nat. Mater.* **2008,** *7*, 816-823.

41.   Escobar-Ivirico, J. L.; Salmeron-Sanchez, M.; Gomez-Ribelles, J. L.; Monleon-Pradas, M.; Soria, J. M.; Gomes, M. E.; Reis, R. L.; Mano, J. F., Proliferation and differentiation of goat bone marrow stromal cells in 3D scaffolds with tunable hydrophilicity. *J. Biomed. Mater. Res. B* **2009,** *91B*, 277-286.

42.   Song, J. H.; Yoon, B. H.; Kim, H. E.; Kim, H. W., Bioactive and degradable hybridized nanofibers of gelatin-siloxane for bone regeneration. *J. Biomed. Mater. Res. A* **2008,** *84*, 875-84.

43.   Ning, C. Q.; Mehta, J.; El-Ghannam, A., Effect of silica on the bioactivity of calcium phosphate composites *in vitro*. *J. Mater. Sci. Mater. Med.* **2005,** *16*, 355-360.

44.   Ayala, R.; Zhang, C.; Yang, D.; Hwang, Y.; Aung, A.; Shroff, S. S.; Arce, F. T.; Lal, R.; Arya, G.; Varghese, S., Engineering the cell-material interface for controlling stem cell adhesion, migration, and differentiation. *Biomaterials* **2011,** *32*, 3700-3711.

45.   Jansen, E. J.; Sladek, R. E.; Bahar, H.; Yaffe, A.; Gijbels, M. J.; Kuijer, R.; Bulstra, S. K.; Guldemond, N. A.; Binderman, I.; Koole, L. H., Hydrophobicity as a design criterion for polymer scaffolds in bone tissue engineering. *Biomaterials* **2005,** *26*, 4423-31.

46.   Fisher, J. P.; Lalani, Z.; Bossano, C. M.; Brey, E. M.; Demian, N.; Johnston, C. M.; Dean, D.; Jansen, J. A.; Wong, M. E.; Mikos, A. G., Effect of biomaterial properties on bone healing in a rabbit tooth extration socket model. *J. Biomed. Mater. Res. A* **2004,** *68*, 428-438.

47.   Anseth, K. S.; Bowman, C. N.; Brannon-Peppas, L., Mechanical properties of hydrogels and their experimental determination. *Biomaterials* **1996,** *17*, 1647-1657.

48.   Drury, J. L.; Mooney, D. G., Hydrogels for tissue engineering: Scaffold design variables and applications. *Biomaterials* **2003,** *24*, 4337-4351.

49.   Park, H.; Guo, X.; Temenoff, J. S.; Tabata, Y.; Caplan, A. I.; Kurtis Kasper, F.; Mikos, A. G., Effect of swelling ratio of injectable hydrogel composites on chondrogenic differentiation of encapsulated rabbit marrow mesenchymal stem cells in vitro. *Biomacromolecules* **2009,** *10*, 541-546.

50.   Pan, Z.; Duan, P.; Liu, X.; Wang, H.; Cao, L.; He, Y.; Dong, J.; Ding, J., Effect of porosities of bilayered porous scaffolds on spontaneous osteochondral repair in cartilage tissue engineering. *Regener. Biomater.* **2015,** *2*, 9-19.

51.   Dhandayuthapani, B.; Yoshida, Y.; Maekawa, T.; Kumar, D. S., Polymeric Scaffolds in Tissue Engineering Application: A Review. *Int. J. Polym. Sci.* **2011,** *2011*, 290602.

52.   Bongio, M.; van den Beucken, J. J. J. P.; Leeuwenburgh, S. C. G.; Jansen, J. A., Development of bone substitute materials: from 'biocompatible' to 'instructive'. *J. Mater. Chem.* **2010,** *20*, 8747-8759.

53.   Hunziker, E. B.; Quinn, T. M.; Häuselmann, H. J., Quantitative structural organization of normal adult human articular cartilage. *Osteoarthritis Cartilage* **2002,** *10*, 564-572.

54.   Lyons, T. J.; Stoddart, R. W.; McClure, S. F.; McClure, J., The tidemark of the chondro-osseous junction of the normal human knee joint. *J. Mol. Histol.* **2005,** *36*, 207-215.

55.   Lepage, S. I. M.; Robson, N.; Gilmore, H.; Davis, O.; Hooper, A.; St. John, S.; Kamesan, V.; Gelis, P.; Carvajal, D.; Hurtig, M.; Koch, T. G., Beyond Cartilage Repair: The Role of the Osteochondral Unit in Joint Health and Disease. *Tissue Eng. Part B Rev.* **2019,** *25*, 114-125.

56.   Woodruff, M. A.; Lange, C.; Reichert, J.; Berner, A.; Chen, F.; Fratzl, P.; Schantz, J.-T.; Hutmacher, D. W., Bone tissue engineering: from bench to bedside. *Mater. Today* **2012,** *15*, 430-435.

57.   Means, A. K.; Grunlan, M. A., Modern Strategies To Achieve Tissue-Mimetic, Mechanically Robust Hydrogels. *ACS Macro Lett.* **2019,** *8*, 705-713.

58.   Madry, H.; Orth, P.; Cucchiarini, M., Role of the Subchondral Bone in Articular Cartilage Degeneration and Repair. *J. Am. Acad. Orthop. Surg.* **2016,** *24*, e45-6.

59.   Jeon, J. E.; Vaquette, C.; Klein, T. J.; Hutmacher, D. W., Perspectives in Multiphasic Osteochondral Tissue Engineering. *The Anatomical Record* **2014,** *297*, 26-35.

60.   Schek, R. M.; Taboas, J. M.; Segvich, S. J.; Hollister, S. J.; Krebsbach, P. H., Engineered osteochondral grafts using biphasic composite solid free-form fabricated scaffolds. *Tissue Eng.* **2004,** *10*, 1376-85.

61.   Oliveira, J. M.; Rodrigues, M. T.; Silva, S. S.; Malafaya, P. B.; Gomes, M. E.; Viegas, C. A.; Dias, I. R.; Azevedo, J. T.; Mano, J. F.; Reis, R. L., Novel hydroxyapatite/chitosan bilayered scaffold for osteochondral tissue-engineering applications: Scaffold design and its performance when seeded with goat bone marrow stromal cells. *Biomaterials* **2006,** *27*, 6123-6137.

62.   Nooeaid, P.; Salih, V.; Beier, J. P.; Boccaccini, A. R., Osteochondral tissue engineering: scaffolds, stem cells and applications. *J. Cell. Mol. Med.* **2012,** *16*, 2247-2270.

63.   Longley, R.; Ferreira, A. M.; Gentile, P., Recent Approaches to the Manufacturing of Biomimetic Multi-Phasic Scaffolds for Osteochondral Regeneration. *Int. J. Mol. Sci.* **2018,** *19*.

64.   Hacker, M. C.; Mikos, A. G., Synthetic Polymers. In *Principles of Regenerative Medicine*, 2nd ed.; Academic Press: San Diego, 2011; pp 587-622.

65.   Sheikh, Z.; Najeeb, S.; Khurshid, Z.; Verma, V.; Rashid, H.; Glogauer, M., Biodegradable Materials for Bone Repair and Tissue Engineering Applications. *Materials (Basel, Switzerland)* **2015,** *8*, 5744-5794.

66.   Du, Y.; Guo, J. L.; Wang, J.; Mikos, A. G.; Zhang, S., Hierarchically designed bone scaffolds: from internal cues to external stimuli. *Biomaterials* **2019**, 119334.

67.   Yu, X.; Tang, X.; Gohil, S. V.; Laurencin, C. T., Biomaterials for bone regenerative engineering. *Adv. Healthcare Mater.* **2015,** *4*, 1268-1285.

68.   Stevens, M. M., Biomaterials for bone tissue engineering. *Mater. Today* **2008,** *11*, 18-25.

69.   Albrektsson, T.; Johansson, C., Osteoinduction, osteoconduction and osseointegration. *Eur. Spine J.* **2001,** *10*, S96-S101.

70.   LeGeros, R. Z., Calcium Phosphate-Based Osteoinductive Materials. *Chem. Rev.* **2008,** *108*, 4742-4753.

71.   Tang, Z.; Li, X.; Tan, Y.; Fan, H.; Zhang, X., The material and biological characteristics of osteoinductive calcium phosphate ceramics. *Regener. Biomater.* **2018,** *5*, 43-59.

72.   Kretlow, J. D.; Mikos, A. G., Review: Mineralization of Synthetic Polymer Scaffolds for Bone Tissue Engineering. *Tissue Eng.* **2007,** *13*, 927-938.

73.   Di Luca, A.; Ostrowska, B.; Lorenzo-Moldero, I.; Lepedda, A.; Swieszkowski, W.; Van Blitterswijk, C.; Moroni, L., Gradients in pore size enhance the osteogenic differentiation of human mesenchymal stromal cells in three-dimensional scaffolds. *Sci. Rep.* **2016,** *6*, 22898.

74.   Roseti, L.; Parisi, V.; Petretta, M.; Cavallo, C.; Desando, G.; Bartolotti, I.; Grigolo, B., Scaffolds for bone tissue engineering: state of the art and new perspectives. *Mater. Sci. Eng. C* **2017,** *78*, 1246-1262.

75.   Weber, F. E., Reconsidering Osteoconduction in the Era of Additive Manufacturing. *Tissue Eng. Part B Rev.* **2019,** *25*, 375-386.

76.   Habibovic, P.; Sees, T. M.; van den Doel, M. A.; van Blitterswijk, C. A.; de Groot, K., Osteoinduction by biomaterials—Physicochemical and structural influences. *J. Biomed. Mater. Res. A* **2006,** *77A*, 747-762.

77.   Harburger, D. S.; Calderwood, D. A., Integrin signalling at a glance. *J. Cell Sci.* **2009,** *122*, 159.

78.   Maia, F. R.; Bidarra, S. J.; Granja, P. L.; Barrias, C. C., Functionalization of biomaterials with small osteoinductive moieties. *Acta Biomater.* **2013,** *9*, 8773-8789.

79.   Habibovic, P.; de Groot, K., Osteoinductive biomaterials—properties and relevance in bone repair. *J. Tissue Eng. Regen. Med.* **2007,** *1*, 25-32.

80.   Breitwieser, G. E., Extracellular calcium as an integrator of tissue function. *The International Journal of Biochemistry & Cell Biology* **2008,** *40*, 1467-1480.

81.   Barradas, A. M. C.; Fernandes, H. A. M.; Groen, N.; Chai, Y. C.; Schrooten, J.; van de Peppel, J.; van Leeuwen, J. P. T. M.; van Blitterswijk, C. A.; de Boer, J., A calcium-induced signaling cascade leading to osteogenic differentiation of human bone marrow-derived mesenchymal stromal cells. *Biomaterials* **2012,** *33*, 3205-3215.

82.   Chai, Y. C.; Carlier, A.; Bolander, J.; Roberts, S. J.; Geris, L.; Schrooten, J.; Van Oosterwyck, H.; Luyten, F. P., Current views on calcium phosphate osteogenicity and the translation into effective bone regeneration strategies. *Acta Biomater.* **2012,** *8*, 3876-3887.

83.   Aquino-Martínez, R.;   Monroe, D. G.; Ventura, F., Calcium mimics the chemotactic effect of conditioned media and is an effective inducer of bone regeneration. *PLoS One* **2019,** *14*, e0210301.

84.   Malhotra, A.; Habibovic, P., Calcium Phosphates and Angiogenesis: Implications and Advances for Bone Regeneration. *Trends Biotechnol.* **2016,** *34*, 983-992.

85.   Dinarvand, P.;   Seyedjafari, E.;   Shafiee, A.;   Babaei Jandaghi, A.; Doostmohammadi, A.; Fathi, M. H.; Farhadian, S.; Soleimani, M., New Approach to Bone Tissue Engineering: Simultaneous Application of Hydroxyapatite and Bioactive Glass Coated on a Poly(l-lactic acid) Scaffold. *ACS Applied Materials & Interfaces* **2011,** *3*, 4518-4524.

86.   Rezwan, K.; Chen, Q. Z.; Blaker, J. J.; Boccaccini, A. R., Biodegradable and bioactive porous polymer/inorganic composite scaffolds for bone tissue engineering. *Biomaterials* **2006,** *27*, 3413-3431.

87.   Wang, W.; Yeung, K. W. K., Bone grafts and biomaterials substitutes for bone defect repair: A review. *Bioactive Materials* **2017,** *2*, 224-247.

88.	Munoz-Pinto, D. J.; Jimenez-Vergara, A. C.; Hou, Y.; Hayenga, H. N.; Rivas, A.; Grunlan, M.; Hahn, M. S., Osteogenic potential of poly(ethylene glycol)-poly(dimethylsiloxane) hybrid hydrogels. *Tissue Eng.* **2012,** *18*, 1710-9.

89.	Frassica, M. T.; Jones, S. K.; Diaz-Rodriguez, P.; Hahn, M. S.; Grunlan, M. A., Incorporation of a silicon-based polymer to PEG-DA templated hydrogel scaffolds for bioactivity and osteoinductivity. *Acta Biomater.* **2019,** *99*, 100-109.

90.	Kerativitayanan, P.; Gaharwar, A. K., Elastomeric and mechanically stiff nanocomposites from poly(glycerol sebacate) and bioactive nanosilicates. *Acta Biomater.* **2015,** *26*, 34-44.

91.	Carrow, J. K.; Di Luca, A.; Dolatshahi-Pirouz, A.; Moroni, L.; Gaharwar, A. K., 3D-printed bioactive scaffolds from nanosilicates and PEOT/PBT for bone tissue engineering. *Regener. Biomater.* **2018,** *6*, 29-37.

92.	Zhang, X.; Zeng, D.; Li, N.; Wen, J.; Jiang, X.; Liu, C.; Li, Y., Functionalized mesoporous bioactive glass scaffolds for enhanced bone tissue regeneration. *Sci. Rep.* **2016,** *6*, 19361.

93.	Zhang, K.; Fan, Y.; Dunne, N.; Li, X., Effect of microporosity on scaffolds for bone tissue engineering. *Regener. Biomater.* **2018,** *5*, 115-124.

94.	Samavedi, S.; Whittington, A. R.; Goldstein, A. S., Calcium phosphate ceramics in bone tissue engineering: A review of properties and their influence on cell behavior. *Acta Biomater.* **2013,** *9*, 8037-8045.

95.	Breuls, R. G. M.; Jiya, T. U.; Smit, T. H., Scaffold stiffness influences cell behavior: opportunities for skeletal tissue engineering. *The open orthopaedics journal* **2008,** *2*, 103-109.

96.	Discher, D. E.; Mooney, D. J.; Zandstra, P. W., Growth factors, matrices, and forces combine and control stem cells. *Science* **2009,** *324*, 1673-1677.

97.	Huebsch, N.; Arany, P. R.; Mao, A. S.; Shvartsman, D.; Ali, O. A.; Bencherif, S. A.; Rivera-Feliciano, J.; Mooney, D. J., Harnessing traction-mediated manipulation of the cell/matrix interface to control stem-cell fate. *Nat. Mater.* **2010,** *9*, 518.

98.	Chatterjee, K.; Lin-Gibson, S.; Wallace, W. E.; Parekh, S. H.; Lee, Y. J.; Cicerone, M. T.; Young, M. F.; Simon, C. G., The effect of 3D hydrogel scaffold modulus on osteoblast differentiation and mineralization revealed by combinatorial screening. *Biomaterials* **2010,** *31*, 5051-5062.

99.   Turnbull, G.; Clarke, J.; Picard, F.; Riches, P.; Jia, L.; Han, F.; Li, B.; Shu, W., 3D bioactive composite scaffolds for bone tissue engineering. *Bioactive Materials* **2018,** *3*, 278-314.

100.   Velasco, M. A.; Narváez-Tovar, C. A.; Garzón-Alvarado, D. A., Design, materials, and mechanobiology of biodegradable scaffolds for bone tissue engineering. *BioMed Res. Int.* **2015,** *2015*, 729076-729076.

101.   Amini, A. R.; Laurencin, C. T.; Nukavarapu, S. P., Bone tissue engineering: recent advances and challenges. *Crit. Rev. Biomed. Eng.* **2012,** *40*, 363-408.

102.   Seo, S.-J.; Mahapatra, C.; Singh, R. K.; Knowles, J. C.; Kim, H.-W., Strategies for osteochondral repair: Focus on scaffolds. *J. Tissue Eng.* **2014,** *5*, 2041731414541850.

103.   Fu, Q.; Saiz, E.; Rahaman, M. N.; Tomsia, A. P., Bioactive glass scaffolds for bone tissue engineering: state of the art and future perspectives. *Mater. Sci. Eng. C* **2011,** *31*, 1245-1256.

104.   Bianco, A.; Cacciotti, I.; Lombardi, M.; Montanaro, L.; Bemporad, E.; Sebastiani, M., F-substituted hydroxyapatite nanopowders: Thermal stability, sintering behaviour and mechanical properties. *Ceram. Int.* **2010,** *36*, 313-322.

105.   Dorozhkin, S. V., Calcium Orthophosphates in Nature, Biology and Medicine. *Materials* **2009,** *2*, 399-498.

106.   Velard, F.; Laurent-Maquin, D.; Braux, J.; Guillaume, C.; Bouthors, S.; Jallot, E.; Nedelec, J.-M.; Belaaouaj, A.; Laquerriere, P., The effect of zinc on hydroxyapatite-mediated activation of human polymorphonuclear neutrophils and bone implant-associated acute inflammation. *Biomaterials* **2010,** *31*, 2001-2009.

107.   Honda, M.; Kikushima, K.; Kawanobe, Y.; Konishi, T.; Mizumoto, M.; Aizawa, M., Enhanced early osteogenic differentiation by silicon-substituted hydroxyapatite ceramics fabricated via ultrasonic spray pyrolysis route. *J. Mater. Sci. Mater. Med.* **2012,** *23*, 2923-2932.

108.   Kim, E.-J.; Bu, S.-Y.; Sung, M.-K.; Choi, M.-K., Effects of Silicon on Osteoblast Activity and Bone Mineralization of MC3T3-E1 Cells. *Biol. Trace Elem. Res.* **2013,** *152*, 105-112.

109.   Beck, G. R.; Ha, S.-W.; Camalier, C. E.; Yamaguchi, M.; Li, Y.; Lee, J.-K.; Weitzmann, M. N., Bioactive silica based nanoparticles stimulate bone forming osteoblasts, suppress bone esorbing osteoclasts, and enhance bone mineral density in vivo. *Nanomedicine* **2012,** *8*, 793-803.

110.   Becerra, J.; Andrades, J. A.; Guerado, E.; Zamora-Navas, P.; López-Puertas, J. M.; Reddi, A. H., Articular Cartilage: Structure and Regeneration. *Tissue Eng. Part B Rev.* **2010,** *16*, 617-627.

111.   Walter, S. G.; Ossendorff, R.; Schildberg, F. A., Articular cartilage regeneration and tissue engineering models: a systematic review. *Arch. Orthop. Trauma Surg.* **2019,** *139*, 305-316.

112.   Burris, D. L.; Ramsey, L.; Graham, B. T.; Price, C.; Moore, A. C., How Sliding and Hydrodynamics Contribute to Articular Cartilage Fluid and Lubrication Recovery. *TriL* **2019,** *67*, 46.

113.   Bružauskaitė, I.; Bironaitė, D.; Bagdonas, E.; Bernotienė, E., Scaffolds and cells for tissue regeneration: different scaffold pore sizes—different cell effects. *Cytotechnology* **2016,** *68*, 355-369.

114.   Nava, M. M.; Draghi, L.; Giordano, C.; Pietrabissa, R., The effect of scaffold pore size in cartilage tissue engineering. *J. Appl. Biomater. Funct. Mater.* **2016,** *14*, e223-e229.

115.   Gao, L.; McBeath, R.; Chen, C. S., Stem Cell Shape Regulates a Chondrogenic Versus Myogenic Fate Through Rac1 and N-Cadherin. *Stem Cells* **2010,** *28*, 564-572.

116.   Panadero, J. A.; Lanceros-Mendez, S.; Ribelles, J. L. G., Differentiation of mesenchymal stem cells for cartilage tissue engineering: Individual and synergetic effects of three-dimensional environment and mechanical loading. *Acta Biomater.* **2016,** *33*, 1-12.

117.   Muhammad, H.; Rais, Y.; Miosge, N.; Ornan, E. M., The primary cilium as a dual sensor of mechanochemical signals in chondrocytes. *Cell. Mol. Life Sci.* **2012,** *69*, 2101-2107.

118.   Uzieliene, I.; Bernotas, P.; Mobasheri, A.; Bernotiene, E., The Role of Physical Stimuli on Calcium Channels in Chondrogenic Differentiation of Mesenchymal Stem Cells. *Int. J. Mol. Sci.* **2018,** *19*, 2998.

119.   Huey, D. J.; Hu, J. C.; Athanasiou, K. A., Unlike Bone, Cartilage Regeneration Remains Elusive. *Science* **2012,** *338*, 917.

120.   Mehdizadeh, M.; Yang, J., Design Strategies and Applications of Tissue Bioadhesives. *Macromol. Biosci.* **2013,** *13*, 271-288.

121.   Yoo, H. S.; Lee, E. A.; Yoon, J. J.; Park, T. G., Hyaluronic acid modified biodegradable scaffolds for cartilage tissue engineering. *Biomaterials* **2005,** *26*, 1925-1933.

122.   Wang, D.-A.; Varghese, S.; Sharma, B.; Strehin, I.; Fermanian, S.; Gorham, J.; Fairbrother, D. H.; Cascio, B.; Elisseeff, J. H., Multifunctional chondroitin sulphate for cartilage tissue–biomaterial integration. *Nat. Mater.* **2007,** *6*, 385.

123.   Wu, S.-C.; Chen, C.-H.; Chang, J.-K.; Fu, Y.-C.; Wang, C.-K.; Eswaramoorthy, R.; Lin, Y.-S.; Wang, Y.-H.; Lin, S.-Y.; Wang, G.-J.; Ho, M.-L., Hyaluronan initiates chondrogenesis mainly via CD44 in human adipose-derived stem cells. *J. Appl. Physiol.* **2013,** *114*, 1610-1618.

124.   Ruffell, B.; Poon, G. F. T.; Lee, S. S. M.; Brown, K. L.; Tjew, S.-L.; Cooper, J.; Johnson, P., Differential Use of Chondroitin Sulfate to Regulate Hyaluronan Binding by Receptor CD44 in Inflammatory and Interleukin 4-activated Macrophages. **2011,** *286*, 19179-19190.

125.   Kazemnejad, S.; Khanmohammadi, M.; Baheiraei, N.; Arasteh, S., Current State of Cartilage Tissue Engineering using Nanofibrous Scaffolds and Stem Cells. *Avicenna J. Med. Biotechnol.* **2017,** *9*, 50-65.

126.   Fell, N. L. A.; Lawless, B. M.; Cox, S. C.; Cooke, M. E.; Eisenstein, N. M.; Shepherd, D. E. T.; Espino, D. M., The role of subchondral bone, and its histomorphology, on the dynamic viscoelasticity of cartilage, bone and osteochondral cores. *Osteoarthritis Cartilage* **2019,** *27*, 535-543.

127.   Stewart, H. L.; Kawcak, C. E., The Importance of Subchondral Bone in the Pathophysiology of Osteoarthritis. *Frontiers in Veterinary Science* **2018,** *5*, 178.

128.   Yousefi, A.-M.; Hoque, M. E.; Prasad, R. G. S. V.; Uth, N., Current strategies in multiphasic scaffold design for osteochondral tissue engineering: A review. *J. Biomed. Mater. Res. A* **2015,** *103*, 2460-2481.

129.   Xiao, H.; Huang, W.; Xiong, K.; Ruan, S.; Yuan, C.; Mo, G.; Tian, R.; Zhou, S.; She, R.; Ye, P.; Liu, B.; Deng, J., Osteochondral repair using scaffolds with gradient pore sizes constructed with silk fibroin, chitosan, and nano-hydroxyapatite. *Int. J. Nanomed.* **2019,** *14*, 2011-2027.

130.   Hu, J.; Feng, K.; Liu, X.; Ma, P. X., Chondrogenic and osteogenic differentiations of human bone marrow-derived mesenchymal stem cells on a nanofibrous scaffold with designed pore network. *Biomaterials* **2009,** *30*, 5061-5067.

131.   Murphy, C. M.; Haugh, M. G.; O'Brien, F. J., The effect of mean pore size on cell attachment, proliferation and migration in collagen–glycosaminoglycan scaffolds for bone tissue engineering. *Biomaterials* **2010,** *31*, 461-466.

132.   Oh, S. H.; Kim, T. H.; Im, G. I.; Lee, J. H., Investigation of Pore Size Effect on Chondrogenic Differentiation of Adipose Stem Cells Using a Pore Size Gradient Scaffold. *Biomacromolecules* **2010,** *11*, 1948-1955.

133.   Engler, A. J.; Tse, J. R., Stiffness gradients mimicking *in vivo* tissue variation regulate mesenchymal stem cell fate. *PLoS One* **2011,** *6*, e15978.

134.   Chen, K.; Shi, P.; Teh, T. K. H.; Toh, S. L.; Goh, J. C. H., In vitro generation of a multilayered osteochondral construct with an osteochondral interface using rabbit bone marrow stromal cells and a silk peptide-based scaffold. *J. Tissue Eng. Regen. Med.* **2016,** *10*, 284-293.

135.   Diaz-Rodriguez, P.; Erndt-Marino, J. D.; Gharat, T.; Munoz Pinto, D. J.; Samavedi, S.; Bearden, R.; Grunlan, M. A.; Saunders, W. B.; Hahn, M. S., Toward zonally tailored scaffolds for osteochondral differentiation of synovial mesenchymal stem cells. *J. Biomed. Mater. Res. B* **2019,** *107*, 2019-2029.

136.   Khanarian, N. T.; Haney, N. M.; Burga, R. A.; Lu, H. H., A functional agarose-hydroxyapatite scaffold for osteochondral interface regeneration. *Biomaterials* **2012,** *33*, 5247-5258.

137.   Lee, W. D.; Gawri, R.; Pilliar, R. M.; Stanford, W. L.; Kandel, R. A., Sol gel-derived hydroxyapatite films over porous calcium polyphosphate substrates for improved tissue engineering of osteochondral-like constructs. *Acta Biomater.* **2017,** *62*, 352-361.

138.   Komuro, H.; Wint, W. Y.; Horiuchi, N.; Nozaki, K.; Sasano, T.; Miyashin, M.; Yamashita, K.; Nagai, A., An oriented hydroxyapatite film with arrayed plate-like particles enhance chondrogenic differentiation of ATDC5 cells. *J. Biomed. Mater. Res. A* **2019,** *n/a*.

139.   Yang, J.; Liu, Y.; He, L.; Wang, Q.; Wang, L.; Yuan, T.; Xiao, Y.; Fan, Y.; Zhang, X., Icariin conjugated hyaluronic acid/collagen hydrogel for osteochondral interface restoration. *Acta Biomater.* **2018,** *74*, 156-167.

140.   Khader, A.; Arinzeh, T. L., Biodegradable zinc oxide composite scaffolds promote osteochondral differentiation of mesenchymal stem cells. *Biotechnol. Bioeng.* **2019,** *0*.

141.   Yu, X.; Zhao, T.; Qi, Y.; Luo, J.; Fang, J.; Yang, X.; Liu, X.; Xu, T.; Yang, Q.;   Gou, Z.; Dai, X., In vitro Chondrocyte Responses in Mg-doped Wollastonite/Hydrogel Composite Scaffolds for Osteochondral Interface Regeneration. *Sci. Rep.* **2018,** *8*, 17911.

142.   Wang, C.; Chen, B.; Wang, W.; Zhang, X.; Hu, T.; He, Y.; Lin, K.; Liu, X., Strontium released bi-lineage scaffolds with immunomodulatory properties induce a pro-

regenerative environment for osteochondral regeneration. *Mater. Sci. Eng. C* **2019,** *103*, 109833.

143.   Lin, R.; Deng, C.; Li, X.; Liu, Y.; Zhang, M.; Qin, C.; Yao, Q.; Wang, L.; Wu, C., Copper-incorporated bioactive glass-ceramics inducing anti-inflammatory phenotype and regeneration of cartilage/bone interface. *Theranostics* **2019,** *9*, 6300-6313.

144.   Baker, M. I.; Walsh, S. P.; Schwartz, Z.; Boyan, B. D., A review of polyvinyl alcohol and its uses in cartilage and orthopedic applications. *J. Biomed. Mater. Res. B* **2012,** *100B*, 1451-1457.

145.   Nathwani, D.; McNicholas, M.; Hart, A.; Miles, J.; Bobic, V., Partial Resurfacing of the Knee with the BioPoly Implant: Interim Report at 2 Years. *JBJS Open Access* **2017,** *2*, e0011.

146.   Pina, S.; Ribeiro, V.; Oliveira, J. M.; Reis, R. L., Pre-clinical and Clinical Management of Osteochondral Lesions. In *Regenerative Strategies for the Treatment of Knee Joint Disabilities*, Oliveira, J. M.; Reis, R. L., Eds. Springer International Publishing: Cham, 2017; pp 147-161.

147.   Jeuken, M. R.; Roth, K. A.; Peters, J. R. W. R.; Van Donkelaar, C. C.; Thies, C. J.; Van Rhijn, W. L.; Emans, J. P., Polymers in Cartilage Defect Repair of the Knee: Current Status and Future Prospects. *Polymers* **2016,** *8*.

148.   Kon, E.; Filardo, G.; Perdisa, F.; Venieri, G.; Marcacci, M., Clinical results of multilayered biomaterials for osteochondral regeneration. *Journal of Experimental Orthopaedics* **2014,** *1*, 10.

149.   Slivka, M. A.; Leatherbury, N. C.; Kieswetter, K.; Niederauer, G. G., Porous, Resorbable, Fiber-Reinforced Scaffolds Tailored for Articular Cartilage Repair. *Tissue Eng.* **2001,** *7*, 767-780.

150.   Pförringer, D.; Harrasser, N.; Mühlhofer, H.; Kiokekli, M.; Stemberger, A.; van Griensven, M.; Lucke, M.; Burgkart, R.; Obermeier, A., Osteoinduction and -conduction through absorbable bone substitute materials based on calcium sulfate: in vivo biological behavior in a rabbit model. *J. Mater. Sci. Mater. Med.* **2018,** *29*, 17.

151.   Thomas, M. V.; Puleo, D. A., Calcium sulfate: Properties and clinical applications. *J. Biomed. Mater. Res. B* **2009,** *88B*, 597-610.

152.   Dell'Osso, G.; Bottai, V.; Bugelli, G.; Manisco, T.; Cazzella, N.; Celli, F.; Guido, G.; Giannotti, S., The biphasic bioresorbable scaffold (Trufit((R))) in the osteochondral knee lesions: long-term clinical and MRI assessment in 30 patients. *Musculoskelet Surgery* **2016,** *100*, 93-6.

153.   Dhollander, A. A.; Liekens, K.; Almqvist, K. F.; Verdonk, R.; Lambrecht, S.; Elewaut, D.; Verbruggen, G.; Verdonk, P. C., A pilot study of the use of an osteochondral scaffold plug for cartilage repair in the knee and how to deal with early clinical failures. *Arthroscopy* **2012,** *28*, 225-33.

154.   Joshi, N.; Reverte-Vinaixa, M.; Díaz-Ferreiro, E. W.; Domínguez-Oronoz, R., Synthetic Resorbable Scaffolds for the Treatment of Isolated Patellofemoral Cartilage Defects in Young Patients:Magnetic Resonance Imaging and Clinical Evaluation. *The American Journal of Sports Medicine* **2012,** *40*, 1289-1295.

155.   Verhaegen, J.; Clockaerts, S.; Van Osch, G.; Somville, J.; Verdonk, P.; Mertens, P., TruFit Plug for Repair of Osteochondral Defects—Where Is the Evidence? Systematic Review of Literature. *Cartilage* **2015,** *6*, 12-19.

156.   Neto, A. S.; Ferreira, J. M. F., Synthetic and Marine-Derived Porous Scaffolds for Bone Tissue Engineering. *Materials (Basel, Switzerland)* **2018,** *11*, 1702.

157.   Matta, C.; Szűcs-Somogyi, C.; Kon, E.; Robinson, D.; Neufeld, T.; Altschuler, N.; Berta, A.; Hangody, L.; Veréb, Z.; Zákány, R., Osteogenic differentiation of human bone marrow-derived mesenchymal stem cells is enhanced by an aragonite scaffold. *Differentiation* **2019,** *107*, 24-34.

158.   Kon, E.; Filardo, G.; Shani, J.; Altschuler, N.; Levy, A.; Zaslav, K.; Eisman, J. E.; Robinson, D., Osteochondral regeneration with a novel aragonite-hyaluronate biphasic scaffold: up to 12-month follow-up study in a goat model. *J. Orthop. Surg. Res.* **2015,** *10*, 81-81.

159.   CartiHeal Announces FDA IDE Approval of its Agili-C™ Implant for the Treatment of Joint Surface Lesions. https://www.cartiheal.com/news/cartiheal-announces-fda-ide-approval-of-its-agili-c-implant-for-the-treatment-of-joint-surface-lesions/ (accessed October 31).

160.   Du, Y.; Liu, H.; Yang, Q.; Wang, S.; Wang, J.; Ma, J.; Noh, I.; Mikos, A. G.; Zhang, S., Selective laser sintering scaffold with hierarchical architecture and gradient composition for osteochondral repair in rabbits. *Biomaterials* **2017,** *137*, 37-48.

161.   Liao, J.; Tian, T.; Shi, S.; Xie, X.; Ma, Q.; Li, G.; Lin, Y., The fabrication of biomimetic biphasic CAN-PAC hydrogel with a seamless interfacial layer applied in osteochondral defect repair. *Bone Research* **2017,** *5*, 17018.

162.   Mellor, L. F.; Huebner, P.; Cai, S.; Mohiti-Asli, M.; Taylor, M. A.; Spang, J.; Shirwaiker, R. A.; Loboa, E. G., Fabrication and Evaluation of Electrospun, 3D-Bioplotted, and Combination of Electrospun/3D-Bioplotted Scaffolds for Tissue Engineering Applications. *BioMed Res. Int.* **2017,** *2017*, 6956794-6956794.

163.	Rajasekharan, A. K.; Bordes, R.; Sandström, C.; Ekh, M.; Andersson, M., Hierarchical and Heterogeneous Bioinspired Composites—Merging Molecular Self-Assembly with Additive Manufacturing. *Small* **2017,** *13*, 1700550.

164.	Su, C.; Su, Y.; Li, Z.; Haq, M. A.; Zhou, Y.; Wang, D., In situ synthesis of bilayered gradient poly(vinyl alcohol)/hydroxyapatite composite hydrogel by directional freezing-thawing and electrophoresis method. *Mater. Sci. Eng. C* **2017,** *77*, 76-83.

165.	Yao, H.; Kang, J.; Li, W.; Liu, J.; Xie, R.; Wang, Y.; Liu, S.; Wang, D.-A.; Ren, L., Novel β-TCP/PVA bilayered hydrogels with considerable physical and bio-functional properties for osteochondral repair. *Biomed. Mater.* **2017,** *13*, 015012.

166.	Bittner, S. M.; Smith, B. T.; Diaz-Gomez, L.; Hudgins, C. D.; Melchiorri, A. J.; Scott, D. W.; Fisher, J. P.; Mikos, A. G., Fabrication and mechanical characterization of 3D printed vertical uniform and gradient scaffolds for bone and osteochondral tissue engineering. *Acta Biomater.* **2019,** *90*, 37-48.

167.	Deliormanlı, A. M.; Atmaca, H., Biological Response of Osteoblastic and Chondrogenic Cells to Graphene-Containing PCL/Bioactive Glass Bilayered Scaffolds for Osteochondral Tissue Engineering Applications. *Appl. Biochem. Biotechnol.* **2018,** *186*, 972-989.

168.	Filardo, G.; Perdisa, F.; Gelinsky, M.; Despang, F.; Fini, M.; Marcacci, M.; Parrilli, A. P.; Roffi, A.; Salamanna, F.; Sartori, M.; Schütz, K.; Kon, E., Novel alginate biphasic scaffold for osteochondral regeneration: an in vivo evaluation in rabbit and sheep models. *J. Mater. Sci. Mater. Med.* **2018,** *29*, 74.

169.	Kang, H.; Zeng, Y.; Varghese, S., Functionally graded multilayer scaffolds for in vivo osteochondral tissue engineering. *Acta Biomater.* **2018,** *78*, 365-377.

170.	Erickson, A. E.; Sun, J.; Lan Levengood, S. K.; Swanson, S.; Chang, F.-C.; Tsao, C. T.; Zhang, M., Chitosan-based composite bilayer scaffold as an in vitro osteochondral defect regeneration model. *Biomed. Microdevices* **2019,** *21*, 34.

171.	Lin, T.-H.; Wang, H.-C.; Cheng, W.-H.; Hsu, H.-C.; Yeh, M.-L., Osteochondral Tissue Regeneration Using a Tyramine-Modified Bilayered PLGA Scaffold Combined with Articular Chondrocytes in a Porcine Model. *Int. J. Mol. Sci.* **2019,** *20*.

172.	Maciulaitis, J.; Miskiniene, M.; Rekštytė, S.; Bratchikov, M.; Darinskas, A.; Simbelyte, A.; Daunoras, G.; Laurinaviciene, A.; Laurinavicius, A.; Gudas, R.; Malinauskas, M.; Maciulaitis, R., Osteochondral Repair and Electromechanical Evaluation of Custom 3D Scaffold Microstructured by Direct Laser Writing Lithography. *Cartilage* **2019,** *0*, 1-11.

173.   Mahapatra, C.; Kim, J.-J.; Lee, J.-H.; Jin, G.-Z.; Knowles, J. C.; Kim, H.-W., Differential chondro- and osteo-stimulation in three-dimensional porous scaffolds with different topological surfaces provides a design strategy for biphasic osteochondral engineering. *J. Tissue Eng.* **2019,** *10*, 2041731419826433-2041731419826433.

174.   Wu, X., Biphasic osteochondral scaffold fabrication using multi-material mask projection stereolithography. *Rapid Prototyping Journal* **2019,** *25*, 277-288.

175.   Bhardwaj, N.; Kundu, S. C., Electrospinning: A fascinating fiber fabrication technique. *Biotechnol. Adv.* **2010,** *28*, 325-347.

176.   Casanova, M. R.; Reis, R. L.; Martins, A.; Neves, N. M., The Use of Electrospinning Technique on Osteochondral Tissue Engineering. In *Osteochondral Tissue Engineering: Nanotechnology, Scaffolding-Related Developments and Translation*, Oliveira, J. M.; Pina, S.; Reis, R. L.; San Roman, J., Eds. Springer International Publishing: Cham, 2018; pp 247-263.

177.   Liu, Y.; Zhang, X.; Xia, Y.; Yang, H., Magnetic-Field-Assisted Electrospinning of Aligned Straight and Wavy Polymeric Nanofibers. *Adv. Mater.* **2010,** *22*, 2454-2457.

178.   Tindell, K. R.; Holloway, J.; Ronken, S. In *Controlling fiber alignment using magnetically-assisted electrospinning for interfacial tissue repair*, Society for Biomaterials Annual Meeting and Exposition 2019: The Pinnacle of Biomaterials Innovation and Excellence - Transactions of the 42nd Annual Meeting, Seattle, WA, Transactions of the Annual Meeting of the Society for Biomaterials and the Annual International Biomaterials Symposium: Seattle, WA, 2019.

179.   Balu, R.; Singaravelu, S.; Nagiah, N., Bioceramic Nanofibres by Electrospinning. *Fibers* **2014,** *2*, 221-239.

180.   Zhang, Y.; Liu, X.; Zeng, L.; Zhang, J.; Zuo, J.; Zou, J.; Ding, J.; Chen, X., Polymer Fiber Scaffolds for Bone and Cartilage Tissue Engineering. *Adv. Funct. Mater.* **2019,** *0*, 1903279.

181.   Yunos, D. M.; Ahmad, Z.; Salih, V.; Boccaccini, A. R., Stratified scaffolds for osteochondral tissue engineering applications: Electrospun PDLLA nanofibre coated Bioglass®-derived foams. *J. Biomater. Appl.* **2011,** *27*, 537-551.

182.   Gacasan, E. G.; Sehnert, R. M.; Ehrhardt, D. A.; Grunlan, M. A., Templated, Macroporous PEG-DA Hydrogels and Their Potential Utility as Tissue Engineering Scaffolds. *Macromol. Mater. Eng.* **2017,** *302*, 1600512.

183.   Woodard, L. N.; Kmetz, K. T.; Roth, A. A.; Page, V. M.; Grunlan, M. A., Porous Poly(ε-caprolactone)-Poly(l-lactic acid) Semi-Interpenetrating Networks as Superior,

Defect-Specific Scaffolds with Potential for Cranial Bone Defect Repair. *Biomacromolecules* **2017,** *18*, 4075-4083.

184.   Scaffaro, R.; Lopresti, F.; Botta, L.; Rigoglioso, S.; Ghersi, G., Integration of PCL and PLA in a monolithic porous scaffold for interface tissue engineering. *J. Mech. Behav. Biomed. Mater.* **2016,** *63*, 303-313.

185.   Tang, G.; Zhang, H.; Zhao, Y.; Zhang, Y.; Li, X.; Yuan, X., Preparation of PLGA Scaffolds with Graded Pores by Using a Gelatin-Microsphere Template as Porogen. *J. Biomater. Sci. Polym. Ed.* **2012,** *23*, 2241-2257.

186.   Deville, S.; Saiz, E.; Nalla, R. K.; Tomsia, A. P., Freezing as a Path to Build Complex Composites. *Science* **2006,** *311*, 515.

187.   Grenier, J.; Duval, H.; Barou, F.; Lv, P.; David, B.; Letourneur, D., Mechanisms of Pore Formation in Hydrogel Scaffolds Textured by Freeze-Drying. *Acta Biomater.* **2019**.

188.   Annabi, N.; Nichol, J. W.; Zhong, X.; Ji, C.; Koshy, S.; Khademhosseini, A.; Dehghani, F., Controlling the Porosity and Microarchitecture of Hydrogels for Tissue Engineering. *Tissue Eng. Part B Rev.* **2010,** *16*, 371-383.

189.   Haugh, M. G.; Murphy, C. M.; O'Brien, F. J., Novel Freeze-Drying Methods to Produce a Range of Collagen–Glycosaminoglycan Scaffolds with Tailored Mean Pore Sizes. *Tissue Eng. Part C Methods* **2009,** *16*, 887-894.

190.   Pawelec, K. M.; Husmann, A.; Best, S. M.; Cameron, R. E., Understanding anisotropy and architecture in ice-templated biopolymer scaffolds. *Mater. Sci. Eng. C* **2014,** *37*, 141-147.

191.   An, J.; Teoh, J. E. M.; Suntornnond, R.; Chua, C. K., Design and 3D Printing of Scaffolds and Tissues. *Engineering* **2015,** *1*, 261-268.

192.   Jammalamadaka, U.; Tappa, K., Recent Advances in Biomaterials for 3D Printing and Tissue Engineering. *J. Funct. Biomater.* **2018,** *9*, 22.

193.   Daly, A. C.; Freeman, F. E.; Gonzalez-Fernandez, T.; Critchley, S. E.; Nulty, J.; Kelly, D. J., 3D Bioprinting for Cartilage and Osteochondral Tissue Engineering. *Adv. Healthcare Mater.* **2017,** *6*, 1700298.

194.   Radhakrishnan, J.; Subramanian, A.; Krishnan, U. M.; Sethuraman, S., Injectable and 3D Bioprinted Polysaccharide Hydrogels: From Cartilage to Osteochondral Tissue Engineering. *Biomacromolecules* **2017,** *18*, 1-26.

195.   Idaszek, J.; Costantini, M.; Karlsen, T. A.; Jaroszewicz, J.; Colosi, C.; Testa, S.; Fornetti, E.; Bernardini, S.; Seta, M.; Kasarełło, K.; Wrzesień, R.; Cannata, S.; Barbetta, A.; Gargioli, C.; Brinchman, J. E.; Święszkowski, W., 3D bioprinting of hydrogel constructs with cell and material gradients for the regeneration of full-thickness chondral defect using a microfluidic printing head. *Biofabrication* **2019,** *11*, 044101.

196.   Skoog, S. A.; Goering, P. L.; Narayan, R. J., Stereolithography in tissue engineering. *J. Mater. Sci. Mater. Med.* **2014,** *25*, 845-856.

197.   Wicker, R. B.; MacDonald, E. W., Multi-material, multi-technology stereolithography. *Virtual Phys. Prototyp.* **2012,** *7*, 181-194.

198.   Raimondi, M. T.; Eaton, S. M.; Nava, M. M.; Laganà, M.; Cerullo, G.; Osellame, R., Two-Photon Laser Polymerization: From Fundamentals to Biomedical Application in Tissue Engineering and Regenerative Medicine. *J. Appl. Biomater. Funct. Mater.* **2012,** *10*, 56-66.

199.   Çakmak, S.; Çakmak, A. S.; Kaplan, D. L.; Gümüşderelioğlu, M., A Silk Fibroin and Peptide Amphiphile-Based Co-Culture Model for Osteochondral Tissue Engineering. *Macromol. Biosci.* **2016,** *16*, 1212-1226.

200.   Amadori, S.; Torricelli, P.; Panzavolta, S.; Parrilli, A.; Fini, M.; Bigi, A., Multi-Layered Scaffolds for Osteochondral Tissue Engineering: In Vitro Response of Co-Cultured Human Mesenchymal Stem Cells. *Macromol. Biosci.* **2015,** *15*, 1535-1545.

201.   Yang, J.; Zhang, Y. S.; Yue, K.; Khademhosseini, A., Cell-laden hydrogels for osteochondral and cartilage tissue engineering. *Acta Biomater.* **2017,** *57*, 1-25.

202.   Chang, C.-H.; Lin, C.-C.; Chou, C.-H.; Lin, F.-H.; Liu, H.-C., Novel bioreactors for osteochondral tissue engineering. *Biomed. Eng.: Appl. Basis Commun.* **2005,** *17*, 38-43.

203.   Hansmann, J.; Groeber, F.; Kahlig, A.; Kleinhans, C.; Walles, H., Bioreactors in tissue engineering—principles, applications and commercial constraints. *Biotechnol. J.* **2013,** *8*, 298-307.

204.   Li, K.; Zhang, C.; Qiu, L.; Gao, L.; Zhang, X., Advances in Application of Mechanical Stimuli in Bioreactors for Cartilage Tissue Engineering. *Tissue Eng. Part B Rev.* **2017,** *23*, 399-411.

205.   Martin, Y.; Eldardiri, M.; Lawrence-Watt, D. J.; Sharpe, J. R., Microcarriers and Their Potential in Tissue Regeneration. *Tissue Eng. Part B Rev.* **2010,** *17*, 71-80.

206.   Zhou, A.; Ye, Z.; Zhou, Y.; Tan, W.-s., Bioactive poly(ε-caprolactone) microspheres with tunable open pores as microcarriers for tissue regeneration. *J. Biomater. Appl.* **2019,** *33*, 1242-1251.

207.   Carvalho, M. R.; Reis, R. L.; Oliveira, J. M., Mimicking the 3D biology of osteochondral tissue with microfluidic-based solutions: breakthroughs towards boosting drug testing and discovery. *Drug Discovery Today* **2018,** *23*, 711-718.

208.   Beddoes, C. M.; Whitehouse, M. R.; Briscoe, W. H.; Su, B., Hydrogels as a Replacement Material for Damaged Articular Hyaline Cartilage. *Materials* **2016,** *9*, 443.

209.   Gong, J. P.; Katsuyama, Y.; Kurokawa, T.; Osada, Y., Double-Network Hydrogels with Extremely High Mechanical Strength. *Adv. Mater.* **2003,** *15*, 1155-1158.

210.   Arnold, M. P.; Daniels, A. U.; Ronken, S.; García, H. A.; Friederich, N. F.; Kurokawa, T.; Gong, J. P.; Wirz, D., Acrylamide Polymer Double-Network Hydrogels: Candidate Cartilage Repair Materials with Cartilage-Like Dynamic Stiffness and Attractive Surgery-Related Attachment Mechanics. *Cartilage* **2011,** *2*, 374-383.

211.   Means, A. K.; Ehrhardt, D. A.; Whitney, L. V.; Grunlan, M. A., Thermoresponsive Double Network Hydrogels with Exceptional Compressive Mechanical Properties. *Macromol. Rapid Commun.* **2017,** *38*, 1700351-n/a.

212.   Means, A. K.; Shrode, C. S.; Whitney, L. V.; Ehrhardt, D. A.; Grunlan, M. A., Double Network Hydrogels that Mimic the Modulus, Strength, and Lubricity of Cartilage. *Biomacromolecules* **2019,** *20*, 2034-2042.

213.   Weisgerber, D. W.; Caliari, S. R.; Harley, B. A., Mineralized collagen scaffolds induce hMSC osteogenesis and matrix remodeling. *Biomater. Sci.* **2015,** *3*, 533-42.

214.   Vo, T. N.; Kasper, F. K.; Mikos, A. G., Strategies for Controlled Delivery of Growth Factors and Cells for Bone Regeneration. *Adv. Drug Del. Rev.* **2012,** *64*, 1292-1309.

215.   Lyons, F. G.; Gleeson, J. P.; Partap, S.; Coghlan, K.; O'Brien, F. J., Novel microhydroxyapatite particles in a collagen scaffold: a bioactive bone void filler? *Clin. Orthop. Relat. Res.* **2014,** *472*, 1318-28.

216.   Bailey, B. M.; Fei, R.; Munoz-Pinto, D.; Hahn, M. S.; Grunlan, M. A., PDMS$_{star}$-PEG hydrogels prepared via solvent-induced phase separation (SIPS) and their potential utility as tissue engineering scaffolds. *Acta Biomater.* **2012,** *8*, 4324-4333.

217.   Hou, Y.; Schoener, C. A.; Regan, K. R.; Munoz-Pinto, D.; Hahn, M. S.; Grunlan, M. A., Photo-cross-linked PDMSstar-PEG hydrogels: synthesis, characterization, and

potential application for tissue engineering scaffolds. *Biomacromolecules* **2010,** *11*, 648-656.

218.   Zhu, J., Bioactive modification of poly(ethylene glycol) hydrogels for tissue engineering. *Biomaterials* **2010,** *31*, 4639-4656.

219.   Mann, B. K.; Gobin, A. S.; Tsai, A. T.; Schmedlen, R. H.; West, J. L., Smooth muscle cell growth in photopolymerized hydrogels with cell adhesive and proteolytically degradable domains: Synthetic ECM analogs for tissue engineering. *Biomaterials* **2001,** *22*, 3045-3051.

220.   Bailey, B. M.; Hui, V.; Fei, R.; Grunlan, M. A., Tuning PEG-DA hydrogel properties via solvent-induced phase separation (SIPS). *J. Mater. Chem.* **2011,** *21*, 18776-18782.

221.   Murphy, W. L.; Dennis, R. G.; Kileny, J. L.; Mooney, D. J., Salt fusion: An approach to improve pore interconnectivity within tissue engineering scaffolds. *Tissue Eng.* **2002,** *8*, 43-52.

222.   Zhang, D.; Burkes, W. L.; Schoener, C. A.; Grunlan, M. A., Porous inorganic–organic shape memory polymers. *Polymer* **2012,** *53*, 2935-2941.

223.   Bencherif, S. A.; Sands, R. W.; Bhatta, D.; Arany, P.; Verbeke, C. S.; Edwards, D. A.; Mooney, D. J., Injectable preformed scaffolds with shape-memory properties. *Proc. Natl. Acad. Sci. U. S. A.* **2012,** *109*, 19590-19595.

224.   Kokubo, T.; Takadama, H., How useful is SBF in predicting in vivo bone bioactivity? *Biomaterials* **2006,** *27*, 2907-2915.

225.   Burdick, J. A.; Anseth, K. S., Photoencapsulation of osteoblasts in injectable RGD-modified PEG hydrogels for bone tissue engineering. *Biomaterials* **2002,** *23*, 4315-4323.

226.   Griffith, L. G., Polymeric biomaterials. *Acta Mater.* **2000,** *48*, 263-277.

227.   Wu, L.; Ding, J., Effects of porosity and pore size on *in vitro* degradation of three-dimensional porous poly(D,L-lactide-*co*-glycolide) scaffolds for tissue engineering. *J. Biomed. Mater. Res. A* **2005,** *75A*, 767-777.

228.   Sobhana, S. S. L.; Sundaraseelan, J.; Sekar, S.; Sastry, T. P.; Mandal, A. B., Gelatin–Chitosan composite capped gold nanoparticles: a matrix for the growth of hydroxyapatite. *J. Nanopart. Res.* **2008,** *11*, 333-340.

229.   Dinh, T. M. T.; Nguyen, T. T.; Pham, T. N.; Nguyen, T. P.; Nguyen, T. T. T.; Hoang, T.; Grossin, D.; Bertrand, G.; Drouet, C., Electrodeposition of HAp coatings on

Ti6Al4V alloy and its electrochemical behavior in simulated body fluid solution. *Adv. Nat. Sci.: Nanosci. Nanotechnol.* **2016,** *7*, 025008.

230.   Liu, S.; Liu, G.; Wei, W.; Xiangli, F.; Jin, W., Ceramic Supported PDMS and PEGDA Composite Membranes for CO2 Separation. *Chin. J. Chem. Eng.* **2013,** *21*, 348-356.

231.   Frassica, M. T.; Grunlan, M. A., Perspectives on synthetic materials to guide tissue regeneration for osteochondral defect repair. *ACS Biomater. Sci. Eng.* **2020,** *6*, 4324-4336.

232.   Chen, M.; Zhang, Y.; Zhou, Y.; Zhang, Y.; Lang, M.; Ye, Z.; Tan, W.-S., Pendant small functional groups on poly(ϵ-caprolactone) substrate modulate adhesion, proliferation and differentiation of human mesenchymal stem cells. *Colloids Surf., B* **2015,** *134*, 322-331.

233.   Phadke, A.; Zhang, C.; Hwang, Y.; Vecchio, K.; Varghese, S., Templated mineralization of synthetic hydrogels for bone-like composite materials: role of matrix hydrophobicity. *Biomacromolecules* **2010,** *11*, 2060-2068.

234.   Lo, K. W. H.; Ashe, K. M.; Kan, H. M.; Laurencin, C. T., The role of small molecules in musculoskeletal regeneration. *Regen. Med.* **2012,** *7*, 535-549.

235.   Newman, M. R.; Benoit, D. S. W., Local and targeted drug delivery for bone regeneration. *Curr. Opin. Biotechnol.* **2016,** *40*, 125-132.

236.   Zhang, D.; George, O. J.; Petersen, K. M.; Jimenez-Vergara, A. C.; Hahn, M. S.; Grunlan, M. A., A bioactive "self-fitting" shape memory polymer scaffold with potential to treat cranio-maxillo facial bone defects. *Acta Biomater.* **2014,** *10*, 4597-4605.

237.   Griffin, M. F.; Ibrahim, A.; Seifalian, A. M.; Butler, P. E. M.; Kalaskar, D. M.; Ferretti, P., Chemical group-dependent plasma polymerisation preferentially directs adipose stem cell differentiation towards osteogenic or chondrogenic lineages. *Acta Biomater.* **2017,** *50*, 450-461.

238.   Zheng, Y.; Liu, L.; Xiong, C.; Zhang, L., Enhancement of bioactivity on modified polyetheretherketone surfaces with –COOH, –OH and –PO4H2 functional groups. *Mater. Lett.* **2018,** *213*, 84-87.

239.   Keselowsky, B. G.; Collard, D. M.; García, A. J., Integrin binding specificity regulates biomaterial surface chemistry effects on cell differentiation. *Proc. Natl. Acad. Sci. U. S. A.* **2005,** *102*, 5953-5957.

240.   Gandavarapu, N. R.; Mariner, P. D.; Schwartz, M. P.; Anseth, K. S., Extracellular matrix protein adsorption to phosphate-functionalized gels from serum promotes

osteogenic differentiation of human mesenchymal stem cells. *Acta Biomater.* **2013,** *9*, 4525-4534.

241.   Watson, B. M.; Kasper, K. F.; Mikos, A. G., Phosphorous-containing polymers for regenerative medicine. *Biomed. Mater.* **2014,** *9*, 025014.

242.   Naz Guven, M.; Akyol, E.; Demir Duman, F.; Yagci Acar, H.; Karahan, O.; Avci, D., Urea dimethacrylates functionalized with bisphosphonate/bisphosphonic acid for improved dental materials. *J. Polym. Sci., Part A: Polym. Chem.* **2017,** *55*, 3195-3204.

243.   Wang, D.-a.; Williams, C. G.; Li, Q.; Sharma, B.; Elisseeff, J. H., Synthesis and characterization of a novel degradable phosphate-containing hydrogel. *Biomaterials* **2003,** *24*, 3969-3980.

244.   Ikemura, K.; Endo, T.; Kadoma, Y., A review of the developments of multi-purpose primers and adhesives comprising novel dithiooctanoate monomers and phosphonic acid monomers. *Dent. Mater. J.* **2012,** *31*, 1-25.

245.   Kim, D. S.; Suriboot, J.; Grunlan, M. A.; Tai, B. L., Feasibility study of silicone stereolithography with an optically created dead zone. *Addit. Manuf.* **2019,** *29*, 100793.

246.   Munoz-Pinto, D. J.; Jimenez-Vergara, A. C.; Gharat, T. P.; Hahn, M. S., Characterization of sequential collagen-poly(ethylene glycol) diacrylate interpenetrating networks and initial assessment of their potential for vascular tissue engineering. *Biomaterials* **2015,** *40*, 32-42.

247.   Arabiyat, A. S.; Diaz-Rodriguez, P.; Erndt-Marino, J. D.; Totsingan, F.; Mekala, S.; Gross, R. A.; Hahn, M. S., Effect of poly(sophorolipid) functionalization on human mesenchymal stem cell osteogenesis and immunomodulation. *ACS Appl. Bio Mater.* **2019,** *2*, 118-126.

248.   Gregory, C. A.; Grady Gunn, W.; Peister, A.; Prockop, D. J., An Alizarin red-based assay of mineralization by adherent cells in culture: comparison with cetylpyridinium chloride extraction. *Anal. Biochem.* **2004,** *329*, 77-84.

249.   Munoz-Pinto, D. J.; Grigoryan, B.; Long, J.; Grunlan, M.; Hahn, M. S., An approach for assessing hydrogel hydrophobicity. *J. Biomed. Mater. Res. A* **2012,** *100A*, 2855-2860.

250.   Schreivogel, S.; Kuchibhotla, V.; Knaus, P.; Duda, G. N.; Petersen, A., Load-induced osteogenic differentiation of mesenchymal stromal cells is caused by mechano-regulated autocrine signaling. *J. Tissue Eng. Regen. Med.* **2019,** *13*, 1992-2008.

251. Lysdahl, H.; Baatrup, A.; Foldager, C. B.; Bünger, C., Preconditioning Human Mesenchymal Stem Cells with a Low Concentration of BMP2 Stimulates Proliferation and Osteogenic Differentiation In Vitro. *BioResearch Open Access* **2014,** *3*, 278-285.

252. Boys, A. J.; McCorry, M. C.; Rodeo, S.; Bonassar, L. J.; Estroff, L. A., Next Generation Tissue Engineering of Orthopedic Soft Tissue-to-Bone Interfaces. *MRS Commun.* **2017,** *7*, 289-308.

253. Barajaa, M. A.; Nair, L. S.; Laurencin, C. T., Bioinspired scaffold designs for regenerating musculoskeletal Tissue interfaces. *Regener. Eng. Transl. Med.* **2019**.

254. Perez, R. A.; Mestres, G., Role of pore size and morphology in musculo-skeletal tissue regeneration. *Mater. Sci. Eng. C* **2016,** *61*, 922-939.

255. Lu, H. H.; Subramony, S. D.; Boushell, M. K.; Zhang, X., Tissue Engineering Strategies for the Regeneration of Orthopedic Interfaces. *Ann. Biomed. Eng.* **2010,** *38*, 2142-2154.

256. Seidi, A.; Ramalingam, M.; Elloumi-Hannachi, I.; Ostrovidov, S.; Khademhosseini, A., Gradient biomaterials for soft-to-hard interface tissue engineering. *Acta Biomater.* **2011,** *7*, 1441-1451.

257. Frassica, M. T.; Jones, S. K.; Suriboot, J.; Arabiyat, A. S.; Ramirez, E. M.; Culibrk, R. A.; Hahn, M. S.; Grunlan, M. A., Enhanced osteogenic potential of phosphonated-siloxane hydrogel scaffolds. *accepted*.

258. Kim, I. L.; Mauck, R. L.; Burdick, J. A., Hydrogel design for cartilage tissue engineering: A case study with hyaluronic acid. *Biomaterials* **2011,** *32*, 8771-8782.

259. Sharma, B.; Williams, C. G.; Kim, T. K.; Sun, D.; Malik, A.; Khan, M.; Leong, K.; Elisseeff, J. H., Designing Zonal Organization into Tissue-Engineered Cartilage. *Tissue Eng.* **2007,** *13*, 405-414.

260. Camarero-Espinosa, S.; Rothen-Rutishauser, B.; Weder, C.; Foster, E. J., Directed cell growth in multi-zonal scaffolds for cartilage tissue engineering. *Biomaterials* **2016,** *74*, 42-52.

261. Girão, A. F.; Semitela, Â.; Ramalho, G.; Completo, A.; Marques, P. A. A. P., Mimicking nature: Fabrication of 3D anisotropic electrospun polycaprolactone scaffolds for cartilage tissue engineering applications. *Composites Part B: Engineering* **2018,** *154*, 99-107.

262. Zhu, D.; Tong, X.; Trinh, P.; Yang, F., Mimicking Cartilage Tissue Zonal Organization by Engineering Tissue-Scale Gradient Hydrogels as 3D Cell Niche. *Tissue Eng., Part A* **2017,** *24*, 1-10.

263.   Venkatesan, J. K.; Meng, W.; Rey-Rico, A.; Schmitt, G.; Speicher-Mentges, S.; Falentin-Daudré, C.; Leroux, A.; Madry, H.; Migonney, V.; Cucchiarini, M., Enhanced Chondrogenic Differentiation Activities in Human Bone Marrow Aspirates via sox9 Overexpression Mediated by pNaSS-Grafted PCL Film-Guided rAAV Gene Transfer. *Pharmaceutics* **2020,** *12*.

264.   Joon Kwon, H., Chondrogenesis on sulfonate-coated hydrogels is regulated by their mechanical properties. *J. Mech. Behav. Biomed. Mater.* **2013,** *17*, 337-346.

265.   Cheng, K.; Zhu, Y.; Wang, D.; Li, Y.; Xu, X.; Cai, H.; Chu, H.; Li, J.; Zhang, D., Biomimetic synthesis of chondroitin sulfate-analogue hydrogels for regulating osteogenic and chondrogenic differentiation of bone marrow mesenchymal stem cells. *Mater. Sci. Eng. C* **2020,** *117*, 111368.
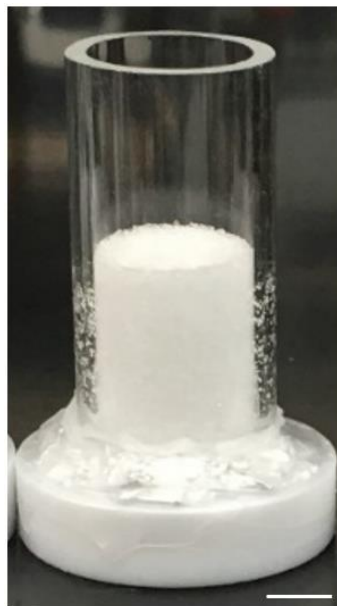
Figure A-1. A dry, fused salt template prepared within the 'hole-in-cap' mold (prior to addition of precursor solution). Scale bars = 5 mm.
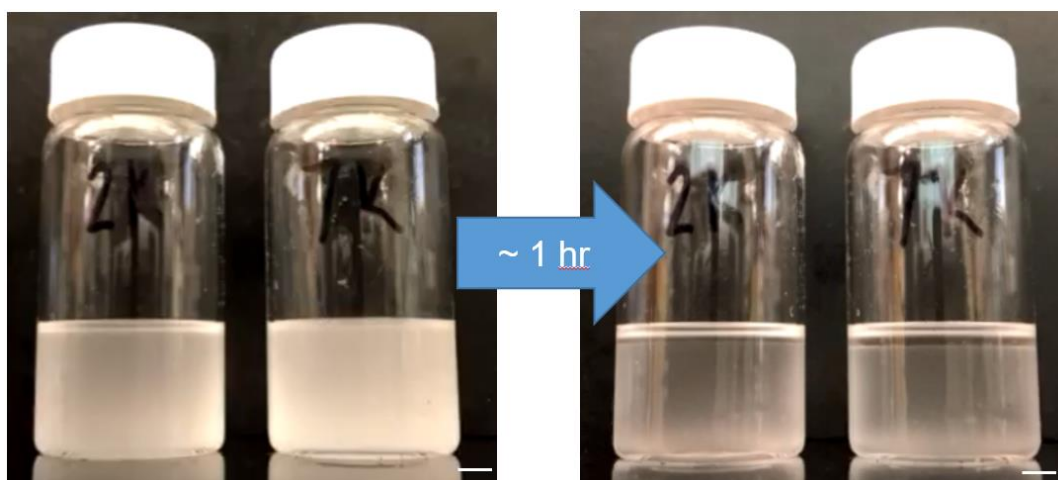
Figure A-2. Photographs displaying the separation of DCM precursor solutions containing 2k PDMS$_{star}$-MA at 20:80 (wt/wt %) (left vial in both pictures) and 7k PDMS$_{star}$-MA at 20:80 (wt/wt %) (right vial in both pictures) after 1 hr. Scale bars = 5 mm.

Table A-1. Percent sol for templated SIPS PDMS$_{star}$-PEG hydrogels and analogous PEG-DA control (0:100 wt/wt %) following DCM soak. All hydrogels were fabricated with medium salt (~270 µm).

	PEG	2k 10:90	2k 20:80	2k 30:70	7k 10:90	7k 20:80	7k 30:70
% Sol:	0.67 ± 0.71	2.00 ± 1.37	3.64 ± 1.50	2.30 ± 1.26	1.60 ± 1.20	4.98 ± 1.80	4.53 ± 0.75
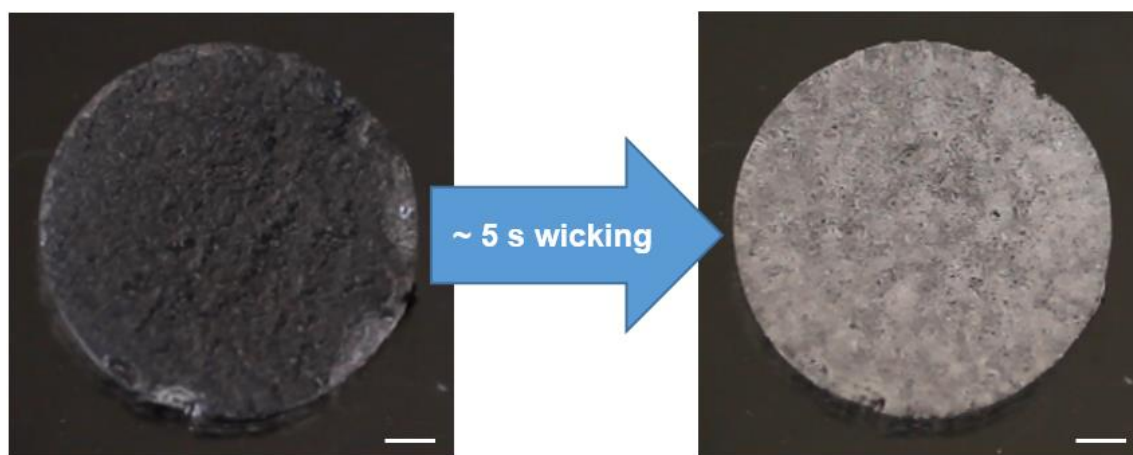
Figure A-3 Photographs displaying the effect of water wicking on a templated PEG-DA control (0:100 wt/wt %; prepared with mediums salt, ~270 µm) hydrogel after wicking with a Kimwipe during percent interconnectivity test. Scale bars = 2 mm.
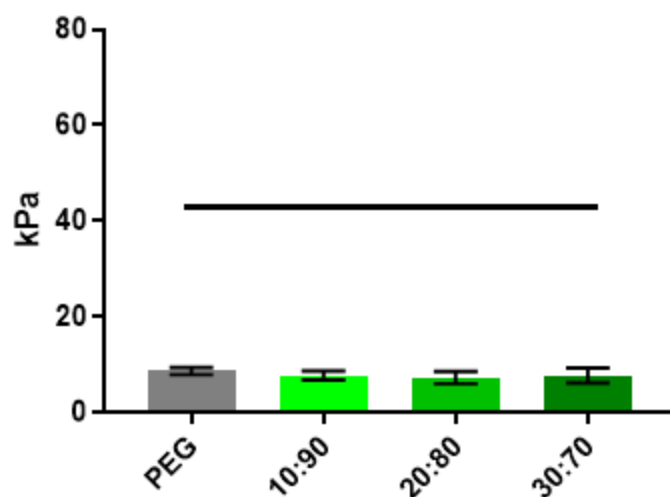
Figure A-4. Bulk compressive Young's modulus of templated SIPS PDMS$_{star}$-PEG hydrogels and analogous PEG-DA control. Hydrogels were fabricated with medium salt (~270 μm) and 2k PDMS$_{star}$-MA. No statistical difference among compositions were observed.
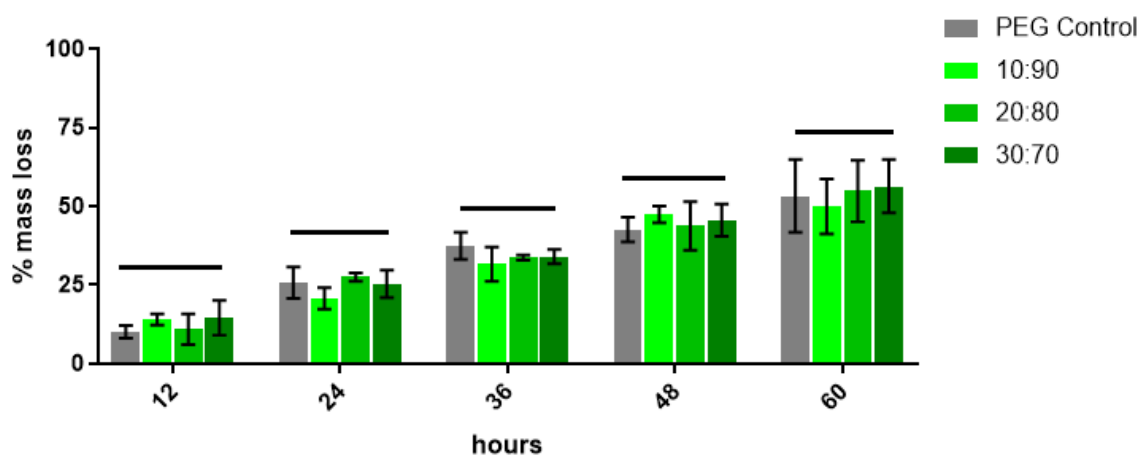
Figure A-5. Accelerated degradation (0.05M NaOH, 37 ℃) of templated SIPS PDMS$_{star}$-PEG hydrogels and analogous PEG-DA control. Hydrogels were fabricated with medium salt (~270 μm) and 2k PDMS$_{star}$-MA. For a given time point, no statistical differences among compositions were observed.
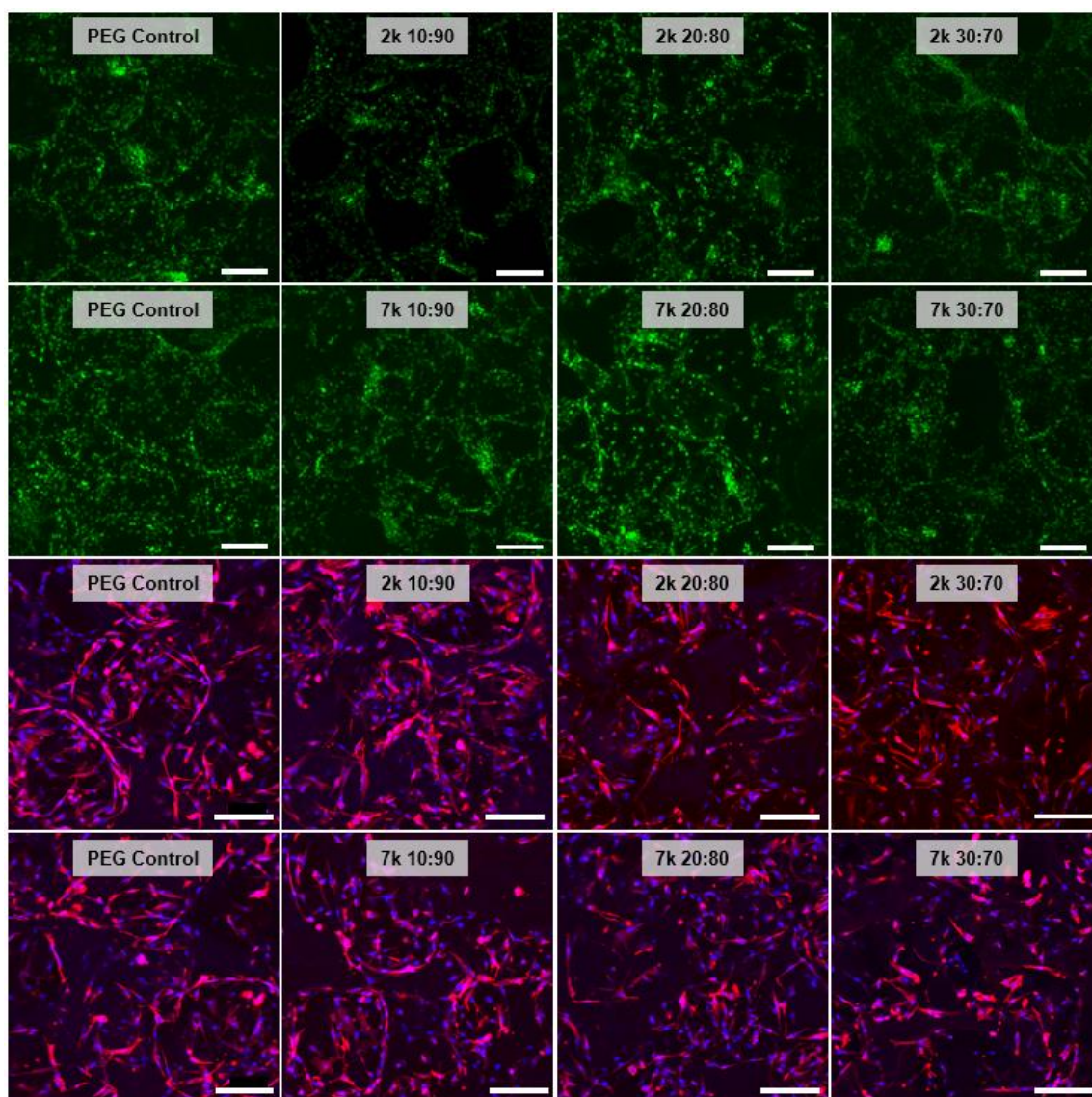
Figure A-6. SYBR green staining for DNA (top 2 rows) and stacked images of rhodamine phalloidin and DAPI staining (bottom 2 rows) after 48 hr culture with hBMSCs on templated SIPS PDMS$_{star}$-PEG scaffolds and analogous PEG-DA control. Scaffolds were fabricated with medium salt (~270 µm). Scale bars = 200 µm.
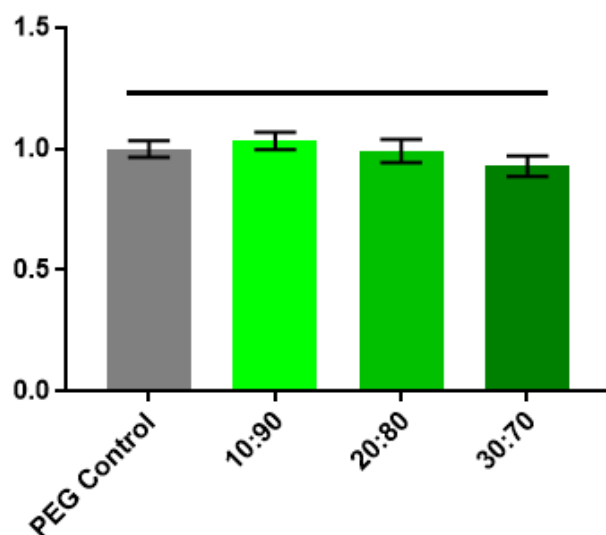
Figure A-7. Relative DNA content of hBMSCs after 14 days culture (during scaffold-induced osteogenesis studies) on templated SIPS PDMS$_{star}$-PEG scaffolds and analogous PEG-DA control. Scaffolds were fabricated with medium salt (~270 µm) and 2k PDMS$_{star}$-MA. No statistical differences among compositions were observed.
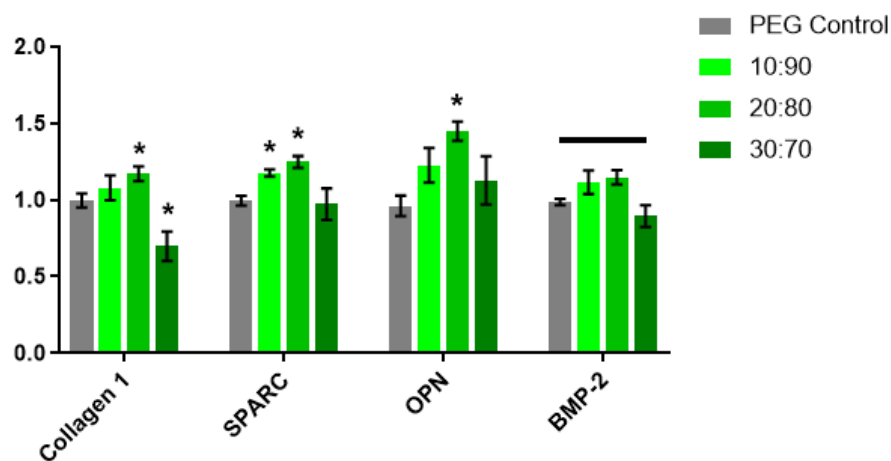
Figure A-8. Osteopontin (OPN) and BMP-2 immunoassay results after 14 day culture of hBMSCs, along with collagen 1 and SPARC levels previously shown in Fig. 7, on templated SIPS PDMS$_{star}$-PEG scaffolds and analogous PEG-DA control. Scaffolds were fabricated with medium salt (~270 µm) and 2k PDMS$_{star}$-MA. Statistically significant difference compared to the PEG-DA control is represented as $* = p < 0.05$. No statistical differences among compositions for BMP-2 expression were observed.

144
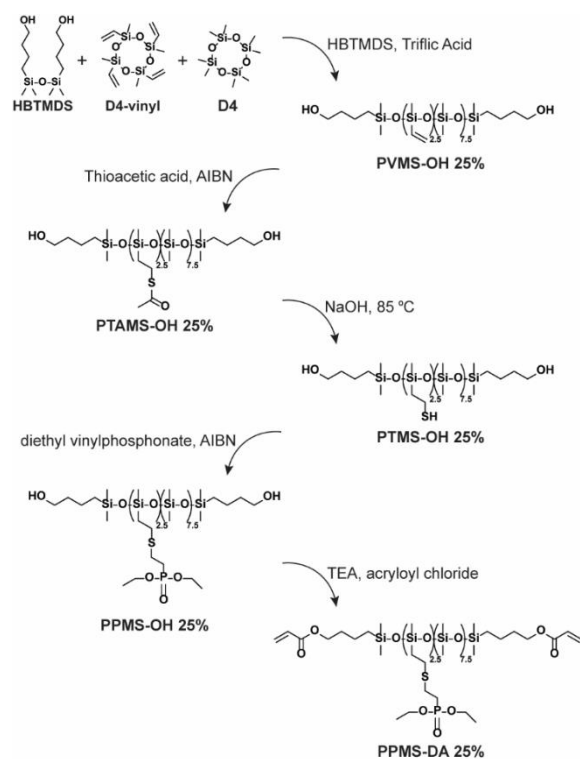
Figure A-9. Five-step synthetic scheme for synthesis of PPMS-DA 25% ($m = 7.5$ and $n = 2.5$).
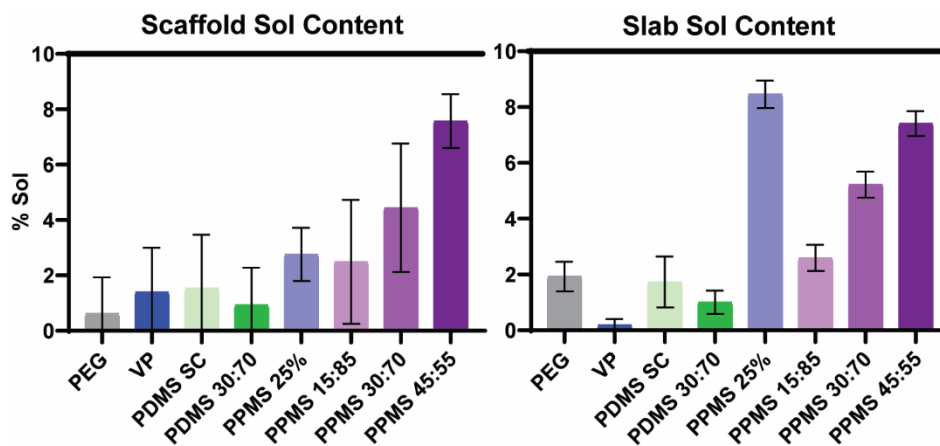
Figure A-10. Sol content % for (**A**) scaffolds and (**B**) non-porous slabs.
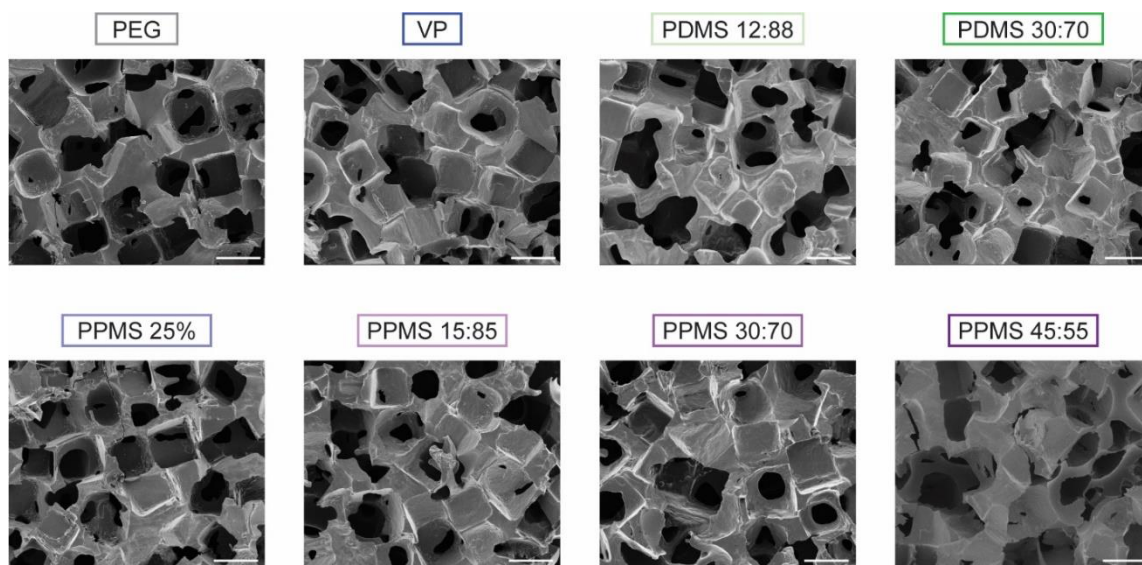
Figure A-11. SEM images of scaffolds. Scale bars = 100 µm.
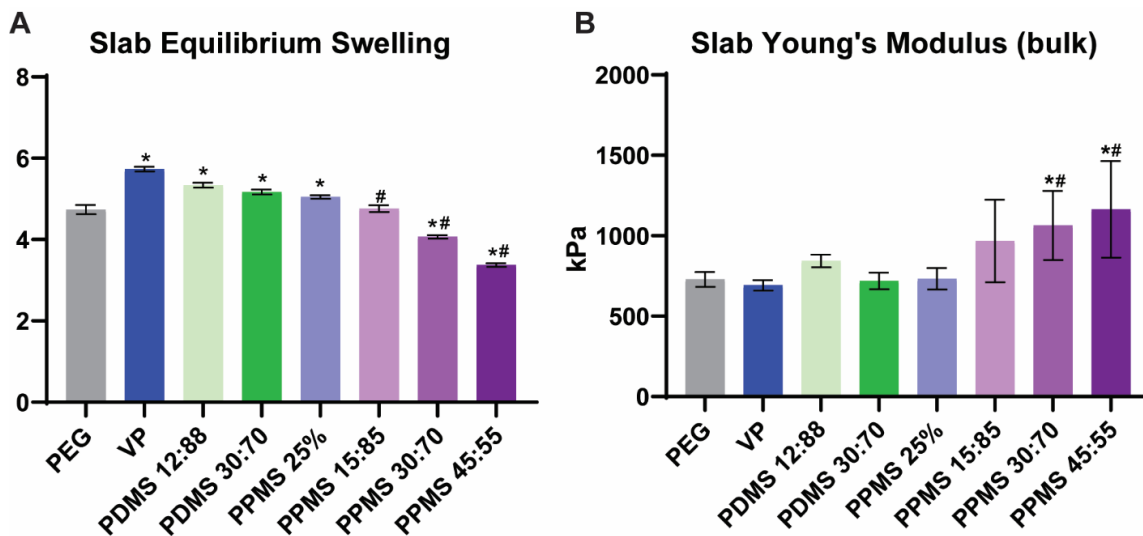
Figure A-12. **(A)** Non-porous slab equilibrium swelling, and **(B)** non-porous slab bulk Young's modulus. Statistical difference versus *PEG* is represented as * and versus *PDMS 30:70* is represented as # ($p < 0.05$).
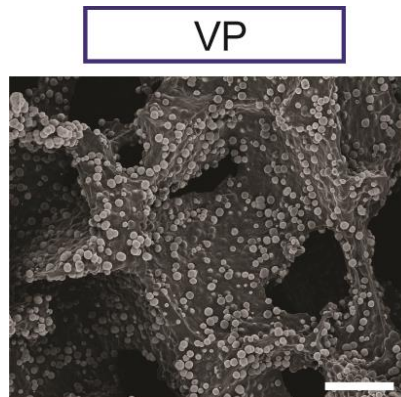
Figure A-13. SEM image of *VP* scaffold displaying HAp mineralization after soaking in simulated body fluid for 4 weeks (SBF, 1X, 37 °C). Scale bar = 100 µm.
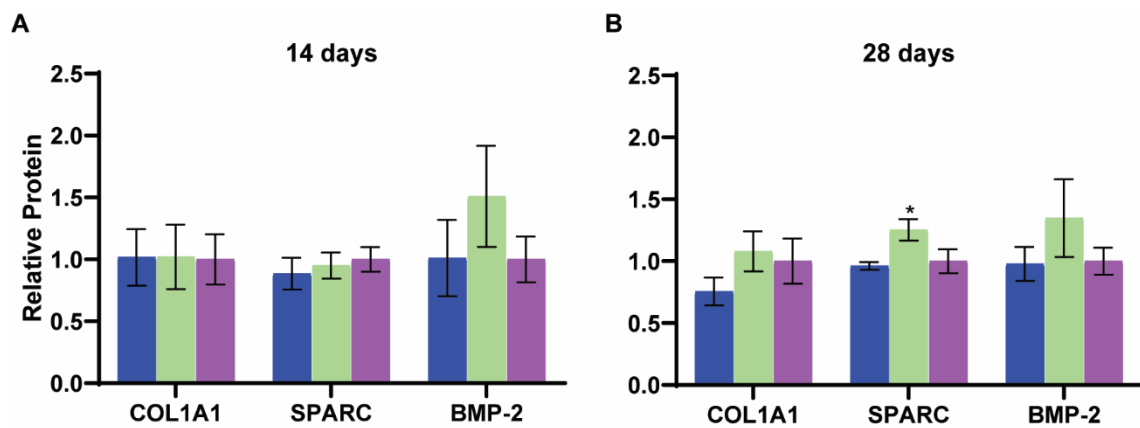
Figure A-14. Relative protein levels of *VP* (blue) and *PDMS 12:88* (green) versus *PPMS 30:70* (purple). Statistical differences versus PPMS 30:70 is indicated with * ($p <$ 0.05).
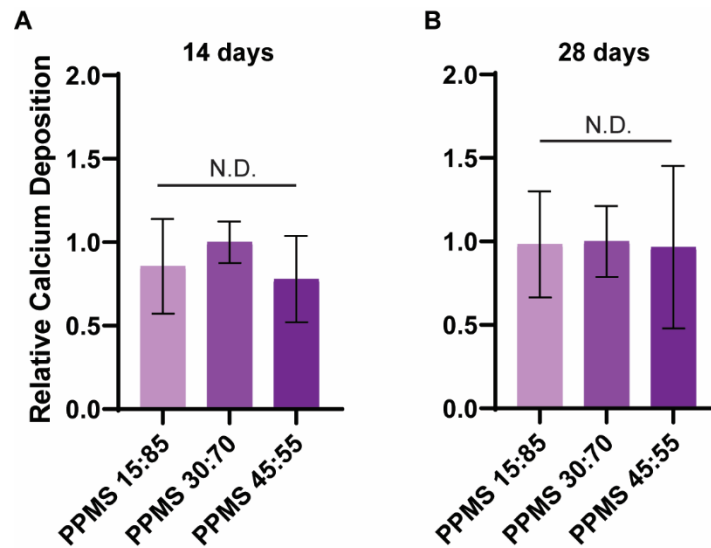
Figure A-15. Relative calcium deposition of *PPMS 15:85* (light purple), *PPMS 30:70* (medium purple), and *PPMS 45:55* (dark purple).
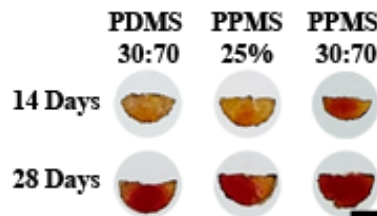
Figure A-16. Representative images of Alizarin Red S staining corresponding relative calcium deposition in Figure 3-7A. Due to the intensity of staining, only macro-images could be taken due to over-saturation during imaging. Scale bar = 4 mm.
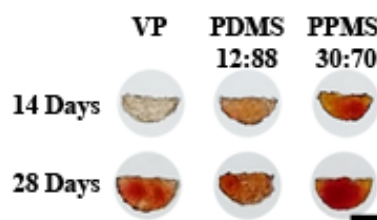
Figure A-17. Representative images of Alizarin Red S staining corresponding relative calcium deposition in Figure 3-7C. Due to the intensity of staining, only macro-images could be taken due to over-saturation during imaging. Scale bar = 4 mm.
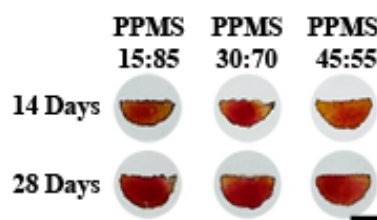
Figure A-18. Representative images of Alizarin Red S staining corresponding relative calcium deposition in Figure A-15. Due to the intensity of staining, only macro-images could be taken due to over-saturation during imaging. Scale bar = 4 mm.
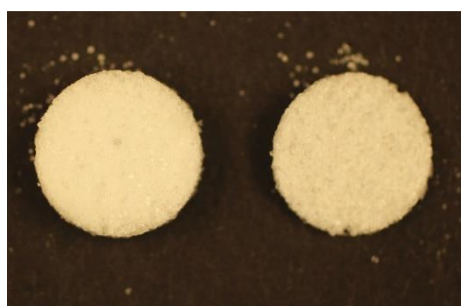
Figure A-19. Salt-containing scaffolds prior to being formed into SSTACs.
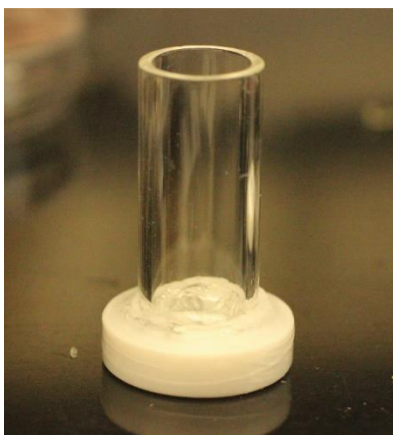
Figure A-20. SSTAC Fabrication mold.
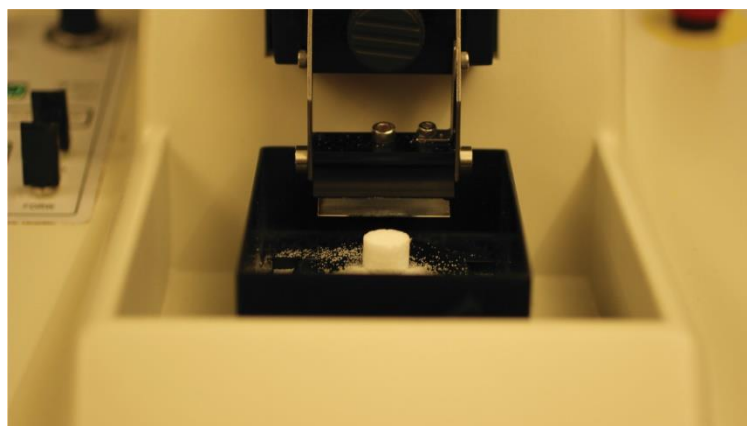
Figure A-21. Salt-containing scaffolds are cut with a vibratome (Leica VT1000S; pictured) to size prior to being formed into a hydrogel SSTAC.

Figure A-22. Custom confined shear set-up used for shear interface testing. Aluminum bar arms are set in tension clamps on an Instron 5944.
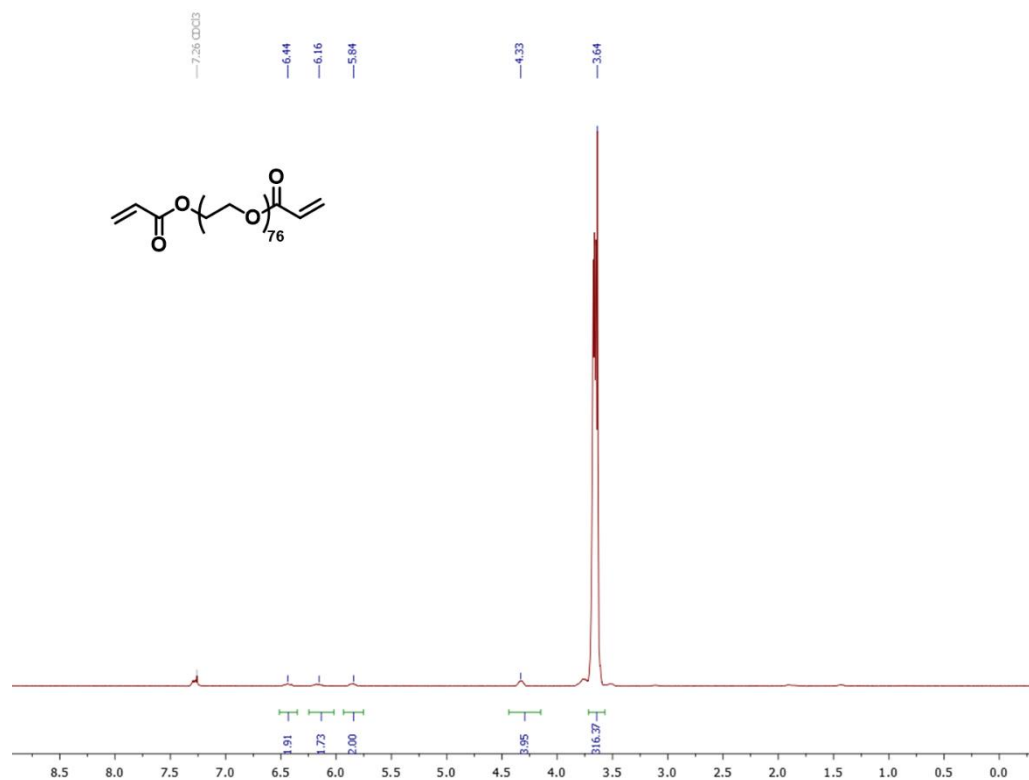
Figure B-1. NMR spectra for PEG-DA [n = 76; M_n = 3286 g/mol]. ¹H-NMR (500 MHz; δ, ppm): 3.64 (s, 316H, –OCH2CH2), 5.84 (m, 2H, –CH=CH_2), 6.16 (m, 2H, –CH=CH_2), 6.44 (m, 2H,–CH=CH$_2$).
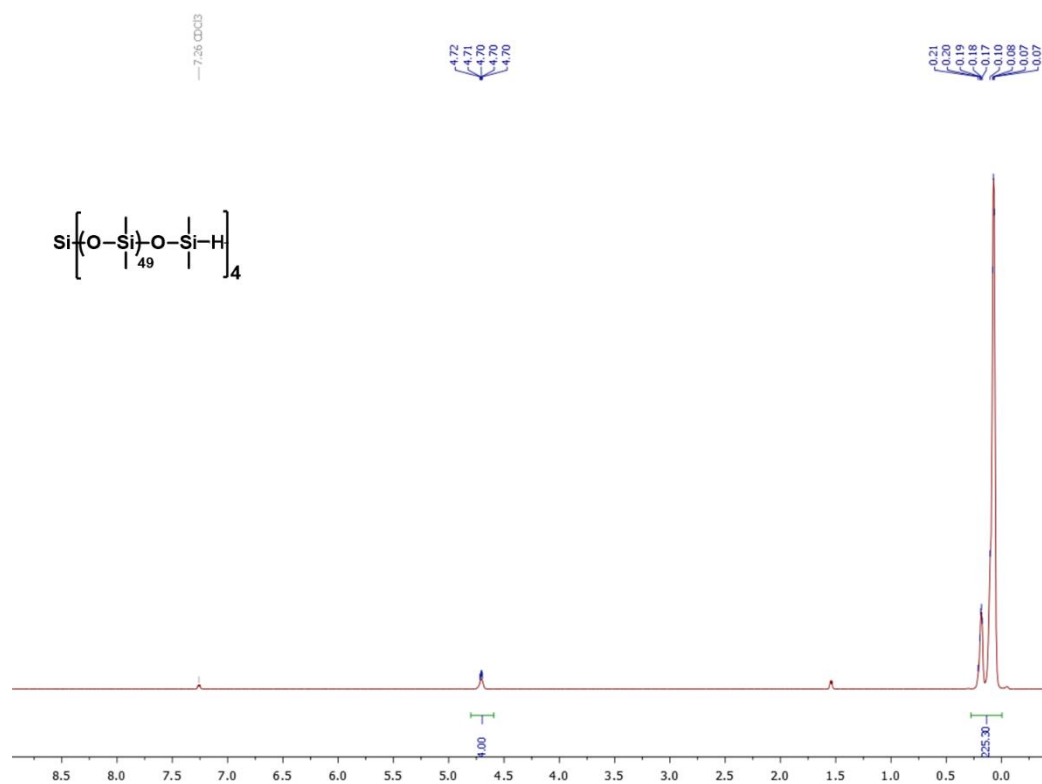
Figure B-2. NMR spectra for PDMS$_{star}$-SiH 2k [n = 4; M_n = 2807 g/mol]. ^{1}H-NMR (500 MHz; δ, ppm): 0-0.28 (bm, 225H, Si*CH$_3$*), 4.7 (m, 4H, Si*H*).
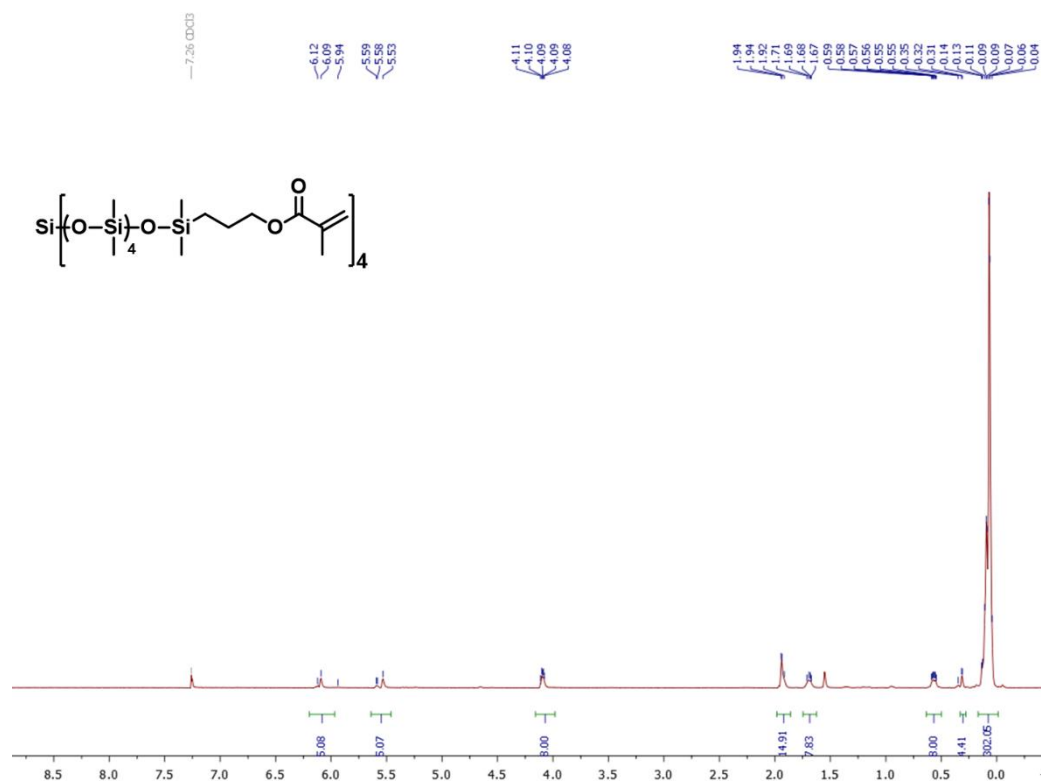
Figure B-3. NMR spectra for PDMS$_{star}$-MA 2k [$n = 4$; $M_n = 4233$ g/mol]. ^{1}H-NMR (500 MHz; δ, ppm): 0-0.22 (bm, 302H, Si*CH$_3$*), 0.56 (m, 8H, -Si*CH$_2$*CH$_2$CH$_2$), 1.68 (m, 8H, -SiCH$_2$*CH$_2$*CH$_2$), 1.94 (s, 12H, C(CH$_2$)*CH$_3$*), 4.09 (m, 8H, -SiCH$_2$CH$_2$*CH$_2$*), 5.53 (m, 4H, -*C(*CH$_2$*)*CH$_3$*)*, 6.09 (m, 4H, -C(*CH$_2$*)CH$_3$).
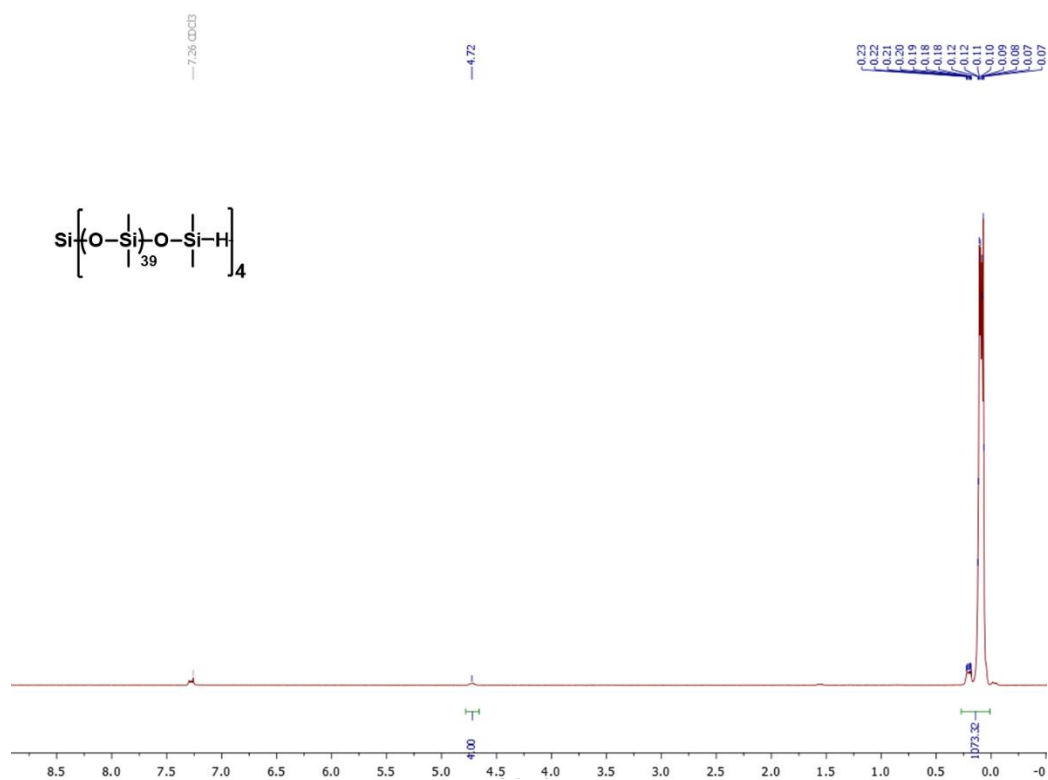
Figure B-4. NMR spectra for PDMS_{star}-SiH 7k [$n = 39$; $M_n = 13266$ g/mol]. ^{1}H-NMR (500 MHz; δ, ppm): 0.011-0.273 (bm, 1073H, Si*CH₃*), 4.72 (m, 4H, Si*H*).
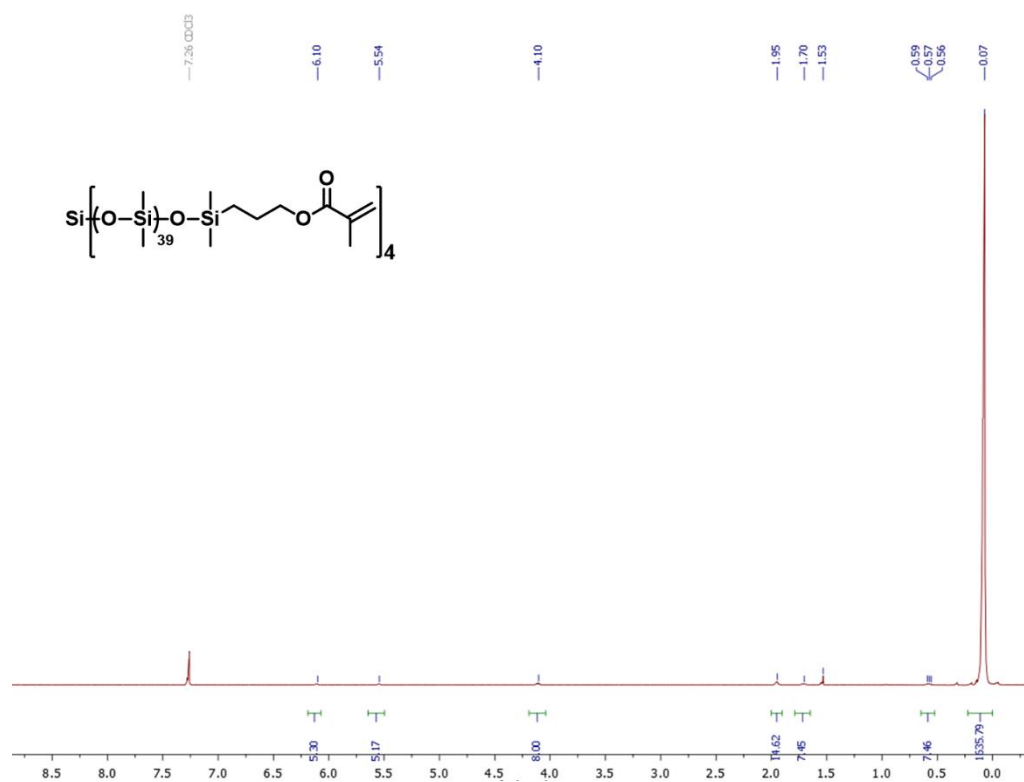
Figure B-5. NMR spectra for PDMS$_{star}$-MA 7k [$n = 39$; $M_n = 20673$ g/mol]. ^{1}H-NMR (500 MHz; δ, ppm): 0-0.22 (bm, 1635H, Si*CH$_3$*), 0.57 (m, 8H, -Si*CH$_2$*CH$_2$CH$_2$), 1.70 (m, 8H, -SiCH$_2$*CH$_2$*CH$_2$), 1.95 (s, 12H,-C(CH$_2$)*CH$_3$*), 4.10 (m, 8H, -SiCH$_2$CH$_2$*CH$_2$*), 5.54 (s, 4H, -C(*CH$_2$*)CH$_3$), 6.10 (s, 4H, -C(*CH$_2$*)CH$_3$).

156

Figure B-6. NMR spectra for PDMS-MA [$n = 10$; $M_n = 1044$ g/mol]. ^{1}H-NMR (400 MHz; δ, ppm): 0.07 (64.5H, Si*CH₃*), 0.56 (4H, Si*CH₂*CH₂CH₂CH₂O(O)*CH*CH₂), 0.96 (5H, CH₃Si*CH₂*CH₂S), 1.33 (15H, SCH₂CH₂P(O)CH₂*CH₃*), 1.40 (4H, SiCH₂*CH₂*CH₂CH₂O(O)*CH*CH₂), 1.58 (4H, SiCH₂CH₂*CH₂*CH₂O(O)*CH*CH₂), 2.03 (5H, SCH₂*CH₂*P(O)OCH₂CH₃), 2.61 (5H, CH₃SiCH₂*CH₂*S), 2.73 (5H, S*CH₂*CH₂P(O)CH₂CH₃), 3.65 (4H, SiCH₂CH₂CH₂*CH₂*O(O)*CH*CH₂), 4.1 (10H, SCH₂CH₂P(O)O*CH₂*CH₃), 6.12 (2H, SiCH₂CH₂CH₂CH₂O(O)*CH*CH₂), 6.36 (4H, SiCH₂CH₂CH₂CH₂O(O)CH*CH₂*).

Figure B-7. NMR spectra for PVMS-OH [*n* = 10]. ^{1}H-NMR (400 MHz; δ, ppm)**:** 0.08 (12H, Si*CH₃*), 0.14 (30H, *CH₃*SiCHCH₂), 0.56 (4H, Si*CH₂*CH₂CH₂CH₂OH), 1.40 (4H, SiCH₂*CH₂*CH₂CH₂OH), 1.57 (4H, SiCH₂CH₂*CH₂*CH₂OH), 3.64 (4H, SiCH₂CH₂CH₂*CH₂*OH), 5.79 (10H, CH₃Si*CH*CH₂), 5.96 (20H, CH₃SiCH*CH₂*).

158

Figure B-8. NMR spectra for PTAMS-OH [*n* = 10]. ^{1}H-NMR (400 MHz; δ, ppm)**:** 0.10 (12H, Si*CH₃*), 0.18 (30H, *CH₃*SiCHCH₂), 0.56 (4H, Si*CH₂*CH₂CH₂CH₂OH), 0.91 (20H, CH3Si*CH₂*CH₂), 1.42 (4H, SiCH₂*CH₂*CH₂CH₂OH), 1.59 (4H, SiCH₂CH₂*CH₂*CH₂OH), 2.3 (30H, SC(O)*CH₃*), 2.9 (20H, CH₃SiCH₂*CH₂*) 3.64 (4H, SiCH₂CH₂CH₂*CH₂*OH).
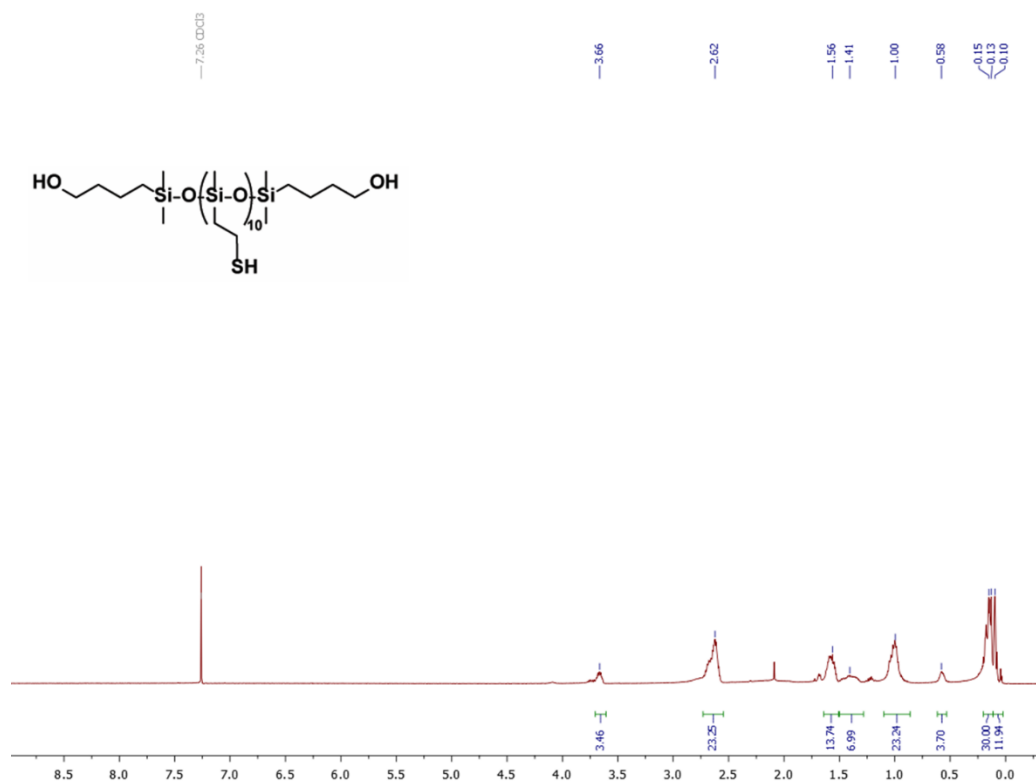
Figure B-9. NMR spectra for PTMS-OH [n = 10]. ^{1}H-NMR (400 MHz; δ, ppm)**:** 0.10 (12H, SiCH_3), 0.15 (30H, CH_3SiCHCH$_2$S), 0.58 (4H, SiCH_2CH$_2$CH$_2$CH$_2$OH), 1.00 (20H, CH$_3$SiCH_2CH$_2$S), 1.41 (4H, SiCH$_2$$CH_2CH_2CH_2$OH), 1.56 (4H, SiCH$_2CH_2$$CH_2CH_2$OH), 2.62 (20H, CH$_3$SiCH$_2$$CH_2$S), 3.66 (4H, SiCH$_2CH_2CH_2$$CH_2$OH).
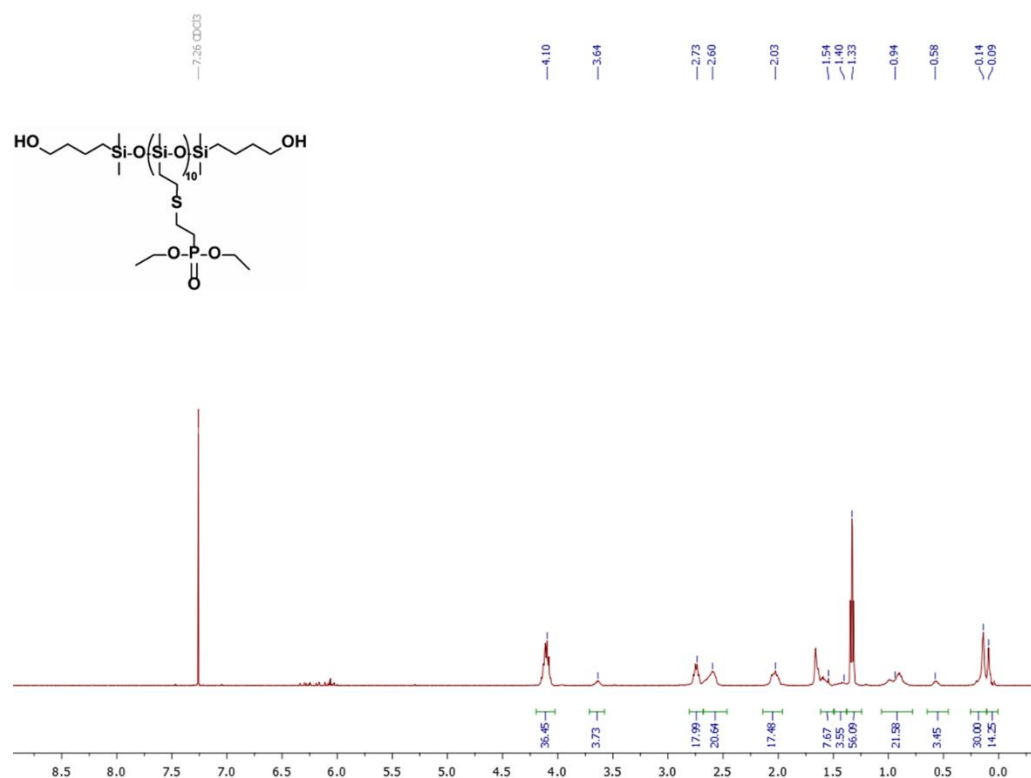
Figure B-10. NMR spectra for PPMS-OH [*n* = 10]. ¹H-NMR (400 MHz; δ, ppm)**:** 0.09 (12H, Si*CH₃*), 0.14 (30H, *CH₃*SiCHCH₂S), 0.58 (4H, Si*CH₂*CH₂CH₂CH₂OH), 0.94 (20H, CH₃Si*CH₂*CH₂S), 1.33 (60H, SCH₂CH₂P(O)CH₂*CH₃*), 1.40 (4H, SiCH₂*CH₂*CH₂CH₂OH), 1.54 (4H, SiCH₂CH₂*CH₂*CH₂OH), 2.03 (20H, SCH₂*CH₂*P(O)OCH₂CH₃), 2.60 (20H, CH₃SiCH₂*CH₂*S), 2.73 (20H, S*CH₂*CH₂P(O)CH₂CH₃), 3.64 (4H, SiCH₂CH₂CH₂*CH₂*OH), 4.1 (40H, SCH₂CH₂P(O)O*CH₂*CH₃).

Figure B-11. NMR spectra for PPMS-DA [*n* = 10]. ^{1}H-NMR (400 MHz; δ, ppm)**:** 0.09 (12H, Si*CH₃*), 0.14 (30H, *CH₃*SiCHCH₂S), 0.58 (4H, Si*CH₂*CH₂CH₂CH₂O(O)CHCH₂), 0.89 (20H, CH₃Si*CH₂*CH₂S), 1.33 (60H, SCH₂CH₂P(O)CH₂*CH3*), 1.40 (4H, SiCH₂*CH₂*CH₂CH₂O(O)CHCH₂), 1.54 (4H, SiCH₂CH₂*CH₂*CH₂O(O)CHCH₂), 2.02 (20H, SCH₂*CH₂*P(O)OCH₂CH₃), 2.58 (20H, CH₃SiCH₂*CH₂*S), 2.74 (20H, S*CH₂*CH₂P(O)CH₂CH₃), 2.94 (4H, SiCH₂CH₂CH₂*CH₂*O(O)CHCH₂), 4.1 (40H, SCH₂CH₂P(O)O*CH₂*CH₃), 6.11 (2H, SiCH₂CH₂CH₂CH₂O(O)*CH*CH₂), 6.33 (4H, SiCH₂CH₂CH₂CH₂O(O)CH*CH₂*).

162

Figure B-12. NMR spectra for PVMS-OH 25% [*n* = 2.5. *m* = 7.5]. ^{1}H-NMR (400 MHz; δ, ppm): 0.07 (57H, Si*CH₃*), 0.14 (7.5H, *CH₃*SiCHCH₂), 0.56 (4H, Si*CH₂*CH₂CH₂CH₂OH), 1.40 (4H, SiCH₂*CH₂*CH₂CH₂OH), 1.60 (4H, SiCH₂CH₂*CH₂*CH₂OH), 3.65 (4H, SiCH₂CH₂CH₂*CH₂*OH), 5.82 (2.5H, CH₃Si*CH*CH₂), 5.96 (5H, CH₃SiCH*CH₂*).
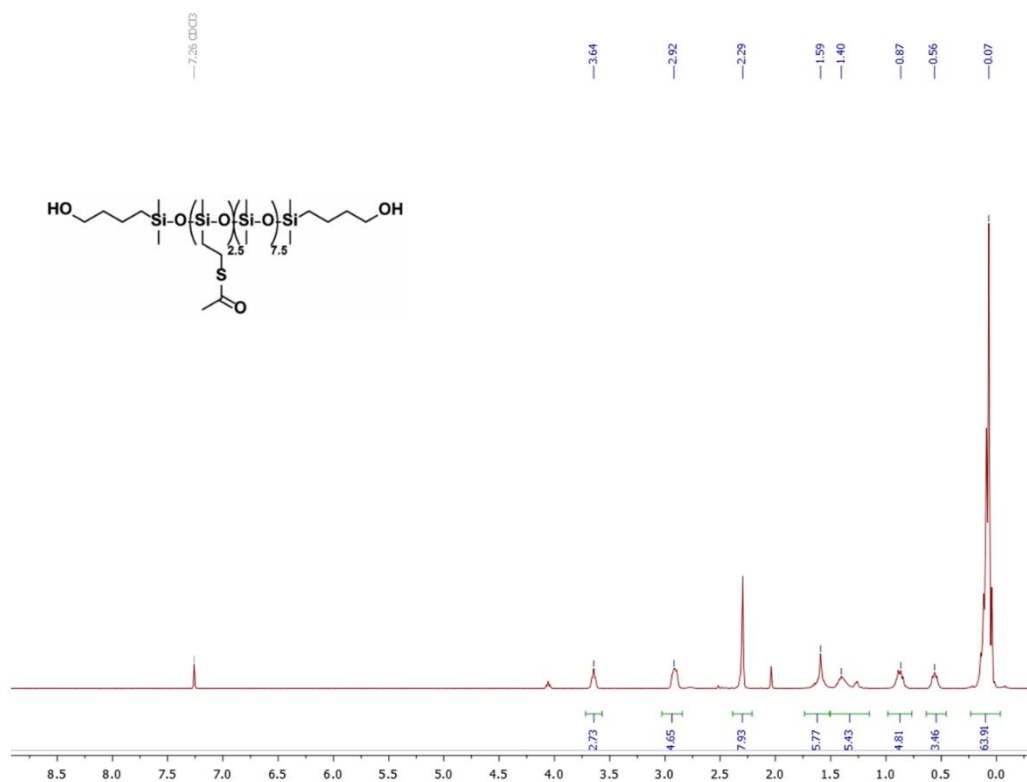
Figure B-13. NMR spectra for PTAMS-OH 25% [n = 2.5. m = 7.5]. ^{1}H-NMR (400 MHz; δ, ppm): 0.07 (64.5H, Si*CH₃*), 0.56 (4H, Si*CH₂*CH₂CH₂CH₂OH), 0.87 (5H, CH₃Si*CH₂*CH₂S), 1.40 (4H, SiCH₂*CH₂*CH₂CH₂OH), 1.59 (4H, SiCH₂CH₂*CH₂*CH₂OH), 2.29 (7.5H, SC(O)*CH₃*), 2.92 (5H, CH₃SiCH₂*CH₂*S), 3.64 (4H, SiCH₂CH₂CH₂*CH₂*OH).
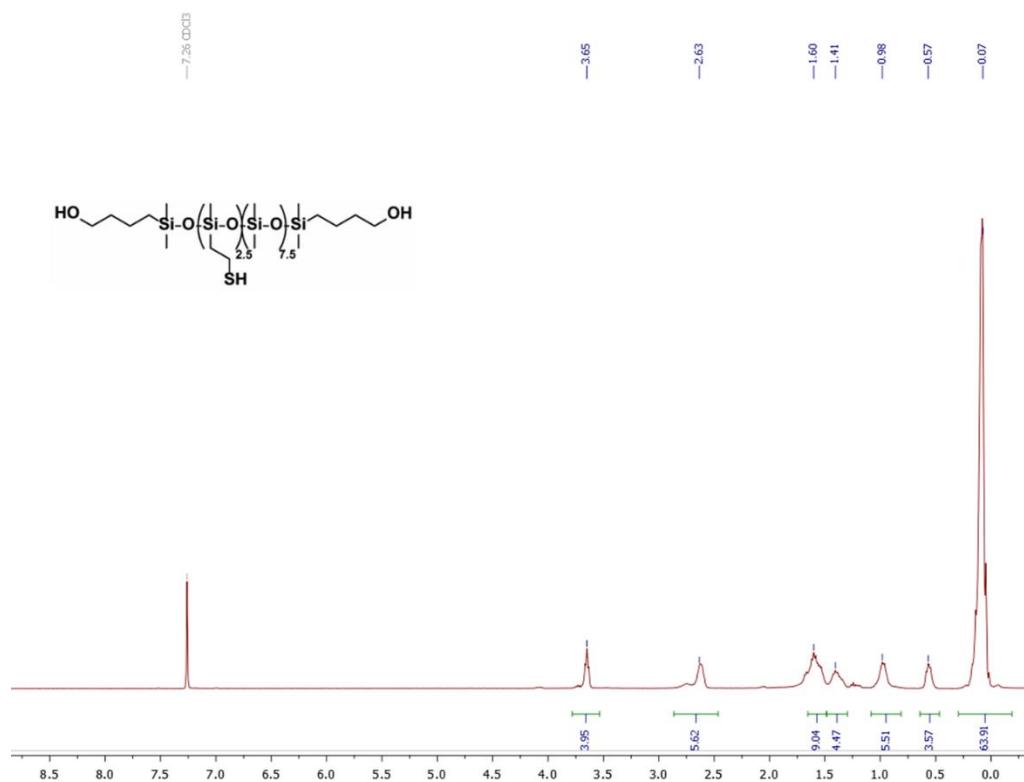
Figure B-14. NMR spectra for PTMS-OH 25% [*n* = 2.5. *m* = 7.5]. ^{1}H-NMR (400 MHz; δ, ppm): 0.07 (64.5H, Si*CH₃*), 0.57 (4H, Si*CH₂*CH₂CH₂CH₂OH), 0.98 (5H, CH₃Si*CH₂*CH₂S), 1.41 (4H, SiCH₂*CH₂*CH₂CH₂OH), 1.60 (4H, SiCH₂CH₂*CH₂*CH₂OH), 2.92 (5H, CH₃SiCH₂*CH₂*S), 3.64 (4H, SiCH₂CH₂CH₂*CH₂*OH).

Figure B-15. NMR spectra for PPMS-OH 25% [n = 2.5. m = 7.5]. ^{1}H-NMR (400 MHz; δ, ppm): 0.07 (64.5H, Si*CH$_3$*), 0.56 (4H, Si*CH$_2$*CH$_2$CH$_2$CH$_2$OH), 0.96 (5H, CH$_3$Si*CH$_2$*CH$_2$S), 1.33 (15H, SCH$_2$CH$_2$P(O)CH$_2$*CH$_3$*), 1.40 (4H, SiCH$_2$*CH$_2$*CH$_2$CH$_2$OH), 1.58 (4H, SiCH$_2$CH$_2$*CH$_2$*CH$_2$OH), 2.03 (5H, SCH$_2$*CH$_2$*P(O)OCH$_2$CH$_3$), 2.61 (5H, CH$_3$SiCH$_2$*CH$_2$*S), 2.73 (5H, S*CH$_2$*CH$_2$P(O)CH$_2$CH$_3$), 3.65 (4H, SiCH$_2$CH$_2$CH$_2$*CH$_2$*OH), 4.1 (10H, SCH$_2$CH$_2$P(O)O*CH$_2$*CH$_3$).

166
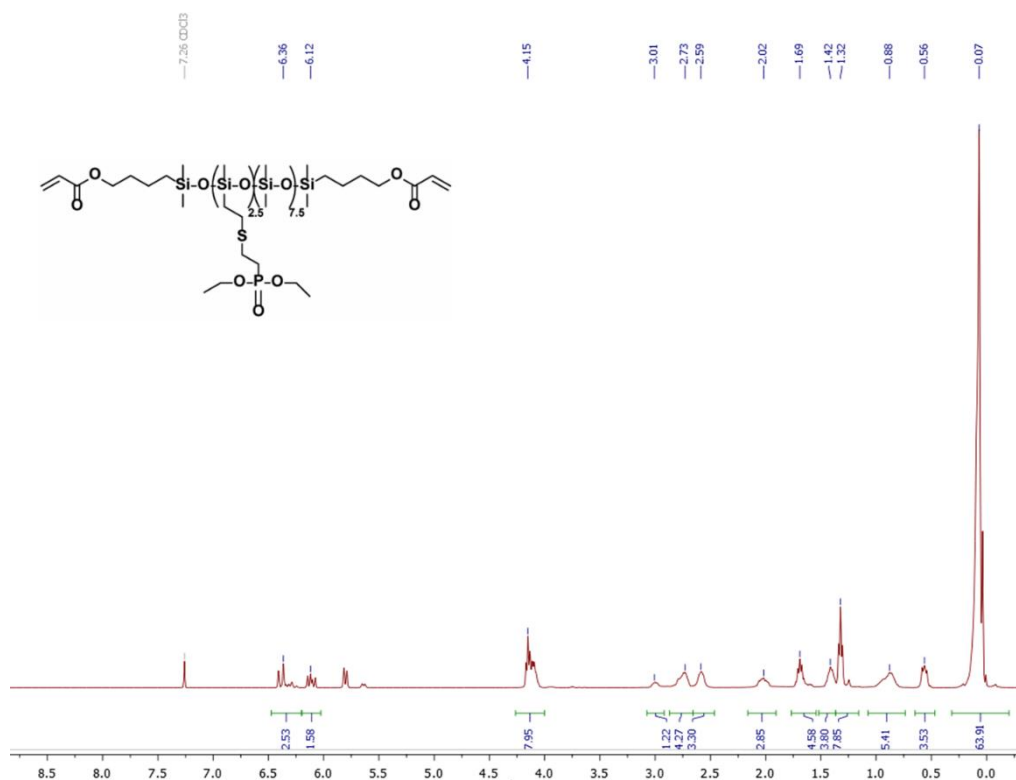
Figure B-16. NMR spectra for PPMS-DA 25% [*n* = 2.5. *m* = 7.5]. ^{1}H-NMR (400 MHz; δ, ppm): 0.07 (64.5H, Si*CH$_3$*), 0.56 (4H, Si*CH$_2$*CH$_2$CH$_2$CH$_2$O(O)*CH*CH$_2$), 0.96 (5H, CH$_3$Si*CH$_2$*CH$_2$S), 1.33 (15H, SCH$_2$CH$_2$P(O)CH$_2$*CH$_3$*), 1.40 (4H, SiCH$_2$*CH$_2$*CH$_2$CH$_2$O(O)*CH*CH$_2$), 1.58 (4H, SiCH$_2$CH$_2$*CH$_2$*CH$_2$O(O)*CH*CH$_2$), 2.03 (5H, SCH$_2$*CH$_2$*P(O)OCH$_2$CH$_3$), 2.61 (5H, CH$_3$SiCH$_2$*CH$_2$*S), 2.73 (5H, S*CH$_2$*CH$_2$P(O)CH$_2$CH$_3$), 3.65 (4H, SiCH$_2$CH$_2$CH$_2$*CH$_2$*O(O)*CH*CH$_2$), 4.1 (10H, SCH$_2$CH$_2$P(O)O*CH$_2$*CH$_3$), 6.12 (2H, SiCH$_2$CH$_2$CH$_2$CH$_2$O(O)*CH*CH$_2$), 6.36 (4H, SiCH$_2$CH$_2$CH$_2$CH$_2$O(O)CH*CH$_2$*).

APPENDIX C

DATA TABLES FOR BAR GRAPHS

Table C-1. Percent interconnectivity values (mean ± SD) for samples from **Figure 2-3A.**

	Aqueous	SIPS	Templated
% interconnectivity:	8.84 ± 2.46 µm	11.43 ± 3.57 µm	54.71 ± 5.41 µm

Table C-2. Equilibrium swelling values (mean ± SD) for samples from **Figure 2-3B.**

	PEG	2k 10:90	2k 20:80	2k 30:70	7k 10:90	7k 20:80	7k 30:70
Equil. Swelling	8.63 ± 0.51	7.99 ± 0.28	6.92 ± 0.86	7.57 ± 0.51	7.84 ± 0.67	7.65 ± 0.70	7.89 ± 0.95

Table C-3. Percent interconnectivity values (mean ± SD) for samples from **Figure 2-3C.**

	PEG	2k 10:90	2k 20:80	2k 30:70	7k 10:90	7k 20:80	7k 30:70
Damping	0.051 ± 0.0083 Tan δ	0.032 ± 0.0068 Tan δ	0.031 ± 0.0066 Tan δ	0.030 ± 0.0075 Tan δ	0.052 ± 0.0076 Tan δ	0.047 ± 0.0081 Tan δ	0.052 ± 0.0102 Tan δ

Table C-4. Local Young's modulus values (mean ± SD) for samples from **Figure 2-3D.**

	PEG	2k 10:90	2k 20:80	2k 30:70
Local Young's Modulus	61.07 ± 13.63 kPa	28.14 ± 5.95 kPa	17.26 ± 11.85 kPa	13.98 ± 11.10 kPa

Table C-5. Relative cytotoxicity values (mean ± SD) for samples from **Figure 2-5.**

	PEG	2k 10:90	2k 20:80	2k 30:70
2k Cytotoxicity	1.00 ± 0.117	0.925 ± 0.064	0.825 ± 0.048	0.845 ± 0.170

	PEG	7k 10:90	7k 20:80	7k 30:70
7k Cytotoxicity	1.00 ± 0.127	0.984 ± 0.174	0.941 ± 0.122	0.970 ± 0.147

Table C-6. Relative Collagen 1 values (mean ± SD) for samples from **Figure 2-6A.**

	PEG	2k 10:90	2k 20:80	2k 30:70	7k 10:90	7k 20:80	7k 30:70
Col 1	1.00 ± 0.123	0.032 ± 0.0068	0.031 ± 0.0066	0.030 ± 0.0075	0.052 ± 0.0076	0.047 ± 0.0081	0.052 ± 0.0102

Table C-7. Relative SPARC values (mean ± SD) for samples from **Figure 2-6B.**

	PEG	2k 10:90	2k 20:80	2k 30:70	7k 10:90	7k 20:80	7k 30:70
SPARC	1.00 ± 0.084	1.181 ± 0.0366	1.254 ± 0.0622	0.976 ± 0.1828	1.036 ± 0.0884	1.097 ± 0.1101	1.220 ± 0.1127

Table C-8. Scaffold pore size values (mean ± SD) for samples from **Figure 3-4A.**

PORE SIZES	PEG	VP	PDMS 12:88	PDMS 30:70	PPMS 25%	PPMS 15:85	PPMS 30:70	PPMS 45:55
Dry	205.9 ± 23.6 µm	178.7 ± 16.4 µm	193.8 ± 17.9 µm	174.2 ± 17.0 µm	174.6 ± 30.6 µm	180.1 ± 18.5 µm	201.4 ± 22.0 µm	171.9 ± 19.4 µm
Hydrated	366.2 ± 45.2 µm	378.0 ± 43.0 µm	388.5 ± 33.8 µm	384.0 ± 38.2 µm	369.5 ± 42.2 µm	375.9 ± 43.2 µm	359.6 ± 29.2 µm	355.3 ± 51.7 µm

Table C-9. Scaffold hydrophobicity index values (mean ± SD) for samples from **Figure 3-4B.**

	PEG	VP	PDMS 12:88	PDMS 30:70	PPMS 25%	PPMS 15:85	PPMS 30:70	PPMS 45:55
H-index	0.75 ± 0.38	0.87 ± 0.04	0.90 ± 0.05	1.29 ± 0.18	1.44 ± 0.067	1.25 ± 0.12	1.79 ± 0.40	1.45 ± 0.29

Table C-10. Scaffold equilibrium swelling values (mean ± SD) for samples from **Figure 3-4C.**

	PEG	VP	PDMS 12:88	PDMS 30:70	PPMS 25%	PPMS 15:85	PPMS 30:70	PPMS 45:55
Equil. Swelling	15.7 ± 1.60	15.4 ± 0.60	13.4 ± 0.87	12.9 ± 1.15	9.9 ± 0.72	12.2 ± 1.03	7.5 ± 1.99	5.4 ± 0.90

Table C-11. Scaffold bulk Young's modulus values (mean ± SD) for samples from **Figure 3-4D.**

	PEG	VP	PDMS 12:88	PDMS 30:70	PPMS 25%	PPMS 15:85	PPMS 30:70	PPMS 45:55
Scaffold Bulk Young's	34.1 ± 2.2 kPa	37.3 ± 1.1 kPa	44.8 ± 4.2 kPa	27.5 ± 10.6 kPa	46.5 ± 4.9 kPa	40.7 ± 1.3 kPa	38.3 ± 5.2 kPa	32.5 ± 1.7 kPa

Table C-12. Relative scaffold local Young's modulus values (mean ± SD) for samples from **Figure 3-4E.**

	PEG	VP	PDMS 12:88	PDMS 30:70	PPMS 25%	PPMS 15:85	PPMS 30:70	PPMS 45:55
Scaffold Local Young's	35.1 ± 13.3 kPa	16.6 ± 4.5 kPa	15.1 ± 2.2 kPa	10.0 ± 5.4 kPa	25.4 ± 12.7 kPa	48.2 ± 14.4 kPa	23.3 ± 4.4 kPa	21.7 ± 14.2 kPa

Table C-13. Relative cytotoxicity values (mean ± SEM) for samples from **Figure 3-6A.**

	PEG	VP	PDMS 12:88	PDMS 30:70	PPMS 25%	PPMS 15:85	PPMS 30:70	PPMS 45:55
Cytotox.	1.00 ± 0.10	1.02 ± 0.29	1.04 ± 0.05	0.65 ± 0.18	1.05 ± 0.11	0.98 ± 0.32	1.04 ± 0.18	0.95 ± 0.21

Table C-14. *In vitro* hBMSC culture relative values (mean ± SEM) for samples from **Figure 3-7A&B.**

	PDMS 30:70	PPMS 25%	PPMS 30:70
Alizarin Red S (14-day)	1.00 ± 0.261	1.10 ± 0.088	2.56 ± 0.160
Alizarin Red S (28-day)	1.00 ± 0.081	1.32 ± 0.204	2.23 ± 0.236
Col 1 (14-day)	1.00 ± 0.266	0.54 ± 0.122	0.67 ± 0.14
Col 1 (28-day)	1.00 ± 0.171	0.75 ± 0.121	0.68 ± 0.123
SPARC (14-day)	1.00 ± 0.181	0.61 ± 0.082	0.92 ± 0.091
SPARC (28-day)	1.00 ± 0.67	0.72 ± 0.043	0.84 ± 0.081
BMP-2 (14-day)	1.00 ± 0.338	1.06 ± 0.378	0.91 ± 0.167
BMP-2 (28-day)	1.00 ± 0.18	1.21 ± 0.170	0.84 ± 0.092

Table C-15. Relative calcium deposition values (mean ± SEM) for samples from **Figure 3-7C.**

	VP	PDMS 12:88	PPMS 30:70
Alizarin Red S (14-day)	0.21 ± 0.035	0.38 ± 0.158	1.00 ± 0.062
Alizarin Red S (28-day)	0.47 ± 0.123	0.52 ± 0.151	1.00 ± 0.106

Table C-16. Relative protein expression values (mean ± SEM) for samples from **Figure 3-7D.**

	PPMS 15:85	PPMS 30:70	PPMS 45:55
Col 1 (14-day)	1.21 ± 0.397	1.00 ± 0.203	1.11 ± 0.262
Col 1 (28-day)	1.048 ± 0.114	1.00 ± 0.096	1.19 ± 0.164
SPARC (14-day)	0.949 ± 0.140	1.00 ± 0.099	0.94 ± 0.0.14
SPARC (28-day)	0.99 ± 0.083	1.00 ± 0.096	1.05 ± 0.083
BMP-2 (14-day)	1.27 ± 0.386	1.00 ± 0.184	0.41 ± 0.051
BMP-2 (28-day)	1.67 ± 0.213	1.00 ± 0.109	1.16 ± 0.179

Table C-17. SSTAC compressive modulus values (mean ± SD) for samples from **Figure 4-2D.**

	PEG	PEG SSTAC	PPMS	PPMS SSTAC
Young's Modulus	34 ± 2.2 kPa	128 ± 23.1 kPa	38 ± 5.2 kPa	58 ± 18.1 kPa

Table C-18. SSTAC shear interface analysis (mean ± SD) for samples from **Figure 4-2E.**

	PEG	PEG:PEG SSTAC
Shear Force at Break	2.37 ± 0.75 N	1.94 ± 0.92 N
Displacement	6.01 ± 0.53 mm	1.97 ± 0.89 mm

Table C-19. Bulk Young's modulus values (mean ± SD) for samples from **Figure A-4.**

	PEG	2k 10:90	2k 20:80	2k 30:70
Bulk Young's Modulus	8.68 ± 0.781 kPa	7.74 ± 0.974 kPa	7.31 ± 1.259 kPa	7.71 ± 1.563 kPa

Table C-20. Mass loss % values (mean ± SD) for samples from **Figure A-5.**

ACCEL. DEG.	PEG	2k 10:90	2k 20:80	2k 30:70
12 h.	10.1 ± 2.0 %	14.0 ± 1.7 %	10.9 ± 4.9 %	14.6 ± 5.6 %
24 h.	25.7 ± 5.1 %	20.8 ± 3.4 %	27.5 ± 1.3 %	25.4 ± 4.4 %
36 h.	37.5 ± 4.3 %	31.6 ± 5.4 %	33.7 ± 0.8 %	34.0 ± 2.2 %
48 h.	42.6 ± 3.9 %	47.5 ± 2.6 %	43.8 ± 7.7 %	45.6 ± 5.2 %
60 h.	53.3 ± 11.6 %	49.9 ± 8.7 %	54.9 ± 9.8 %	56.4 ± 8.5 %

Table C-21. Relative DNA content values (mean ± SD) for samples from **Figure A-7.**

	PEG	2k 10:90	2k 20:80	2k 30:70
DNA Content	1.00 ± 0.035	1.03 ± 0.036	0.99 ± 0.048	0.93 ± 0.043

Table C-22. Relative protein expression values (mean ± SD) for samples from **Figure A-8.**

ACCEL. DEG.	PEG	2k 10:90	2k 20:80	2k 30:70
Col 1	1.00 ± 0.046	1.08 ± 0.081	1.17 ± 0.048	0.70 ± 0.096
SPARC	1.00 ± 0.031	1.18 ± 0.022	1.25 ± 0.038	0.97 ± 0.102
OPN	0.96 ± 0.067	1.23 ± 0.113	1.45 ± 0.063	1.13 ± 0.157
BMP-2	0.99 ± 0.021	1.12 ± 0.078	1.15 ± 0.046	0.90 ± 0.070

Table C-23. Sol content values (mean ± SD) for samples from **Figure A-10.**

% SOL	PEG	VP	PDMS 12:88	PDMS 30:70	PPMS 25%	PPMS 15:85	PPMS 30:70	PPMS 45:55
Scaffold	0.62 ± 1.31	1.40 ± 1.60	1.53 ± 1.94	0.93 ± 1.35	2.76 ± 0.96	2.49 ± 2.24	4.44 ± 2.32	7.57 ± 0.97
Slab	1.93 ± 0.53	0.19 ± 0.22	1.73 ± 0.91	1.01 ± 0.42	8.46 ± 0.50	2.60 ± 0.47	5.22 ± 0.46	7.41 ± 0.45

Table C-24. Slab equilibrium swelling values (mean ± SD) for samples from **Figure A-12A.**

	PEG	VP	PDMS 12:88	PDMS 30:70	PPMS 25%	PPMS 15:85	PPMS 30:70	PPMS 45:55
Slab Equil. Swelling	4.74 ± 0.11	5.73 ± 0.06	5.34 ± 0.06	5.17 ± 0.06	5.05 ± 0.04	4.76 ± 0.08	4.07 ± 0.04	3.38 ± 0.04

Table C-25. Slab bulk Young's modulus values (mean ± SD) for samples from **Figure A-12B.**

	PEG	VP	PDMS 12:88	PDMS 30:70	PPMS 25%	PPMS 15:85	PPMS 30:70	PPMS 45:55
Slab Bulk Young's	728.8 ± 45.5 kPa	695.3 ± 24.4 kPa	846.8 ± 42.1 kPa	718.0 ± 37.4 kPa	732.6 ± 66.2 kPa	967.3 ± 257 kPa	1064 ± 215 kPa	1164 ± 300 kPa

Table C-26. Relative protein expression values (mean ± SEM) for samples from **Figure A-14.**

	VP	PDMS 12:88	PPMS 30:70
Col 1 (14-day)	1.02 ± 0.229	1.02 ± 0.260	1.00 ± 0.204
Col 1 (28-day)	0.76 ± 0.112	1.08 ± 0.161	1.00 ± 0.182
SPARC (14-day)	0.89 ± 0.128	0.95 ± 0.105	1.00 ± 0.100
SPARC (28-day)	0.96 ± 0.032	1.25 ± 0.089	1.00 ± 0.096
BMP-2 (14-day)	1.01 ± 0.309	1.51 ± 0.408	1.00 ± 0.408
BMP-2 (28-day)	0.98 ± 0.137	1.35 ± 0.3140	1.00 ± 0.109

Table C-27. Relative calcium deposition values (mean ± SEM) for samples from **Figure A-15.**

	PPMS 15:85	PPMS 30:70	PPMS 45:55
Alizarin Red S (14-day)	0.86 ± 0.142	1.00 ± 0.0625	0.78 ± 0.128
Alizarin Red S (28-day)	0.98 ± 0.159	1.00 ± 0.106	0.97 ± 0.244